INFORMATION TO USERS

EXPERIMENTAL INVESTIGATION OF THE BIAXIAL FLEXURAL STRENGTH

OF 8YSZ THIN CERAMIC SUBSTRATES AS ELECTROLYTES

By

Ming Cheng

A Dissertation Submitted to the Faculty of the

DEPARTMENT OF AEROSPACE AND MECHANICAL ENGINEERING

In partial Fulfillment of the Requirements
For the Degree of

DOCTOR OF PHILOSOPHY
WITH A MAJOR IN MECHANICAL ENGINEERING

In the Graduate College

THE UNIVERSITY OF ARIZONA

2 0 0 2

UMI Number: 3050320

UMI®

THE UNIVERSITY OF ARIZONA ®
GRADUATE COLLEGE

As members of the Final Examination Committee, we certify that we have

read the dissertation prepared by_____Ming Cheng_____

entitled _____EXPERIMENTAL INVESTIGATION OF THE BIAXIAL FLEXURAL_____

_____STRENGTH OF 8YSZ THIN CERAMIC SUBSTRATES AS ELECTROLYTES_____

_____

_____

_____

and recommend that it be accepted as fulfilling the dissertation

requirement for the Degree of _____Doctor of Philosophy_____

Weinong (Wayne) Chen	3/27/02 — Date
Sergey V. Shkarayev	3/27/02 — Date
Tribikram Kundu	3/27/02 — Date
Michael W. Marcellin	3/27/02 — Date
Jeffrey J. Rodriguez	3-27-02 — Date

Final approval and acceptance of this dissertation is contingent upon
the candidate's submission of the final copy of the dissertation to the
Graduate College.

I hereby certify that I have read this dissertation prepared under my
direction and recommend that it be accepted as fulfilling the dissertation
requirement.

_____   3/27/02
Dissertation Director   Date
 Weinong (Wayne) Chen

STATEMENT BY AUTHOR

This dissertation has been submitted in partial fulfillment of requirements for an advanced degree at The University of Arizona and is deposited in the University Library to be made available to borrowers under rules of the Library.

Brief quotations from this dissertation are allowable without special permission, provided that accurate acknowledgment of source is made. Requests for permission for extended quotation from or reproduction of this manuscript in whole or in part may be granted by the head of the major department or the Dean of the Graduate College when in his or her judgment the proposed use of the material is in the interests of scholarship. In all other instances, however, permission must be obtained from the author.

SIGNED: _Ming Cheng_

ACKNOWLEDGEMENTS

The author wishes to express his extreme appreciation to Professor W. Chen. His guidance, friendship, and unending quest to understand that to which we have dedicated our lives have had profound impact on my skills, my drive, and my engineering philosophy. Having worked with Dr. Chen through my doctorate, I have come to appreciate the degree to which we complement each other in our working environment. I thank him for giving me the opportunity and the pleasure of working with him during this research and I look forward to a lasting friendship.

The author would also like to thank Dr. M. Gottmann, Dr. D. Nyuen, and Mr. B. Zhang for the helpful discussions, Ms. S. Brach for her assistance on the specimen preparation.

Finally, the author would like to extend his gratitude to his family, friends, and, most of all, his wife Qizhi, for their encouragement, patience, and understanding during this work.

DEDICATION

TO MY WIFE AND MY WHOLE FAMILY

TABLE OF CONTENTS

TABLE OF CONTENTS - *Continued*

TABLE OF CONTENTS - *Continued*

LIST OF ILLUSTRATIONS

LIST OF ILLUSTRATIONS - *Continued*

LIST OF ILLUSTRATIONS - *Continued*

LIST OF ILLUSTRATIONS - *Continued*

LIST OF ILLUSTRATIONS - *Continued*

LIST OF TABLES

ABSTRACT

Thin ceramic substrates are widely used in engineering applications in modern industry. For example, they are used as molecular filters in fuel cells and solid oxide electrolyzers for oxygen generation. Development of high-reliability substrate materials inevitably requires the accurate characterization of their mechanical properties. The loading conditions in service on the ceramic substrates, such as the solid oxide electrolytes with a thickness of much less than 2 mm, often involve multiaxial bending instead of simple tension or bending.

In this dissertation, the ASTM standard piston-on-3-ball experimental technique at ambient temperature is employed to investigate the quasi-static biaxial flexural strength of pure 8YSZ and Al_2O_3 or 3YSZ doped 8YSZ ceramic substrates. Furthermore, this piston-on-3-ball experimental technique is developed into a dynamic piston-on-3-ball technique at ambient temperature and a quasi-static piston-on-3-ball technique at elevated temperatures. Stress distribution functions in the tensile surface of a specimen under piston-on-3-ball loading condition are formulated and used to develop statistical models, which are proven to be in the form of a Weibull distribution function, to describe the biaxial flexural strength behavior of ceramic substrates under piston-on-3-ball loading condition. Analytical modeling was conducted on the dynamic piston-on-3-ball loading configuration. This analytical model can be used to guide the experimental design and judge the validity of experimental results. A new material constitutive model is

developed to give a good description of the dynamic strength behavior of ceramic materials under constant stress-rate loading.

Quasi-static experiments under piston-on-3-ball loading are conducted at both ambient temperature and elevated temperatures, while dynamic experiments are conducted at ambient temperature. Experimental results, as well as observations from SEM microstructure images and values of fracture toughness measured using a newly developed Vickers micro-indentation toughness technique, lead to a conclusion that no obvious overall improvement to the 8YSZ ceramic substrates in the biaxial flexural strength can be observed by adding Al_2O_3 additive with amount up to 3 mol% or 3YSZ additive with amount up to 30 wt%.

CHAPTER 1

INTRODUCTION

This research is a part of a NASA-sponsored research program, "The development of superior materials for layered solid oxide electrolyzers based on mechanical and thermal failure testing and analysis," which studies the material issues related to solid oxide electrolyzers (electrochemical systems) that will generate oxygen from the atmosphere of Mars and also from the lunar regolith.

1.1 Applications of 8YSZ thin ceramic substrates

The high oxygen ion conductivity over wide ranges of temperature and oxygen pressures in 8-mol% yttria stabilized zirconia (8YSZ) has led to its use as a solid oxide electrolyte in a variety of electrochemical applications (Pasciak, Prociow, Mielcarek, Gornicka, and Mazurek, 2001). These include high temperature solid oxide fuel cells (SOFCs) which offer a clean, pollution-free technology to electrochemically generate electricity at high efficiencies. These fuel cells provide many advantages over traditional energy conversion systems including high efficiency, reliability, modularity, fuel adaptability, and very low levels of NO_x and SO_x emissions. Quiet, vibration-free operation of solid oxide fuel cells also eliminates noise usually associated with

conventional power generation systems. Furthermore, because of their high temperature of operation (800~1000°C), natural gas fuel can be reformed within the cell stack eliminating the need for an expensive, external reformer system. Also, pressurized SOFCs can be successfully used as replacements for combustors in gas turbines; such hybrid SOFC-gas turbine power systems are expected to reach efficiencies approaching 70% (Singhal, 2000).

In addition to the wide applications described above, the solid oxide electrolyzer is used in our NASA-sponsored research program as an electrochemical apparatus (Figures 1.1 and 1.2) to generate pure oxygen from oxygen bearing gases such as carbon dioxide, water vapor, and air. Functioning as an effective oxygen generator, it has a wide variety of potential applications in space exploration. For example, it can be used to produce oxygen either from the predominantly carbon dioxide rich atmosphere of Mars, or from hydrogen or carbon reduction of the lunar regolith (Sridhar and Vaniman, 1995). The oxygen thus produced can be used for not only propulsion but also life support. The solid oxide electrolyzer can also be used aboard a space station for air revitalization in closed-loop life support. When oxygen is extracted by the electrolyzer from oxygen bearing gases in space, significant savings in launch mass and cost can be attained for both unmanned and manned missions. In unmanned missions such as the robotic return missions to Mars, the oxidizer for the return trip propellant can be replaced with a small oxygen production unit, thereby reducing both the launching mass from Earth and the landing mass on Mars. On the other hand, in manned missions, the oxygen produced can be used for both intraplanetary and interplanetary propulsion and life support.
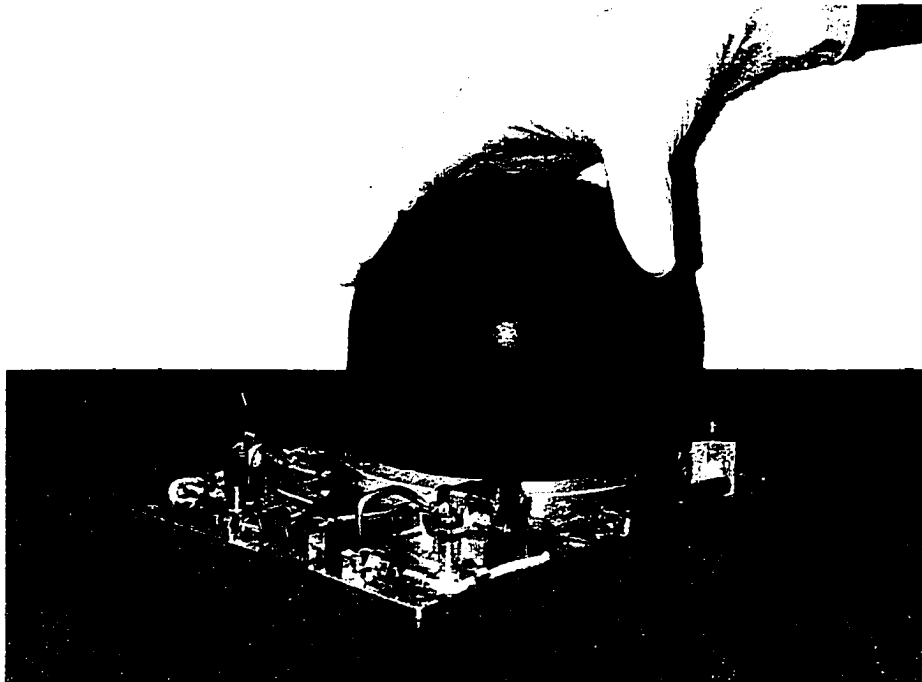
Figure 1. 1 Oxygen generator.
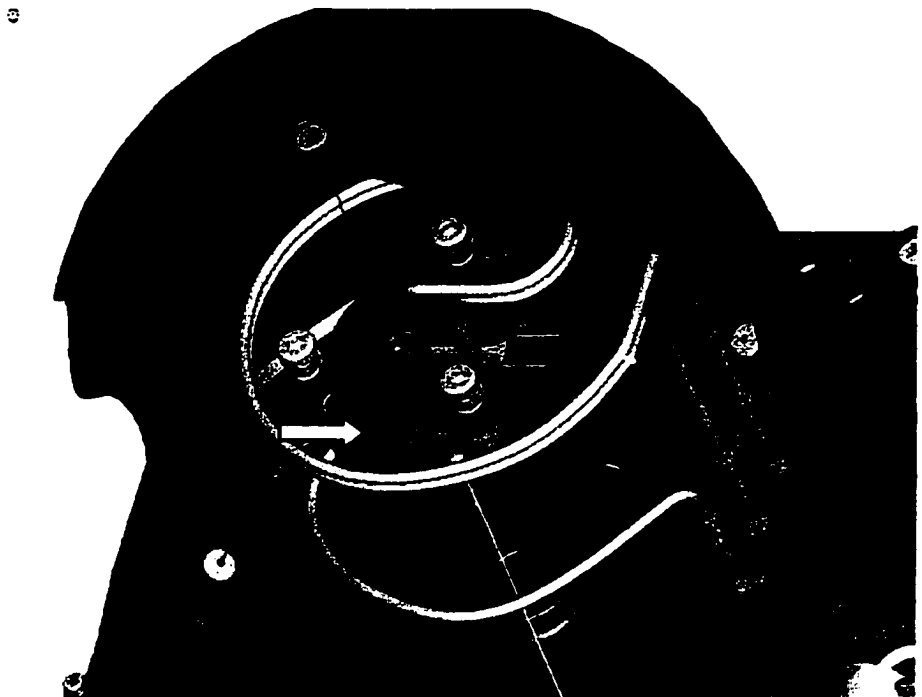
Figure 1. 2 Electrolyzer.

The critical part of the electrolyzer is a stack of electrochemical cell whose central

portion includes three different layers: two porous electrodes (an anode and a cathode)

separated by a dense, oxygen ion conducting electrolyte (Figure 1.3). Of these three

layers, the electrolyte is the oxygen-generating layer, which is usually made of a ceramic

solid oxide such as 8-mol% yttria stabilized zirconia (8YSZ).
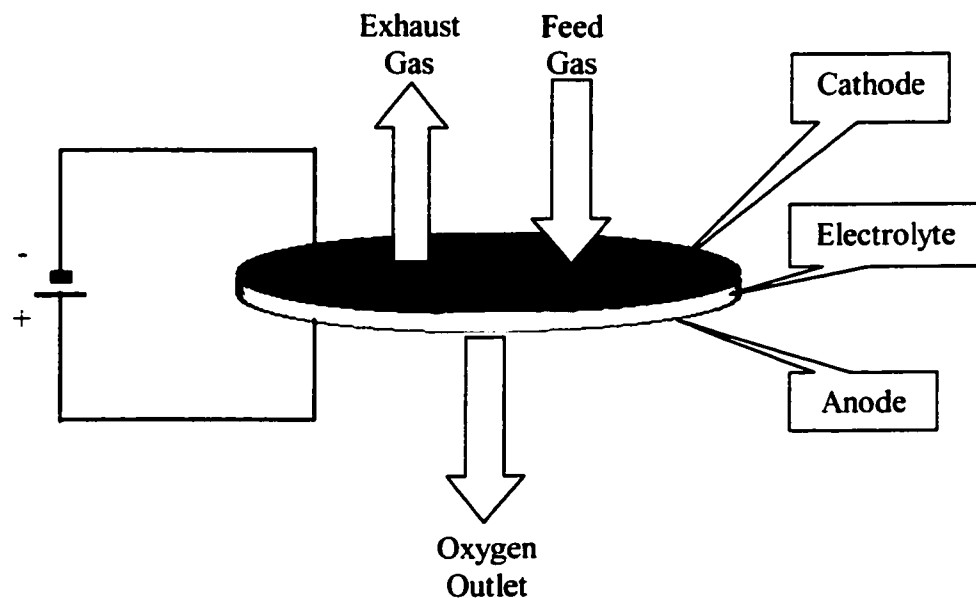
Figure 1. 3 A single cell of electrolyzer.

1.2 Mechanical properties for electrolyte material selection

The selection criteria for the electrolyte material are based on its physical and mechanical properties. The physical properties include elastic constants (Young's modulus and Poisson's ratio), thermal expansion coefficient, thermal conductivity, density, and electric conductivity. The most important is the electric conductivity, which directly associated with the oxygen production. The mechanical properties include strength, fracture toughness, and parameters of subcritical crack growth. The main characteristic of ceramics is brittleness. Brittleness means that failure occurs without prior measurable plastic deformation. This is due to the strong atomic bonding of ceramics, which lead to high stresses for the motion of dislocations. Thus, failure can start from small flaws before plastic deformation is possible. This fact can also be expressed as the low resistance against crack extension, which is characterized by the fracture toughness. The random distribution of sizes and locations of the small flaws in ceramic materials causes a large scatter of strength. This requires a statistical description of the strength and a relation between failure probability and stress distribution in a component. In addition, subcritical crack extension can cause failure under constant or cyclic loading during the operation of a component and will lead, consequently, to a limited lifetime.

The most widely used electrolyte material is 8YSZ due to its superior characteristics including cost, sintering behavior, chemical stability at high temperatures, oxygen conductivity over a wide range of oxygen partial pressures, and relatively proper

mechanical properties. The main disadvantages of 8YSZ are low tensile strength at room temperature, brittleness, large scatter of strengths, and subcritical crack extension.

Since the electric conductivity across the electrochemical cell decreases with the increasing thickness of the electrolyte, the electrolyte is usually made as a very thin sheet. The thin 8YSZ sheets (~0.5mm) that are used for electrolyte must be designed to withstand stresses of considerable magnitude which originate from launching, landing, gas pumping, and thermal expansion mismatch with supporting structure during thermal cycling between ambient temperature and working temperature.

1.3 Literature survey

Yttria stabilized zirconia (YSZ) has been studied for a long time. However, most researchers focused their attentions on partially yttria-stabilized zirconia such as 3-mol% yttria stabilized zirconia (3YSZ) because a phase transformation mechanism makes it possess a high toughness and high strength (Evans, 1984; Hannink, Kelly, and Muddle, 2000). Strength and fracture of yttria stabilized zirconia single crystals were studied by Ingel et al. (1982). Some measurements of strength and toughness on 8YSZ polycrystalline materials as well as some 8YSZ-containing composites have already been performed by several investigators (Winnubst, Keizer, and Burggraaf, 1983; Esper et al., 1983; Mori et al, 1994; Burelli, Maschio, and Lucchini, 1997; Selçuk, and Atkinson, 2000). However, most results showed large scatter and were impossible to be reliably

applied in practical design procedure. In the following, a brief review of the work having been done on 8YSZ is given.

Using biaxial-loading experimental method to obtain the biaxial flexural strength of ceramic thin substrate has been widely accepted. Selçuk and Atkinson tested type-cast 8YSZ by ring-on-ring method (Selçuk and Atkinson, 2000; Atkinson and Selçuk, 2000). They reported that mean flexural strength of 8YSZ is 416±70 MPa at room temperature (25 °C) and 265±39 MPa at 900 °C. A byproduct of the ring-on-ring method they obtained was the Young's modulus, E, of the material. They used the relation between the Young's modulus and the central deflection of the specimen under load, P, to estimate the value of E. They found this result was in good agreement with those from the standardized impulse excitation technique (IET) (Selçuk, and Atkinson, 1997). The average value of E was 216±5 GPa at room temperature and 155±8 GPa at 900 °C.

Selçuk and Atkinson (2000) also tried to relate the biaxial strength with the mode-I fracture toughness. They used Irwin's part-through crack extension model for semi-elliptical surface defects in brittle materials (Irwin, 1965) to predict the mode-I fracture toughness for their weakest specimen and obtained acceptable agreement with their experimental observations. The Irwin's model is

$$K_{IC} = \frac{\sigma_F M(\pi x)^{1/2}}{Y} \tag{1.1}$$

where K_{IC} is the mode-I fracture toughness, σ_F the fracture stress, M a numerical free-surface correction factor (0.795 in their bending condition), and x the crack depth. The

term Y is a shape factor for a semi-elliptical surface crack with a half-length of a, approximated by the equation

$$Y = \left[1 + 1.464 \left(\frac{x}{a} \right)^{1.65} \right]^{1/2} \qquad (1.2)$$

This approach was based on the "weakest link of a chain" assumption. Although they noticed that the specimens of high strength broke into many pieces, they assumed that this phenomenon was due to the crack branching during unstable crack propagation.

The mechanical properties of the fully stabilized 8YSZ, which is usually in cubic phase (Hannink, Kelly, and Muddle, 2000), can be modified by adding some additives such as alumina (Al_2O_3). The mechanical properties of composites of yttria stabilized zirconia and alumina (Al_2O_3) have been investigated by many researchers. Esper, Friese and Geier (1983) studied the mechanical, thermal, and electrical properties of the system of stabilized $ZrO_2(Y_2O_3)/\alpha$-Al_2O_3 . They concluded that the mechanical strength of the 7.5 mol% yttria stabilized zirconia could be increased by 50% by adding about 20 mass% alumina. Sušnik et al. (1997) reported the influence of alumina additive on the characteristics of cubic 8YSZ ceramic.

The fracture strength of 8YSZ as well as the composites of 8YSZ and Al_2O_3 has been examined as a function of Al_2O_3 content by Mori et al. in 1994. The temperature dependence of 3-point bending strength of 8YSZ showed a minimum at 500 °C. The strength of pure 8YSZ at 1000 °C was about 250 MPa, almost comparable to that at room temperature. The strength of the composites of 8YSZ and Al_2O_3 increased with Al_2O_3

content up to 20 wt%. The composite with 20-wt% Al_2O_3 showed a fracture strength of 320 MPa at room temperature. However, the experimental method they used was 3-point bending which applied a non-uniform uniaxial stress loading on the specimen. Their specimen dimension was 36 mm × 4mm × 3mm, which was not the geometry of the usually thin electrolyte in service. Therefore, these data need to be re-examined before using them for designing electrolyte since the loading condition and specimen geometry have significant effects on strength (Hoshide, Murano, and Kusaba, 1998).

The fracture strength data of 8YSZ as well as the composites of 8YSZ and Al_2O_3 have also been reported by Burelli et al. in 1997. Their data, shown in Table 1.1, further verified the statement that the loading condition and specimen geometry have effects on strength. In addition to the fracture strength, Burelli et al. also reported the fracture toughness trend against composition measured by two different experimental techniques. The fracture toughness increases approximately linearly with the increase of zirconia volume percentage up to 80%. The mode-I fracture toughness of pure yttria stabilized zirconia as well as Bi_2O_3 doped material was also studied by Winnubst, Keizer, and Burggraaf (1983) using indentation method.

The flexural strength of yttria-stabilized zirconia at elevated temperatures has also been studied. The fracture mode of cubic phase 6.5 mol% yttria stabilized zirconia was transgranular at low temperatures, mixed mode at intermediate temperatures (~500°C-1000°C), and intergranular at higher temperatures (Adams, Ruh, and Mazdiyasni, 1997). The four-point flexural strength of the hot-pressed and sintered Zyttrite yttria-stabilized zirconia showed a minimum value at about 760°C and 960°C, respectively.

Table 1. 1
Bending strength and Weibull modulus determined by monoaxial single bending and biaxial ball-on-ring tests

Composition	4-point bending σ (MPa)	Weibull modulus	Ball-on-ring σ (MPa)	Weibull modulus
Al_2O_3	242	11.6	350	9.4
Al_2O_3-ZrO_2 20-vol%	255	16.8	361	9.1
Al_2O_3-ZrO_2 40-vol%	402	20.4	508	10.4
Al_2O_3-ZrO_2 60-vol%	500	16.7	535	12.2
Al_2O_3-ZrO_2 80-vol%	500	17.3	574	14.1
ZrO_2	508	36.9	514	9.9

Although the strength data can be directly measured, the fracture mechanism study is important to the comprehensive understanding of the fracture strength. The fracture resistance and stable crack-growth behavior of the cubic-phase 8YSZ made by uniaxial powder pressing at room temperature has been carefully studied by Kumar and Sϕorensen (2000) at room temperature. They placed double-cantilever-beam specimens, which were loaded with pure bending moments in a specially designed loading fixture, inside an environmental scanning electron microscope (ESEM). Crack-growth data were obtained from truly sharp (arrested) cracks, bypassing the interpretation problems that involve crack initiation from a machined notch. Their crack-growth studies were conducted over a range of applied energy-release rates from crack arrest to fast fracture. The relation between crack-growth and energy-release rate was revealed as shown in Figure 1.4. Three critical energy-release-rate values were determined as follows:

- Energy-release-rate associated with crack arrest, G_a, is 2.8 J/m^2.

- Energy-release-rate associated with initiation of crack growth, G_i, is 3.5 J/m^2.

- Energy-release-rate associated with fast fracture, G_f, is 8.0 J/m^2.
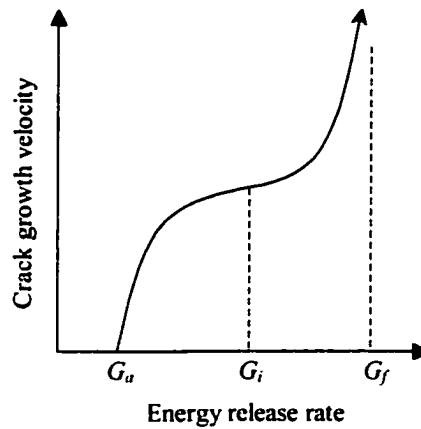
Figure 1. 4 The crack-growth velocity as a function of the applied energy-release rate.

The crack-growth behavior can be well illustrated by Figure 1.4. If applied energy-release rate is lower than G_a, no crack-growth will happen. When loading starts from an energy-release rate $G < G_a$, the load has to be increased to G G_i to initiate crack growth. Decreasing the energy-release rate will decrease the crack-growth velocity. If the energy-release rate is decreased to $G < G_a$, the crack growth is arrested. Then, energy-release rate has to be increased beyond G_a to G_i before further crack growth happens. The stable crack-growth occurs when the energy-release rate is between G_a and G_i, provided that the crack-growth has been initiated. Furthermore, Kumar and

Sⱷorensen identified that the fracture mode for stable crack-growth is transgranular while some (~5%-10%) intergranular fracture modes were observed in the fast-fracture region.

Several characteristic features were observed at the microscopic scale during the stable crack growth by Kumar and Sⱷorensen. These are grain bridging, branching, and secondary cracking, which are shown in Figure 1.5. Although these characteristic features can be material toughening mechanisms, 8YSZ possesses no obvious R-curve behavior because the occurrence rates of these characteristic features are too low. Typically, the formation of secondary cracks occurs about 10 times over a distance of 1 mm, the crack branching once over 10 mm, and grain bridging once over 200 μm. The grain size of their specimens was about 10 μm.

(a)   (b)   (c)
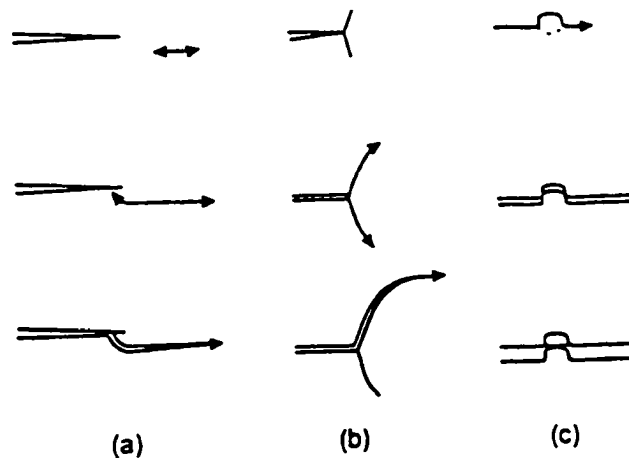
Figure 1. 5 Schematics of crack-growth process and mechanisms (a) formation of secondary cracks, (b) crack branching, and (c) grain bridging.

Failure mechanisms of 8YSZ ceramic at ambient and elevated temperatures were investigated by Lowrie and Raelings (2000). They found that sub-critical crack growth (sccg) occurred at both ambient temperature and 950°C, and was shown to be very sensitive to the applied stress.

1.4 Outline of this research

One of the final goals of the NASA-sponsored research program is to identify a proper material for the electrolyte in the oxygen generator, which can efficiently generate oxygen as well as possesses reasonable mechanical properties to ensure a high working reliability of the oxygen generator. The most important material property for such a material is electric conductivity as mentioned early. Researches from another group (Brach, 2000) have singled out some candidates, which are 8YSZ and its doped compositions with alumina and 3-mol% yttria stabilized zirconia (3YSZ). 8YSZ ceramic with less than 3-mol% alumina or 30-wt% 3YSZ will not degrade its electric conductivity significantly. To fulfill the eletrolyte material research, it is necessary to study the mechanical properties of these material candidates.

In order to integrate this study with the study of physical properties in another research group, the specimens prepared for this study are exactly the same as those specimens used for the study of physical properties. The specimen compositions studied in this research are listed in Table 1.2 with their aliases that will be used later on.

Table 1. 2
Composition of specimens

Composition	Alias
Pure 8YSZ	8YSZ
1 mol% Al_2O_3-doped 8YSZ	1A
2 mol% Al_2O_3-doped 8YSZ	2A
3 mol% Al_2O_3-doped 8YSZ	3A
10 wt% 3YSZ-doped 8YSZ	1Y
20 wt% 3YSZ-doped 8YSZ	2Y
30 wt% 3YSZ-doped 8YSZ	3Y

The specimens were made from TZ-8YSZ powder (TOSOH USA, Inc., Atlanta, GA). Standard specification of this powder provided by TOSOH is in Table 1.3. Typical properties of sintered material bulk with TOSOH-recommended heating schedule are listed in Table 1.4. The powder was mixed with dopants and was then processed into slurry with dispersant, binder, and plasticizer, and the slurry was tape-cast. Then, the specimens were laser-cut out of green sheets and sintered at 1450 C for 3 hours as recommended by TOSOH. The surface roughness of as-fired specimens is between 20 and 30 μm as observed with a Zeiss IM 35 inverted microscope. The geometry of the specimen is the one recommended by ASTM F 394-78: a thin cycle disk with 32-mm in diameter. An X-ray diffraction (XRD) analysis performed on the materials revealed that only the cubic phase was present in all these specimens (Brach, 2000).

Table 1. 3
Standard specification of TOSOH 8YSZ powder

Y_2O_3 (mol.%)	8
Y_2O_3 (wt%)	13.3 ± 0.60
Al_2O_3 (wt%)	≤ 0.1
SiO_2 (wt%)	≤ 0.02
Fe_2O_3 (wt%)	≤ 0.01
Na_2O (wt%)	≤ 0.12
Specific surface area (m^2/g)	7 ± 2

Table 1. 4
Typical properties of sintered material bulk with TOSOH 8YSZ powder

Density (g/cm^3)	5.90
Bending strength at room temperature (MPa)	300
Fracture toughness at room temperature (MPa $m^{0.5}$)	1.5
Hardness (HV10)	1250

It has been shown by Lawn and Wilshaw (1975) that if small dust particles are wedged between the undersurface of a specimen and the surface on which it is placed, the resulting stresses are sufficient to rupture bonds. Silicate glass is a very good example for demonstrating the importance of surface cracks. If the sizes of surface cracks are reduced by etching away some surface materials, the stress of the silicate glass can be increased several-fold (Jayatilaka, 1979). The effects of surface conditions on flexural strength of

yttria stabilized zirconia are also significant (Kosmač, Oblak, Jevnikar, Funduk, and Marion, 1999). Therefore, for research on strength improvement theory, microstructure design, and processing, the surfaces are usually prepared to be as free as possible of cracks not characteristic of the general microstructure. However, the surface condition of the specimens is usually made as close as possible to that to be used in service when the intention is to obtain strength data for design. This is the situation of this research. Therefore, the specimens used in this research will be kept as-fired. At this surface condition, the test results include all the factors that have effects on the biaxial flexural strength, such as material compositions and processing parameters, in addition to surface flaws. Nevertheless, the surface conditions of each specimen will be carefully examined whenever it is necessary.

Fracture strength and fracture strength distribution are the most commonly used properties for the design of ceramic components for advanced structural applications such as the solid oxide electrolyzer. Although many fracture strength data have been published by different investigators, these data are different from each other because the fracture strength of brittle materials depends on many factors such as materials' chemical compositions, processing parameters, loading conditions, and environmental conditions in service. Therefore, it is mandatory to measure the fracture strength for each single target application, although the general data in the literature are useful to serve as the references for the selection of candidate materials. Ceramic materials usually possess high compressive strength. Their tensile strengths are much lower and depend on the material properties such as fracture toughness and parameters of subcritical crack growth

as well as loading conditions and material processing parameters such as crack density. The research in this dissertation focuses on the tensile strength of the target material candidates under biaxial bending loading conditions.

In the next chapter of this dissertation, the piston-on-3-ball technique, an ASTM standard test method for the biaxial flexural strength of ceramic substrates at ambient temperature, is briefly discussed first with an analytical elastic solution of the stress distribution in the tensile surface of a specimen under such loading condition. Experiments with this technique on 8YSZ thin substrates and its doped versions are performed. Since strength data of brittle materials show large scatter, statistical processing of these data is necessary. However, there is no theory available about the distribution of the biaxial flexural strength data of brittle materials under the piston-on-3-ball loading condition. Therefore, a new theoretical proof is presented in chapter 3 that the well-accepted Weibull statistical treatment of the strength data of brittle materials under uniaxial loading conditions can also be applied to describe the scattering of the strength data under the piston-on-3-ball loading condition. The quasi-static experimental results with the piston-on-3-ball technique are then processed using the Weibull treatment.

The oxygen generator associated with this research is planned to be placed on a spacecraft. The eletrolyzer is then exposed to transient loading conditions during launching and landing. The ceramics possess different mechanical properties under high-speed loading conditions from those under static loading conditions (Grady, 1995). Therefore, it is mandatory to investigate the strength behavior of electrolyte material

under high-speed loading conditions. However, no dynamic experimental technique is available to obtain the strength data of ceramic substrates under biaxial loading conditions. In chapter 4, a new dynamic piston-on-3-ball experimental technique is proposed. Analytical model of the dynamic piston-on-3-ball technique is provided to guide the design of experimental facility and to judge the validity of the strength result obtained from each experiment. Finally, a new dynamic strength model under constant stress-rate is formulated to facilitate the description of the dynamic strength behavior of ceramic materials.

The electrolyzer works at elevated temperatures (800°C~1000°C). The strength behavior is different form that at room temperature (24°C) as mentioned early. Therefore, the experimental investigation of the strength behavior of the target material candidates at elevated temperatures is important to the design of a reliable oxygen generator. In chapter 5, the ASTM standard piston-on-3-ball experimental technique is modified to test the biaxial flexural strength of ceramic substrates at elevated temperatures.

Next, some comprehensive discussions about the effects of the dopants on the microstructures and macroscopic strengths of 8YSZ ceramic substrates are presented in chapter 6. In addition, a new Vickers micro-indentation toughness technique is developed in this chapter. The fracture toughness values measured with this new Vickers micro-indentation toughness technique, as well as SEM micro-structural observations, are combined together with the results of various piston-on-3-ball experiments to analyze the biaxial flexural strength behavior of 8YSZ ceramic substrate and its Al_2O_3 or 3YSZ doped versions.

The final conclusions and the work necessary to accomplish a complete research are discussed in chapter 7. In this chapter, some possible solutions to the strength problem of electrolyte ceramic substrates are proposed.

CHAPTER 2

QUASI-STATIC PISTON-ON-3-BALL EXPERIMENTAL TECHNIQUE

A number of techniques and methodologies have been developed for the measurement of fracture strength of ceramic materials. All of these techniques equate the fracture strength to the maximum stress in the specimen at fracture moment. Consequently, in order for a particular load and specimen geometry to be useful for the determination of fracture strength, the stress distribution must be well established. A complicating factor in the determination of fracture strength is that the strength of ceramic materials is quite sensitive to size, shape, and surface finish. This sensitivity is largely responsible for the wide variation in strength values often reported for a given material. To be viable, the test methodology must therefore account for these effects.

2.1 Ceramic test methods

In the US, the American Society for Testing and Materials (ASTM) has developed many standard test methods for advanced ceramics and ceramic composites. ASTM committee C28 on Advanced Ceramics has been responsible for the creation of

over 25 standards. All of the ASTM standard test methods can be classified into three catalogues.

- Uniform uniaxial stress loading.

- Nonuniform uniaxial stress loading.

- Biaxial stress loading.

Although uniform uniaxial stress loading, such as uniaxial tensile test (ASTM C 1273-95a, 1995) is conceptually simple, it is in empirical practice the most difficult to conduct satisfactorily. Analytically, this method is statically determinate, and the uniform stress state can be simply calculated as the axial load divided by the cross-sectional area of the gauge section. However, a geometric stress concentration in the gauge section is a major source of error. St. Venant's principle indicates that the effects of stress concentrations decay with distance from the load application site until the simplest, statically equivalent stress distribution is reached. Thus, the length of the uniform gauge section is chosen to achieve a uniform, uniaxial stress field relatively distant from smooth reductions in the specimen cross section leading from the loading point to the gauge section. Another major source of error is bending stresses resulted from nonaxial (eccentric) loading such as off-center loading, moment applied at ends, curved specimen, and twisting. Moments due to eccentricity applied at the end of the specimen will not decay with distance from the ends. The bending stresses often result in failure of brittle specimen during specimen-grip alignment procedure.

The most common experimental techniques of nonuniform uniaxial stress loading are three- and four-point bending (ASTM C 1211-92, 1995). Despite their wide utilizations, these experimental techniques are not without problem. Ferber, Wereszczak and Jenkins (1998) summarized the major sources of errors of these bending test methods. The main drawback of these test methods is the effects of specimen preparation upon the strength. In other words, the cut-surface finish has strong effects on the final test results. It is then necessary to carefully polish the specimen. Therefore, these test methods could not be used to study the effects of material processing parameters on the specimen in an as-fired state. Besides, the specimen geometry is a rectangular bar with a thickness required to be thicker than 2 mm. The solid oxide electrolytes are typically made by a tape-cast process. After sintering, the products are usually in the form of thin sheets. The thickness of these sheets is typically 0.5 mm or less in engineering applications. The three- and four-point bending experimental techniques thus are incompatible with the geometry of thin, tape-cast sheets.

2.2 Biaxial flexural test methods

Fracture in ceramic substrates mainly originates at a surface flaw. The strength of ceramic substrates is determined by surface condition in conjunction with internal microstructure rather than by internal microstructure alone. A valid test method for the purpose of obtaining strength data for design should permit the determination of the strength of specimens having the same surface condition that they have in service and

should not require any machining of a type not actually occurring in the normal use of the material. Most ceramic substrates are used with as-fired surfaces such as the electrolyte in this research program, so a test method capable of measuring strength on specimens in this condition is needed.

The strength of brittle materials such as ceramics depends significantly on specimen size and loading conditions (Weibull, 1939; Richerson, 1992; Hoshide, Murano, and Kusaba, 1998). The loading conditions in service on the electrolyte and many other applications such as SOFC, with a thickness of much less than 2 mm, often involve biaxial bending instead of simple tension or simple bending. Therefore, a biaxial experimental technique must be used for this research.

To obtain strength data under biaxial bending on thin sheets, ASTM standardized a piston-on-3-ball testing method for the biaxial flexural strength (modulus of rupture, MOR) of ceramic substrates (Wachtman, Capps, and Mandel, 1972; ASTM F 394-78, 1995). In such a test, a thin ceramic sheet is placed on three balls sitting 120° apart on a 25.4-mm-diameter circle. A piston pushes at the center of the circle from the other side of the ceramic sheet, thus producing a biaxial flexural loading condition. The area of maximum tensile stress thus falls only at the center of the lower surface of the specimen plate and the strength should be independent of the condition of the edges of the plate. A number of variations of this technique exist (Figure 2.1). For the loads to be more evenly distributed on the ceramic sheet, it has been proposed to replace the three supporting balls by a ring. Also, the piston could be replaced by a ball, a smaller ring, or simply pressure, resulting in new designs of the biaxial flexural testing configurations: ring-on-ring,

piston-on-ring, ball-on-ring, piston-on-3-ball, and ball-on-3-ball. The ring-on-ring (Kao, Perrone, and Capps, 1971; Fessler and Fricker, 1984; Hulm, Parker, and Evans, 1998) configuration involves supporting a circular plate on a ring and loading with a small concentric ring, which was the focus of a collaborative Japan-United States effort on development of low-cost aluminum nitride materials (Wallace et al., 1998). The ball-on-3-ball has a theoretical advantage over the other biaxial loading configurations in that there is no problem of assuring uniform loading over the surface of the piston and it is totally symmetric about the loading center. However, no exact elastic analysis for this loading configuration has been found. Rickerby developed a pressure-on-ring loading configuration (Salem and Jenkins, 1999), which can be considered a modified version of piston-on-ring loading configuration.
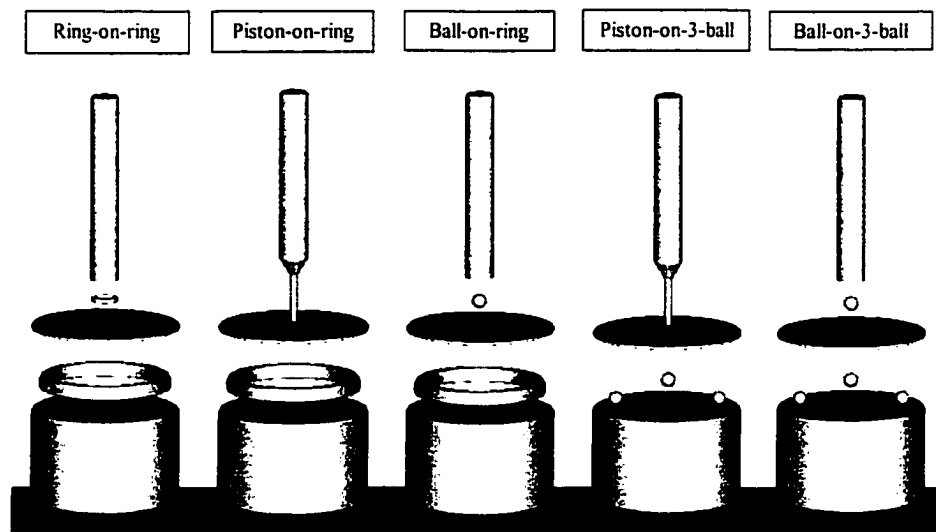
Figure 2. 1 Biaxial flexure loading configurations.

2.3 Quasi-static piston-on-3-ball biaxial flexural strength test method

Watchman et al. (Wachtman, Capps, and Mandel, 1972) presented a piston-on-3-ball experimental technique, which later became an ASTM standard (ASTM F 394-78, 1995). This technique has an advantage over many other ring-supported biaxial flexural strength measurement techniques in that three balls support the specimens, allowing the use of a slightly warped specimen, and no surface grinding or polishing is required. It is possible, therefore, to analyze the effects of processing parameters on the surface of the specimen using the piston-on-3-ball method.

2.3.1 ASTM standard piston-on-3-ball experimental technique

The quasi-static piston-on-3-ball biaxial flexural strength test method, an ASTM test standard, is a method used to measure the biaxial flexural strength of ceramic substrates at room temperature. The technique employs a compression piston-on-3-ball experimental fixture as in Figure 2.2. The three 3.18-mm-diameter balls are equidistant (120°) on a 25.4-mm-diameter circle. A thin 32-mm-diameter plate specimen is placed on the three balls with a 1.6-mm-diameter piston pushing the central portion of the specimen until the specimen is broken. The suggested loading rate should be such that the stress rate at the center of the specimen is 19.5 to 26.4 MPa/s. The experimental fixture and specimen dimensions are fashioned after the design by Wachtman et al. (Wachtman, Capps, and Mandel, 1972).
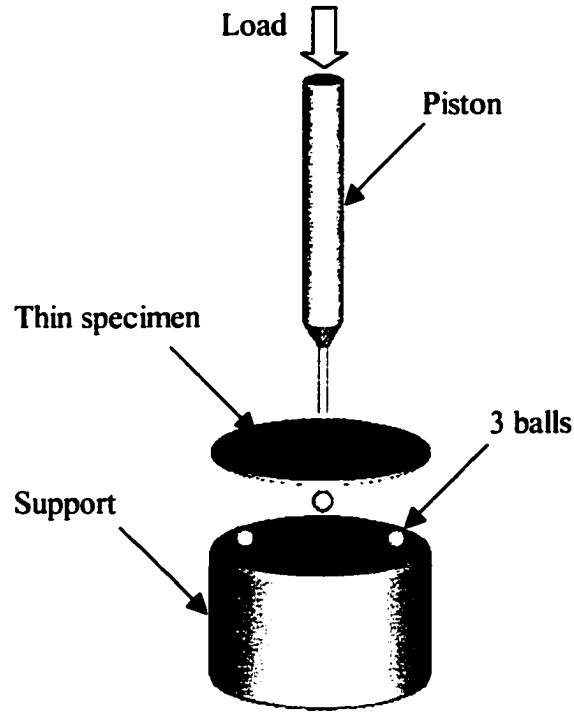
Figure 2. 2 Piston-on-3-ball experimental configuration.

The experiments can be performed using a hydraulically driven material testing system such as MTS 810 material test machine with piston load and central specimen deflection recorded simultaneously. Once the peak piston load at fracture is determined, the following equation provided by ASTM F 394-78 can be used to calculate the biaxial flexural strength.

$$\sigma_F = -\frac{3}{4\pi}\frac{P}{h^2}(X-Y)$$

(2.1)

where

σ_F = biaxial flexural strength (MPa),

P = load peak causing fracture (N),

h = specimen thickness at fracture origin (mm),

$$X = (1+\nu)\ln\left(\frac{r_2}{r_0}\right)^2 + \left[\frac{1-\nu}{2}\right]\left(\frac{r_2}{r_0}\right)^2,$$

$$Y = (1+\nu)\left[1+\ln\left(\frac{r_1}{r_0}\right)^2\right] + (1-\nu)\left(\frac{r_1}{r_0}\right)^2,$$

ν = Poisson's ratio,

r_0 = radius of specimen (mm),

r_1 = radius of support circle (mm), and

r_2 = radius of loading area (mm).

Although an ASTM standard exists for this experimental configuration, it has been argued that the piston-on-3-ball configuration applies a nonuniform stress and therefore introduces uncertainties in the calculation of the biaxial flexural strength. In experimental practice, it is not possible to produce uniform loading under a piston's whole cross section once deflection has been induced, even with the alignment fixtures developed for this purpose. Regardless of these introduced uncertainties, the technique remains popular because of its experimental convenience.

2.3.2 Analytical elastic solution to the stress distribution in the tensile surface of a

specimen under the piston-on-3-ball loading condition

Numerical method such as finite element method (FEM) can usually be employed to solve elastic problem with complicated structural geometry and external loading. However, numerical solution is difficult to be used for further formulation in a theoretical analysis procedure. Fortunately, the elastic problem with the piston-on-3-ball loading configuration has been analytically solved for small deflections (less than the specimen thickness).

Bassali (1957) formulated a general solution to the problem of flexure of a thin circular elastic plate supported at an arbitrary number of points, which may be located anywhere within the plate periphery, and loaded perpendicular to the plate over a circular area lying anywhere within the boundary of the plate. Kirstein and Woolley (1967) specified Bassali's theory to provide solutions to the problem of symmetrical bending of thin circular elastic plates on equally spaced point supports. With these solutions, the equations for evaluating the stress state on the tensile surface of the specimen plate can be formulated. The contribution of direct shear forces to the stress is ignored, which is justified by the fact that the thickness of the plate is much less than the in-plane dimensions, such that the plate can be considered as a slender structure.

Some of the parameters associated with the piston-on-3-ball loading configuration (Figure 2.2) are given in Figure 2.3. The in-plane stresses on the tensile surface are conveniently expressed in a polar coordinate system with normalized radius $\rho = r/r_0$ ($0 \leq$

$\rho \leq 1$), which starts from the center of the specimen surface, and polar angle θ, which starts from the positive X axis that passes through one of the supports.
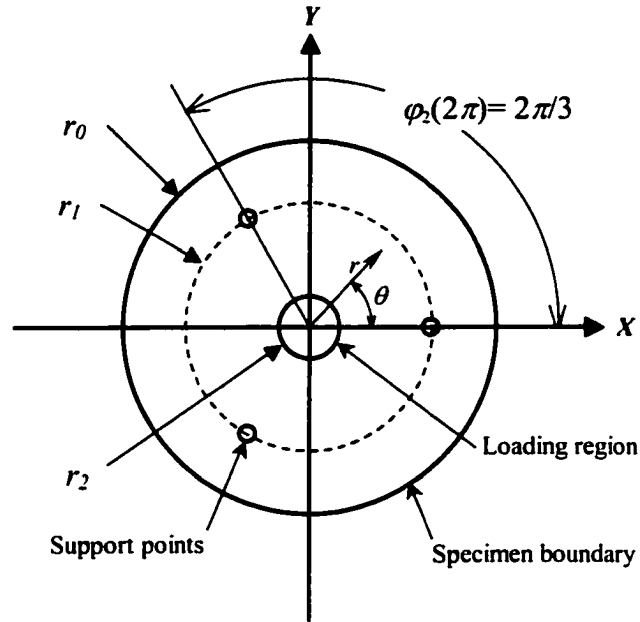
Figure 2. 3 Parameters in the piston-on-3-ball configuration: r_0 = radius of the plate specimen, r_1 = radius of the concentric support circle, r_2 = radius of the loaded area (radius of the piston), and $\varphi_i(\theta) = \theta - 2\pi i / 3$ ($i = 1,2,3$).

By using Kirstein and Woolley's equations for bending and twisting moments, the in-plane stresses on the tensile surface due to the out-of-plane load P can be derived as follows:

$$\sigma_{rr} = P \, \bar{f}_{rr}(\rho, \theta) \frac{6}{h^2} \qquad (2.2)$$

$$\sigma_{\theta\theta} = P \, \bar{f}_{\theta\theta}(\rho,\theta) \frac{6}{h^2}$$

(2.3)

and

$$\sigma_{r\theta} = P \, \bar{f}_{r\theta}(\rho,\theta) \frac{6}{h^2}$$

(2.4)

where h is the thickness of the plate, ρ is the normalized polar radius coordinate (r/r_0),

and $\bar{f}_{rr}(\rho,\theta)$, $\bar{f}_{\theta\theta}(\rho,\theta)$, and $\bar{f}_{r\theta}(\rho,\theta)$ are stress distribution functions that are

independent of loading levels and plate thickness and are expressed as follows:

$$\bar{f}_{rr}(\rho,\theta) = -\frac{1+\nu}{24\pi\kappa}\Psi + \frac{1-\nu}{48\pi\kappa\rho^2}\Theta$$

$$\bar{f}_{\theta\theta}(\rho,\theta) = -\frac{1+\nu}{24\pi\kappa}\Psi - \frac{1-\nu}{48\pi\kappa\rho^2}\Theta$$

$$\bar{f}_{r\theta}(\rho,\theta) = \frac{1-\nu}{24\pi\kappa\rho^2}\Phi$$

where κ is defined as $(3+\nu)/(\nu-1)$, ν is the Poisson's ratio, and Ψ is defined as

$$\Psi = \overline{\Psi} + \begin{cases} 6\kappa\ln q + \dfrac{3\kappa\rho^2}{q^2} - 3\kappa, & \rho \le q \\ 6\kappa\ln\rho, & \rho > q \end{cases}$$

with the first term defined as

$$\overline{\Psi} = \sum_{i=1}^{3}\overline{\Psi}_i - \frac{6t^2\left(1+\dfrac{\kappa q^2}{2-t^2}\right)}{\kappa+1} + 3\left(1+t^2\right)$$

$$\overline{\Psi}_i = \ln\left(1 - 2\rho t \cos\varphi_i + \rho^2 t^2\right) - \kappa \ln\left(\rho^2 - 2\rho t \cos\varphi_i + t^2\right) - \frac{\left(1-t^2\right)\left(1-\rho^2 t^2\right)}{1 - 2\rho t \cos\varphi_i + \rho^2 t^2}$$

where q is defined as r_2/r_0, and t is defined as r_1/r_0. In addition, Θ is defined as

$$\Theta = \overline{\Theta} + \begin{cases} -\dfrac{3\kappa\rho^4}{q^2}, & \rho \le q \\ -6\kappa\rho^2 + 3\kappa q^2, & \rho > q \end{cases}$$

with the first term defined as

$$\overline{\Theta} = \sum_{i=1}^{3}\overline{\Theta}_i + 3(\kappa-1)\left(\rho^2 - t^2\right)$$

$$\overline{\Theta}_i = \left(\kappa^2 - 1\right)\ln\left(1 - 2\rho t \cos\varphi_i + \rho^2 t^2\right) + \frac{\left(1-\rho^2 t^2\right)^2 - 2t^2\left(1-\rho^2\right)^2}{1 - 2\rho t \cos\varphi_i + \rho^2 t^2}$$

$$- \frac{\left(1-\rho^2\right)\left(1-t^2\right)\left(1-\rho^2 t^2\right)^2}{\left(1 - 2\rho t \cos\varphi_i + \rho^2 t^2\right)^2} + \frac{\kappa\left(\rho^2 - t^2\right)^2}{\rho^2 - 2\rho t \cos\varphi_i + t^2}$$

Φ is defined as

$$\Phi = \sum_{i=1}^{3}\Phi_i$$

$$\Phi_i = \frac{\rho t \sin\varphi_i\left(\rho^2 - t^2\right)}{1 - 2\rho t \cos\varphi_i + \rho^2 t^2} - \frac{\rho t \sin\varphi_i\left(1-\rho^2\right)\left(1-t^2\right)\left(1-\rho^2 t^2\right)}{\left(1 - 2\rho t \cos\varphi_i + \rho^2 t^2\right)^2}$$

$$- \frac{\kappa\rho t \sin\varphi_i\left(\rho^2 - t^2\right)}{\rho^2 - 2\rho t \cos\varphi_i + t^2} - \left(\kappa^2 - 1\right)\arctan\frac{\rho t \sin\varphi_i}{1 - \rho t \cos\varphi_i}$$

The stress distributions expressed by Equations (2.2)-(2.4) have a singular point at

the center of the plate where ρ is equal to zero. By further analysis of stresses at this point

(Kirstein and Woolley, 1967), it was concluded that the tensile stresses reach their maximum values at the center of the surface,

$$\sigma_{rr} = \sigma_{\theta\theta} = \sigma_b = P \bar{f_c} \frac{6}{h^2}$$ (2.5)

and

$$\sigma_{r\theta} = 0$$ (2.6)

where

$$\bar{f_c} = -\frac{(1+\nu)}{8\pi}\left[\frac{2t^2\left(1-\frac{q^2}{2t^2}\right)}{\kappa+1} + 2\ln\frac{q}{t} - 1\right]$$

As described by Equations (2.2)-(2.5), all the stresses are proportional to the piston load P and inversely proportional to the square of the specimen thickness. However, each stress has its own distribution function, independent of loading level, as described by $\bar{f_{rr}}(\rho,\theta)$, $\bar{f_{\theta\theta}}(\rho,\theta)$, and $\bar{f_{r\theta}}(\rho,\theta)$. Therefore, the stress distributions can be normalized by the stresses at the center. The normalized stress distribution functions $f_{rr}(\rho,\theta)$, $f_{\theta\theta}(\rho,\theta)$, and $f_{r\theta}(\rho,\theta)$ are independent of the piston load and the thickness of the specimen. In terms of $f_{rr}(\rho,\theta)$, $f_{\theta\theta}(\rho,\theta)$, and $f_{r\theta}(\rho,\theta)$, the stress distributions in the tensile surface of the plate can be expressed as follows:

$$\sigma_{rr} = \sigma_b \frac{\bar{f_{rr}}(\rho,\theta)}{\bar{f_c}} = \sigma_b f_{rr}(\rho,\theta)$$ (2.7)

$$\sigma_{\theta\theta} = \sigma_b \frac{\bar{f}_{\theta\theta}(\rho,\theta)}{\bar{f}_c} = \sigma_b f_{\theta\theta}(\rho,\theta) \tag{2.8}$$

and

$$\sigma_{r\theta} = \sigma_b \frac{\bar{f}_{r\theta}(\rho,\theta)}{\bar{f}_c} = \sigma_b f_{r\theta}(\rho,\theta) \tag{2.9}$$

With the stress components σ_{rr}, $\sigma_{r\theta}$, and $\sigma_{\theta\theta}$ known, the principal stresses at any

point (ρ,θ) on the tensile surface of the specimen can be calculated by

$$\sigma_1 = \frac{\sigma_{rr} + \sigma_{\theta\theta}}{2} + \sqrt{\left(\frac{\sigma_{rr} - \sigma_{\theta\theta}}{2}\right)^2 + \sigma_{r\theta}^2} = \sigma_b f_1(\rho,\theta) \tag{2.10}$$

and

$$\sigma_2 = \frac{\sigma_{rr} + \sigma_{\theta\theta}}{2} - \sqrt{\left(\frac{\sigma_{rr} - \sigma_{\theta\theta}}{2}\right)^2 + \sigma_{r\theta}^2} = \sigma_b f_2(\rho,\theta) \tag{2.11}$$

where the normalized principal stress distribution functions are

$$f_1(\rho,\theta) = \frac{f_{rr}(\rho,\theta) + f_{\theta\theta}(\rho,\theta)}{2} + \sqrt{\left(\frac{f_{rr}(\rho,\theta) - f_{\theta\theta}(\rho,\theta)}{2}\right)^2 + f_{r\theta}(\rho,\theta)^2} \tag{2.12}$$

and

$$f_2(\rho,\theta) = \frac{f_{rr}(\rho,\theta) + f_{\theta\theta}(\rho,\theta)}{2} - \sqrt{\left(\frac{f_{rr}(\rho,\theta) - f_{\theta\theta}(\rho,\theta)}{2}\right)^2 + f_{r\theta}(\rho,\theta)^2} \tag{2.13}$$

Therefore, the stresses on the tensile surface of a thin disk specimen under the

piston-on-3-ball loading condition are fully determined. In the next chapter, the stress

distribution outlined above will be employed to derive a statistical model to describe biaxial flexural strength behavior of ceramic substrates under the piston-on-3-ball loading condition.

2.4 Summary

The piston-on-3-ball loading configuration was determined to best fit our needs and be employed as an experimental technique to investigate the biaxial flexural strength of ceramic substrates.

The quasi-static piston-on-3-ball biaxial flexural strength test method has been developed as an ASTM standard test method used to measure the biaxial flexural strength of ceramic substrates at room temperature.

For the purposes of further formulation about the piston-on-3-ball loading configuration, stress distribution functions were formulated by using Bassali's (1957) theory, which was specified by Kirstein and Woolley to provide solutions to the problem of symmetrical bending of thin circular elastic plates on equally spaced point supports.

CHAPTER 3

QUASI-STATIC BIAXIAL FLEXURAL STRENGTH UNDER PISTON-ON-3-BALL LOADING CONDITION

The experimental results of the strength of a series of nominally identical ceramic specimens typically demonstrate considerable scatter. This phenomenon can be explained qualitatively as a result of the scatter in the size of the critical cracks responsible for the failure of a specimen of a certain size under certain loading conditions. Therefore, it is desirable to use a statistical means to describe the strength behavior of brittle materials.

In this chapter, statistical models of the strength of thin ceramic substrates with surface defects under piston-on-3-ball loading conditions are formulated using Batdorf's statistical theory and stress distribution functions derived in chapter 2. As will be shown, these models possess the form of a Weibull distribution function, making it possible to process the piston-on-3-ball biaxial flexural strength data using a Weibull treatment. During this study, it was noted that the thickness of the specimen had no effect on the failure distribution. Therefore, it was deemed that a reasonable thickness of the specimen disk could be selected for the piston-on-3-ball test in the case where the thickness is so small that the deflection of the center of the specimen exceeds half of the thickness (this thickness would invalidate the strength evaluation equation specified in ASTM F 394-78). The strengths of seven different compositions of 8YSZ with dopants were tested

using the piston-on-3-ball method under valid test conditions. The results were then processed using the derived models. The failure distributions of two different thickness groups of 8YSZ specimens were similar, verifying that the thickness, indeed, has no effect on the failure distribution.

3.1 Weibull distributions under uniaxial loading conditions

Ceramic strength data are typically scattered over a wide range (compared to metal materials) and must be processed statistically. The Weibull distribution has been widely used in processing ceramic strength data in order to account for the wide scattering of such data. Weibull's strength theory of brittle materials is a pure statistical model. Previous research activities have mostly been focused on the application of the Weibull distribution to interpret strength data on the basis of uniaxial loading conditions. The two-parameter Weibull distribution and mean strength for several test methods for a volume distribution of flaws are listed in Table 3.1, in which V is the volume of the specimen, σ_0 is a threshold value, m is the Weibull parameter, and Γ is the gamma function, which is defined by

$$\Gamma(z) = \int_0^\infty t^{z-1} \exp(-t) dt$$

It should be careful that V must be non-dimensional if σ_0 has dimensions of stress so that V should be expressed as V/V_0, where V_0 is some chosen unit volume. If V is instead absorbed into σ_0 then σ_0 must have dimensions of stress times $(\text{volume})^{1/m}$.

Table 3. 1
Two-parameter Weibull distribution and mean strength for several test methods with a volume distribution of flaws

Loading configuration	Probability distribution of strength $F(\sigma_F)$	Mean strength $\overline{\sigma}_F$
Tension	$1 - \exp\left[-\left(\dfrac{\sigma_F}{\sigma_0}\right)^m V\right]$	$\dfrac{\sigma_0}{V^{1/m}}\Gamma\left(1+\dfrac{1}{m}\right)$
Pure bending	$1 - \exp\left[-\left(\dfrac{\sigma_F}{\sigma_0}\right)^m \dfrac{V}{2(m+1)}\right]$	$\dfrac{\sigma_0}{V^{1/m}}[2(m+1)]^{1/m}\,\Gamma\left(1+\dfrac{1}{m}\right)$
Three-point bending	$1 - \exp\left[-\left(\dfrac{\sigma_F}{\sigma_0}\right)^m \dfrac{V}{2(m+1)^2}\right]$	$\dfrac{\sigma_0}{V^{1/m}}\left[2(m+1)^2\right]^{1/m}\,\Gamma\left(1+\dfrac{1}{m}\right)$
Four-point bending with load at the quarter points	$1 - \exp\left[-\left(\dfrac{\sigma_F}{\sigma_0}\right)^m \dfrac{V(m+2)}{4(m+1)^2}\right]$	$\dfrac{\sigma_0}{V^{1/m}}\left[\dfrac{4(m+1)^2}{m+2}\right]^{1/m}\Gamma\left(1+\dfrac{1}{m}\right)$
Four-point bending with load at the third points	$1 - \exp\left[-\left(\dfrac{\sigma_F}{\sigma_0}\right)^m \dfrac{V(m+3)}{6(m+1)^2}\right]$	$\dfrac{\sigma_0}{V^{1/m}}\left[\dfrac{6(m+1)^2}{m+3}\right]^{1/m}\Gamma\left(1+\dfrac{1}{m}\right)$

Although Weibull treatment of strength data of brittle materials has been widely applied under uniaxial stress loading conditions, there was no existing mechanism-based analytical method for deducing the statistics of fracture under more general stress states until Batdorf's theory was published (Batdorf and Crose, 1974; Batdorf and Heinisch, 1978; Batdorf and Chang, 1979; Batdorf and Sines, 1980). Specific models still need to be developed to properly process the strength results obtained from biaxial stress loading tests.

3.2 Statistical models for piston-on-3-ball loading

A physics-based statistical model must consider two key factors that dominate brittle fracture under multi-axial loading conditions—the statistical nature of fracture and the multi-axial stress state that causes the fracture. The statistics of fracture under multi-axial stresses have been studied by Batdorf and his co-workers (Batdorf and Crose, 1974; Batdorf and Heinisch, 1978; Batdorf and Chang, 1979; Batdorf and Sines, 1980) and by Evans (1978). Although Batdorf and his co-workers and Evans proposed two different theories for multi-axial fractures, Chao and Shetty (1990) proved that the theories were equivalent if the same fracture criterion and flaw size distribution were used. Furthermore, they developed failure probability formulations based on Batdorf's theory for the test configurations of uniaxial tension, three- and four-point bending, and the ring-on-ring method (Chao and Shetty, 1991). Although the intrinsic nature of multi-axial stress states near the crack tips was not accounted for, these models were an important advancement in the interpretation of the statistical nature of multi-axial brittle fractures.

The Weibull treatment of strength data is usually employed in the ASTM standard test methods for uniaxial flexural strength of ceramic materials (ASTM C 1161-94, 1995; ASTM C 1211-92, 1995; ASTM C 1273-95a, 1995). However, there is no suitable model to interpret the results obtained by the ASTM standard test method for the biaxial flexural strength of ceramic substrates (piston-on-3-ball method), perhaps due to the lack of statistical models for this loading configuration. Although rigorous theoretical proof does not exist, some researchers have heuristically fitted their piston-on-3-ball strength data with the standard Weibull distribution function and used the Weibull modulus to compare

the results obtained from three- and four-point bending tests that had uniaxial stress states at the specimen surfaces (Cattell et al., 2001). This use points out the need for an analytical statistical model for the piston-on-3-ball test configuration so the statistics of the test data can be interpreted, analyzed, and applied properly.

In the following, specific statistical models for the piston-on-3-ball method are formulated by following the same procedure used by Chao and Shetty (1991), who developed statistical models for many other loading conditions, such as uniaxial, three- and four-point bending, and ring-on-ring loading configurations. The formulations are based on studies by two research groups: Batdorf and Crose (1974), who developed a general statistical theory for the fracture of a brittle structure subjected to nonuniform multi-axial stresses, and Kirstein and Woolley (1967), who developed equations that could be used for evaluating the moments in the piston-on-3-ball loading configuration, which can then be used to derive formulations for evaluating the stresses in the tensile surface. Kirstein and Woolley's equations for the moments under piston-on-3-ball loading condition are summarized in the section 2.3.2.

The stresses in the tensile surface are the key to the application of Batdorf's theory. The resultant specific statistical models for biaxial brittle fracture are applied to the strength analysis of 8-mol% yttria stabilized zirconia (8YSZ) thin substrates under piston-on-3-ball loading conditions. Since the specimens are tested at as-fired conditions, the fractures are considered to be initiated at defects in the tensile surface where the most significant tensile stresses occur. By SEM examination of the fracture surfaces of the tested specimen, Selçuk and Atkinson (2000) revealed that the fracture of 8YSZ thin

substrates under ring-on-ring loading conditions was also initiated at defects in the tensile surface. Here, only statistical models with fractures caused by surface flaws are formulated. Multi-axial fractures initiated at volume flaws can be modeled in the same manner.

3.2.1 Statistical models

Batdorf and his co-workers developed a statistical theory for the fracture of brittle structures subjected to nonuniform multi-axial stress state (Batdorf and Crose, 1974; Batdorf and Heinisch, 1978; Batdorf and Chang, 1979; Batdorf and Sines, 1980). According to this theory, the probability distribution of strength under certain loading condition, which is also referred as the cumulative probability distribution or failure probability in the literature, due to surface defects is given by

$$F = 1 - \exp\left[-\int_A \int_0^{\sigma_h} \frac{\Omega}{2\pi} \frac{dN(\sigma_{cr})}{d\sigma_{cr}} d\sigma_{cr} dA \right] \tag{3.1}$$

where F is the probability distribution of strength; σ_{cr} is, according to Batdorf's definition, the remote critical normal stress that causes fracture when a uniform uniaxial stress is applied normal to the plane of a crack; σ_h is the highest value that σ_{cr} can achieve; A is the tensile surface area; and Ω is the solid angle containing the normals to all orientations for which the component of the applied stress normal to the crack plane is larger than σ_{cr}. In the case of a biaxial stress state (Figure 3.1), the solid angle is
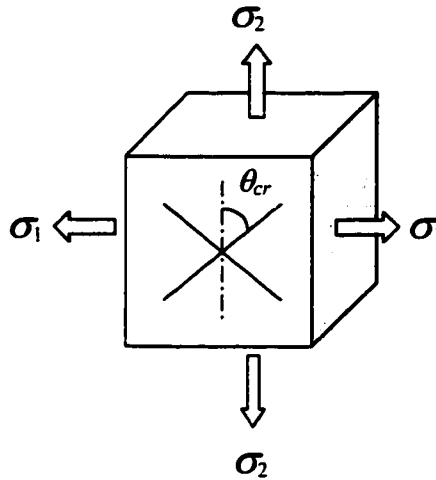
Figure 3. 1 Critical angle for randomly oriented surface cracks in a biaxial stress state.

$$\Omega = 4\theta_{cr} \tag{3.2}$$

where θ_{cr} is the largest angle of the orientation of the crack associated with the critical stress σ_{cr}. All the cracks associated with the critical stress σ_{cr} with orientation angles less than θ_{cr} will lead to fracture. $N(\sigma_{cr})$ is the crack size distribution function on the tensile surface, which gives the density of cracks having a critical stress less than or equal to σ_{cr}. Batdorf and coworkers proposed to represent $N(\sigma_{cr})$ by a Taylor series. However, Chao and Shetty (1991) used a relatively simple form for the crack size distribution function

$$N(\sigma_{cr}) = \bar{k} \; \sigma_{cr}^{m} \tag{3.3}$$

where $\bar{k}$ and m are the scale and shape parameters, respectively, in analogy to the Weibull parameters.

When Equation (3.3) is used to describe the crack size distribution, the probability distribution of strength has the form of

$$F = 1 - \exp\left[-\int_A \int_0^{\sigma_k} \frac{4\theta_{cr}}{2\pi} \overline{k} m \sigma_{cr}^{m-1} d\sigma_{cr} dA \right]$$

or

$$F(\sigma_b) = 1 - \exp\left(-\sigma_b^m \frac{2}{\pi} \overline{k} m I_B \right) \tag{3.4}$$

where the scale factor I_B is evaluated by

$$I_B = r_0^2 \int_0^{2\pi} \int_0^1 \int_0^{\sigma_k/\sigma_b} \theta_{cr} \left(\frac{\sigma_{cr}}{\sigma_b} \right)^{m-1} d\left(\frac{\sigma_{cr}}{\sigma_b} \right) \rho \, d\rho \, d\theta \tag{3.5}$$

and r_0 is the radius of specimen.

Chao and Shetty (1991) considered two failure criteria to determine the solid angle. The first one was the critical normal stress criterion, which considered failure to be determined solely by the mode I loading of a crack.

$$K_I = K_{IC} \tag{3.6}$$

where K_I is the mode I stress intensity factor and K_{IC} is the mode I fracture toughness of the material. The second failure criterion was the noncoplanar strain release rate criterion

$$\left(\frac{K_I}{K_{IC}} \right) + \left(\frac{K_{II}}{CK_{IC}} \right)^2 = 1 \tag{3.7}$$

where K_{II} is the mode II stress intensity factor and C is a constant. This equation was originally suggested by Palaniswamy and Knauss (1978) using the shear-sensitivity parameter C as

$$C = \sqrt{\frac{2}{3}} \approx 0.82.$$

Singh and Shetty (1989a) showed that C took values in the range of 1 to 2 for polycrystalline ceramics under combined mode I and mode II loading conditions. The higher the value of C, the lower the shear sensitivity of the material.

If the crack on the tensile surface is assumed to be in the shape of a half penny, the mode I and mode II stress intensity factors for a half-penny surface crack subjected to general remote loading are as follows (Kassir and Sih, 1966; Sih, 1984):

$$K_I = \frac{2M_I \sigma_N \sqrt{a}}{\sqrt{\pi}} \tag{3.8}$$

and

$$K_{II} = \frac{4M_{II} \tau \sqrt{a}}{\sqrt{\pi}(2-v)} \tag{3.9}$$

where σ_N and τ are normal and shear stresses, respectively, and M_I and M_{II} are free surface and stress gradient correction factors. Since M_I and M_{II} are approximately equal to each other (Smith and Sorensen, 1975; Newman and Raju, 1981), the two fracture criteria, Equations (3.6) and (3.7), become

$$\sigma_N = \sigma_{cr} \tag{3.10}$$

and

$$\frac{\sigma_N}{\sigma_{cr}} + \left[\frac{2\tau}{C(2-v)\sigma_{cr}} \right]^2 = 1 \tag{3.11}$$

For a general biaxial stress state at an arbitrary location on the tensile surface, the normal stress σ_N and shear stress τ can be evaluated as

$$\sigma_N = \frac{\sigma_1 + \sigma_2}{2} - \frac{\sigma_1 - \sigma_2}{2}\cos(2\theta) \tag{3.12}$$

and

$$\tau = -\frac{\sigma_1 - \sigma_2}{2}\sin(2\theta) \tag{3.13}$$

By substituting Equations (3.12) and (3.13) into the critical normal stress criterion, Equation (3.10), and using Equations (2.10) and (2.11), σ_{cr}/σ_b is found to be

$$\frac{\sigma_{cr}}{\sigma_b} = \frac{(f_1 + f_2)}{2} - \frac{(f_1 - f_2)}{2}\cos(2\theta_{cr}) = f_N(\rho,\theta,\theta_{cr}) \tag{3.14}$$

Furthermore, by applying differentiation to Equation (3.14), we obtain

$$d\left(\frac{\sigma_{cr}}{\sigma_b}\right) = (f_1 - f_2)\sin(2\theta_{cr})d\theta_{cr} \tag{3.15}$$

Therefore, by substituting Equations (3.14) and (3.15) into Equation (3.5), the scale factor I_B can be obtained as

$$I_B = r_0^2 \int_0^{2\pi} \int_0^1 \int_0^{\pi/2} \theta_{cr}[f_N \; H(f_N)]^{m-1}(f_1 - f_2)\sin(2\theta_{cr})\,\rho\,d\theta_{cr}\,d\rho\,d\theta \tag{3.16}$$

where $H(f_N)$ is the Heaviside step function. The reason for employing the Heaviside step function is to avoid counting the contributions from compressive normal stresses, since the compressive stresses normal to a crack will not cause fracture in brittle materials. An

analysis using the finite element method or Bassali's theory shows that the maximum principle stresses are compressive in the vicinity of the three support balls on the tensile surface. Therefore, fracture cannot occur there.

The noncoplanar strain release rate criterion takes both the mode I and mode II loadings into consideration, which is more proper for shear-sensitive materials. The scale factor for this criterion can be obtained by substituting Equations (3.12) and (3.13) into Equation (3.11) and using Equations (2.10) and (2.11). Therefore, σ_{cr}/σ_b and its differentiation are found to be

$$\frac{\sigma_{cr}}{\sigma_b} = G(\rho, \theta, \theta_{cr})$$

$$= \frac{f_N}{2} + \frac{\sqrt{C^2(2-v)^2 f_N^2 + 4(f_1 - f_2)^2 \sin^2(2\theta_{cr})}}{2C(2-v)}$$

(3.17)

and

$$d\left(\frac{\sigma_{cr}}{\sigma_b}\right) = \frac{\partial G(\rho, \theta, \theta_{cr})}{\partial \theta_{cr}} d\theta_{cr}$$

$$= \frac{8(f_1 - f_2)^2 \sin(2\theta_{cr})\cos(2\theta_{cr}) + 2\left(\frac{\sigma_{cr}}{\sigma_b}\right)C^2(2-v)^2(f_1 - f_2)\sin(2\theta_{cr})}{C^2(2-v)^2\left[4\left(\frac{\sigma_{cr}}{\sigma_b}\right) - (f_1 + f_2) + (f_1 - f_2)\cos(2\theta_{cr})\right]} d\theta_{cr}$$

(3.18)

In this case, the scale factor I_B is obtained as

$$I_B = r_0^2 \int_0^{2\pi} \int_0^1 \int_0^{\pi/2} \theta_{cr} [G \ H(f_N)]^{m-1} \frac{\partial G}{\partial \theta_{cr}} \rho \ d\theta_{cr} \ d\rho \ d\theta$$

(3.19)

3.2.2 Sensitivity of the scale factor

Equation (3.4), as well as Equations (3.16) and (3.19), shows that the probability distribution of strength of a thin ceramic substrate under the piston-on-3-ball loading condition is in the form of a Weibull distribution. The scale factor I_B is an important parameter in the probability distribution. Once the flaw size distribution function in the tensile surface, $N(\sigma_{cr})$, is determined, the smaller the scale factor I_B, the smaller the failure probability at a certain strength level. Therefore, the scale factor I_B can be used as an indicator of reliability. The studies of the sensitivity of the scale factor I_B to the Poisson's ratio are shown in Figures 3.2 and 3.3, with a specimen geometry (radius of specimen $r_0 = 15.9$ mm, radius of support circle $r_1 = 12.7$ mm, and radius of loading area $r_2 = 0.8$ mm) recommended by ASTM F 394-78 and a shape parameter $m = 7.1$.
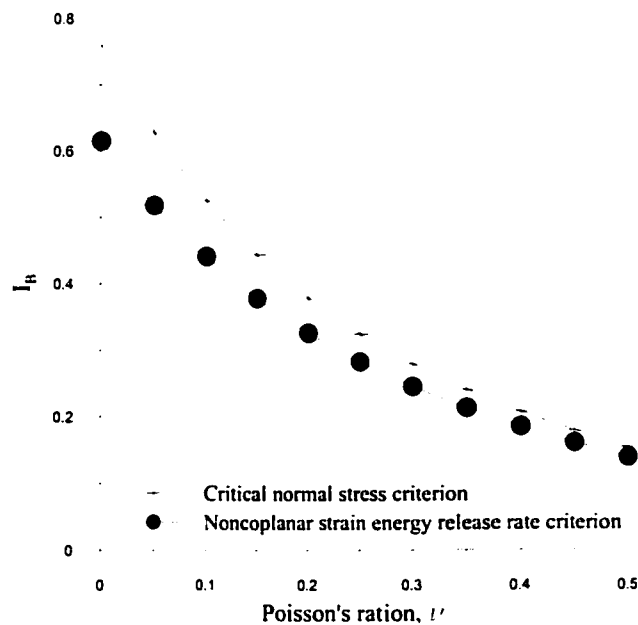
Figure 3. 2 Variation of the scale factor I_B for different fracture criteria ($C = 0.82$ for the noncoplanar strain energy release rate criterion).
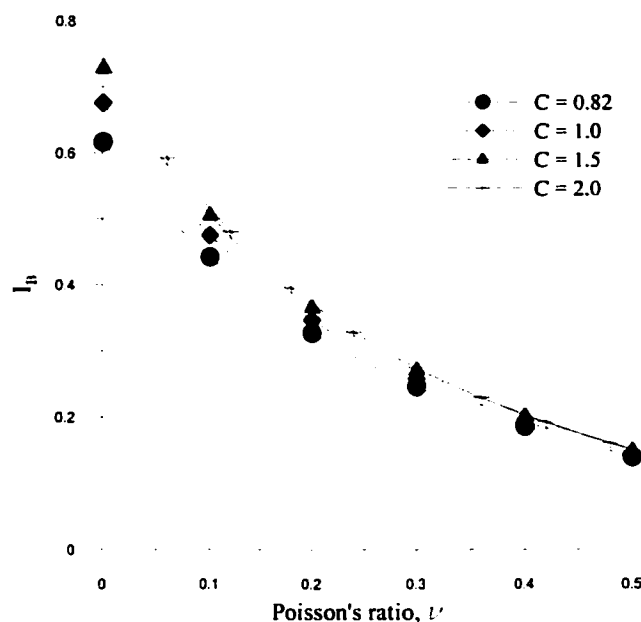
Figure 3. 3 Variation of scale factor I_B with the noncoplanar strain energy release rate fracture criterion with different values of the shear-sensitivity parameter C.

Figure 3.2 shows that the noncoplanar strain energy release rate criterion is safer to use than the critical normal stress criterion if the shear-sensitivity parameter C is chosen to be 0.82 as recommended by Palaniswamy and Knauss (1978), especially for brittle materials with small Poisson's ratios. This is because the noncoplanar strain energy release rate criterion takes mode II loading into account, in addition to the mode I loading.

Figure 3.3 shows that the scale factor I_B depends on the value of the shear-sensitivity parameter C. With C increasing from 0.82 to 2, the scale factor, I_B, increases. When checking the numerical values of these data, it was observed that the critical normal stress criterion is equivalent to the noncoplanar strain energy release rate criterion

provided the value of C is 2, which is the upper limit proposed by Shetty and coworkers (Shetty, 1987; Singh and Shetty, 1989a, b).

3.2.3 Discussions

With the cumulative probability distribution functions derived above, it has been proven that the Weibull distribution may also be used to describe the biaxial flexural strength of ceramic thin substrates under piston-on-3-ball loading conditions. As in the cases of three- and four-point bending experiments (Wachtman, 1996), the strength data can be fitted to a Weibull distribution function to obtain the Weibull parameters. In the case of piston-on-3-ball experiments, the Weibull shape parameter, m, and crack density scale parameter, $\bar{k}$, can be identified from a group of piston-on-3-ball test data. Equation (3.3) shows that these two parameters characterize the surface flaw population of the test material with associated specific material processing parameters. Therefore, they provide a method to estimate the fracture distribution of the same material with the same processing parameters, but with different geometry and loading conditions. For example, we can estimate the strength of a bar with three- or four-point bending conditions using the cumulative probability distribution formulations derived by Chao and Shetty (1991). Furthermore, with the stress distribution of a structure analyzed using a finite element program, the cumulative probability distribution can be numerically calculated following the same procedure as that applied to derive the cumulative probability distributions in this dissertation.

An important observation was made from the derivation of the cumulative probability distribution formulae. The thickness, h, of the specimen does not contribute anything to the final results as it is cancelled in the process of derivation, which can be seen in Equations (2.7)-(2.9). This is because we assumed that the fracture resulted from the surface defects. Changing the thickness does not change the surface crack distribution. Therefore, it provides us with a flexible way to prepare specimens. It is known from fracture mechanics that the geometry of the specimen has strong effects on the strength (Hoshide et al., 1998). Thus, in practice, the sizes of the specimens must be designed as close as possible to the sizes of the real structures. Sometimes, the actual structure must be designed to be very thin (< 0.5 mm), making its use as a specimen for piston-on-3-ball experiments impossible since such experiments require that the deflection of the specimen must be less than half of the thickness of the specimen to obtain valid data. When surface defects are the main fracture initiators, we can use test data from a group of reasonably thicker specimens to represent the fracture distribution of the thin structure.

3.3 Experimental results

The experiments were performed at room temperature with a hydraulically driven material testing system (MTS 810) with a piston moving speed of less than 1.27 $\mu m/sec$. The outputs of piston loading forces and specimen central deflection signals from the MTS 810 controller were recorded simultaneously using a National Instrument PCI-MIO-16XE-50 multifunction DAQ board that was installed in a personal computer. A data-acquisition control program was developed using LabVIEW 6i. Then, MATLAB 5.1 was used to process the original data. The statistics toolbox of MATLAB was used to do the Weibull analysis.

A typical loading trace is shown in Figure 3.4, which shows that the load increases linearly with deflection until failure, indicating a brittle failure at the peak load. The linearity of load with deflection is consistent with the analytical results derived by Kirstein et al. (1966).

The strength data were evaluated by the peak load using the equation for the stress at the center of the tensile surface, Equation (2.1). The Poisson's ratios for these material compositions are chosen to be 0.315 as suggested by Selçuk and Atkinson (2000), since Poisson's ratio for YSZ ceramics is reported in literatures to be 0.30~0.32 and is relative insensitive to both composition and temperature (Kandil, Greiner, and Smith, 1984; Hendriksen and Jørgensen, 1996).
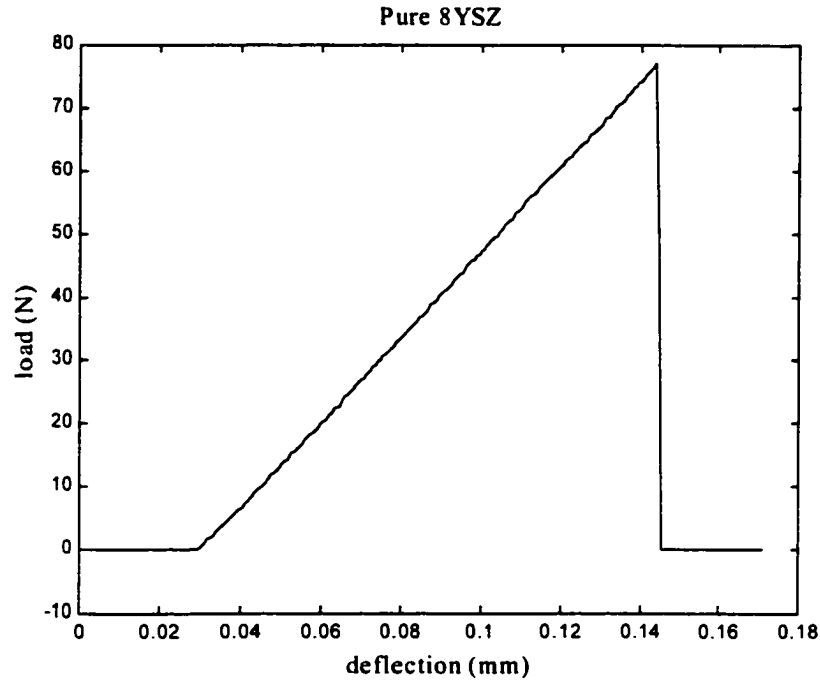
Figure 3. 4 A typical loading trace of the piston-on-3-ball experiment.

Table 3.2 lists the strength data obtained from the piston-on-3-ball experiments. Then, the data were fitted to the Weibull cumulative probability distribution function using the method of maximum likelihood (Jayatilaka, 1979),

$$F(\sigma_b) = 1 - \exp\left[-\left(\frac{\sigma_b}{\sigma_0}\right)^m V_e \right] \tag{3.20}$$

where $F(\sigma_b)$ is the probability distribution of strength, σ_b is the fracture stress, σ_0 is a scale factor which usually take a value of the mean of the fracture stress data, V_e is a effective volume which is a representative volume in analogy to the volume term in a standard Weibull distribution function such as those listed in Table 3.1, and m is the Weibull modulus.

Table 3. 2
Biaxial flexural strength data (MPa) from quasi-static piston-on-3-ball experiments at ambient temperature

8YSZ (h = 0.76 mm)	8YSZ (h = 0.41 mm)	1A	2A	3A	1Y	2Y	3Y
348.5	375.2	353.2	317.8	333.9	301.8	321.1	267.4
355.7	360.1	344.1	318.9	336.6	182.7	339.3	357.5
285.8	469.8	397.1	260.7	254.0	245.3	335.2	362.1
306.6	344.0	336.1	285.7	402.6	326.1	292.0	284.6
280.1	387.4	219.4	299.6	320.8	307.4	267.8	351.6
296.3	318.2	268.4	276.7	349.9	250.9	368.2	406.0
256.7	451.0	382.2	249.5		251.8	375.3	324.6
346.4	327.3	313.5	301.9		233.2	262.0	330.6
335.4	336.5	290.2	309.0		245.8	346.0	411.2
333.3	236.0	330.1	349.7		212.1	314.3	330.4
330.3	387.5	306.0	290.8		257.3	301.0	
337.1	248.3	296.9	208.0		308.7	245.1	
273.5	273.4	346.9	243.6		232.9	306.7	
302.7	437.6	271.9	230.9		194.9	277.4	
321.2		286.7	210.2		290.4	309.9	
355.0		357.7			288.8		
249.2		378.2			271.3		
283.9					292.3		
337.5					293.6		

303.9	185.3
382.6	301.3
381.2	302.7
280.3	267.9
356.2	319.2
179.6	284.6
363.5	265.0
393.2	271.5
339.1	95.4
274.1	159.9
297.4	172.9
388.9	367.6
218.2	263.8
210.9	
275.3	
299.4	

In the case of piston-on-3-ball biaxial flexural strength experiments, the scale factor of the crack size distribution function [see Equation (3.3)], is

$$\bar{k} = \frac{\pi}{2} \frac{1}{m I_B} \frac{V_e}{\sigma_0^m}$$

(3.21)

The data are shown as linearized Weibull plots in Figures 3.5~3.11, and the associated Weibull parameters are listed in Table 3.3.
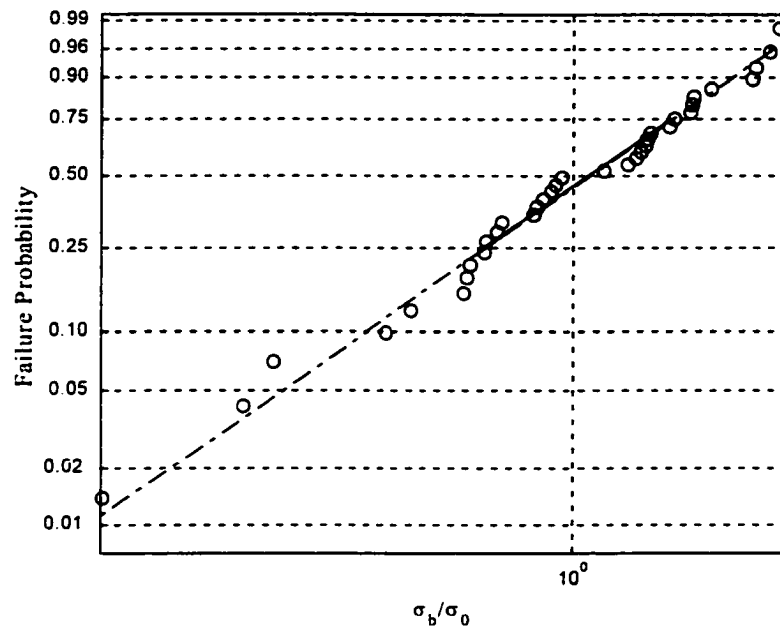
Figure 3. 5 Weibull probability plot of the biaxial flexural strength of 8YSZ from the piston-on-3-ball experiments at ambient temperature.
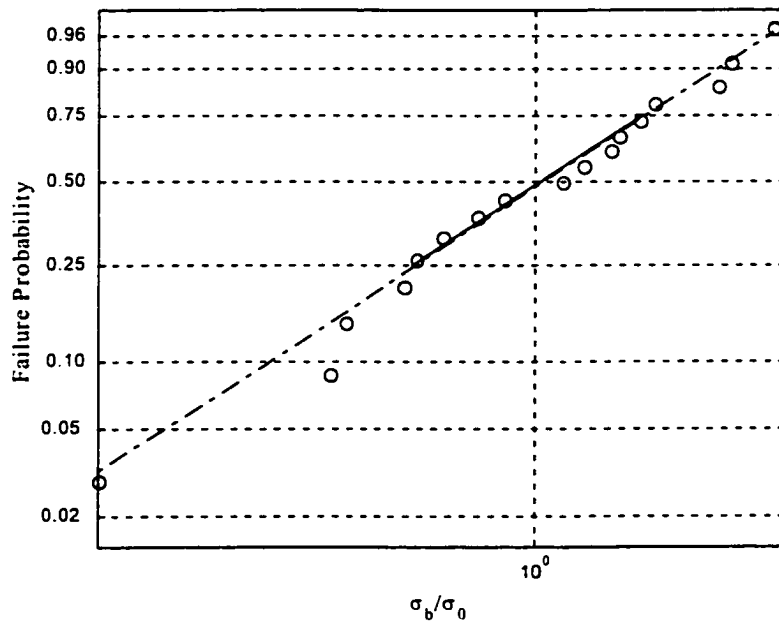
Figure 3. 6 Weibull probability plot of the biaxial flexural strength of 1A from the piston-on-3-ball experiments at ambient temperature.
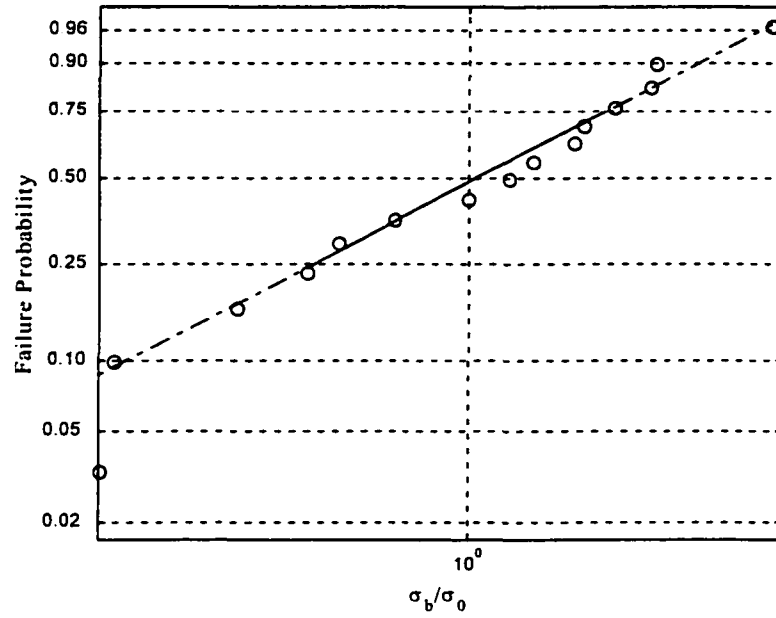
Figure 3. 7 Weibull probability plot of the biaxial flexural strength of 2A from the piston-on-3-ball experiments at ambient temperature.
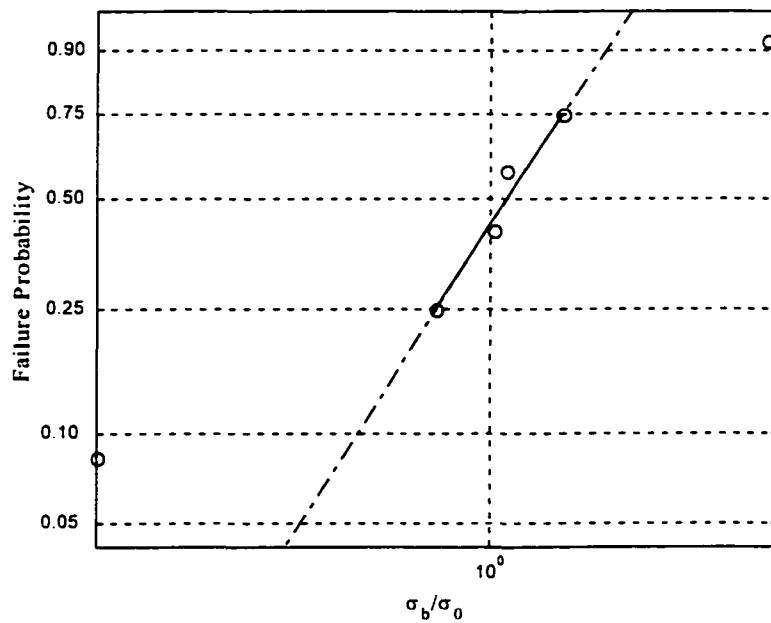
Figure 3. 8 Weibull probability plot of the biaxial flexural strength of 3A from the piston-on-3-ball experiments at ambient temperature.
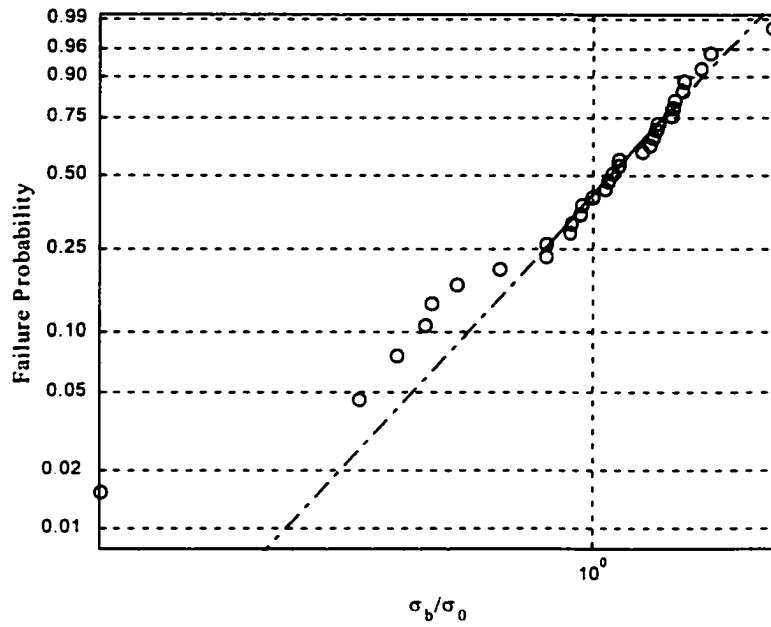
Figure 3. 9 Weibull probability plot of the biaxial flexural strength of 1Y from the piston-on-3-ball experiments at ambient temperature.
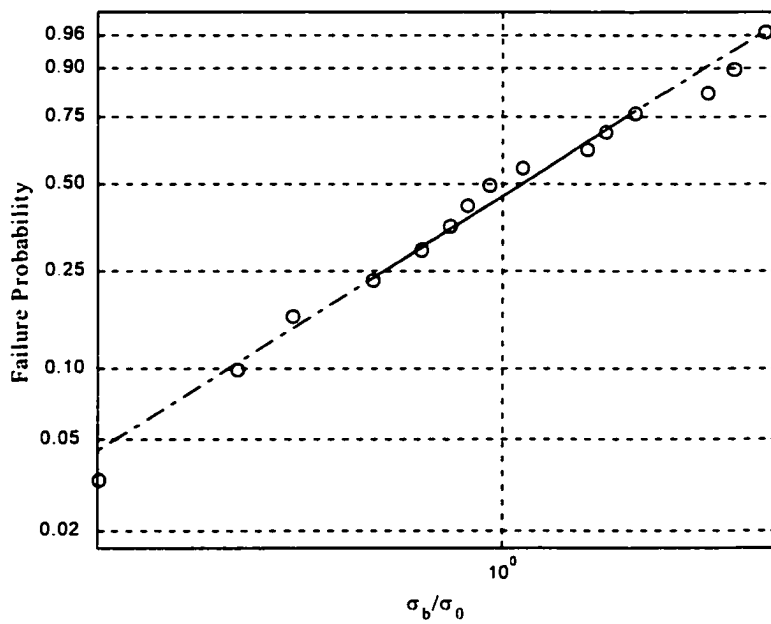
Figure 3. 10 Weibull probability plot of the biaxial flexural strength of 2Y from the piston-on-3-ball experiments at ambient temperature.
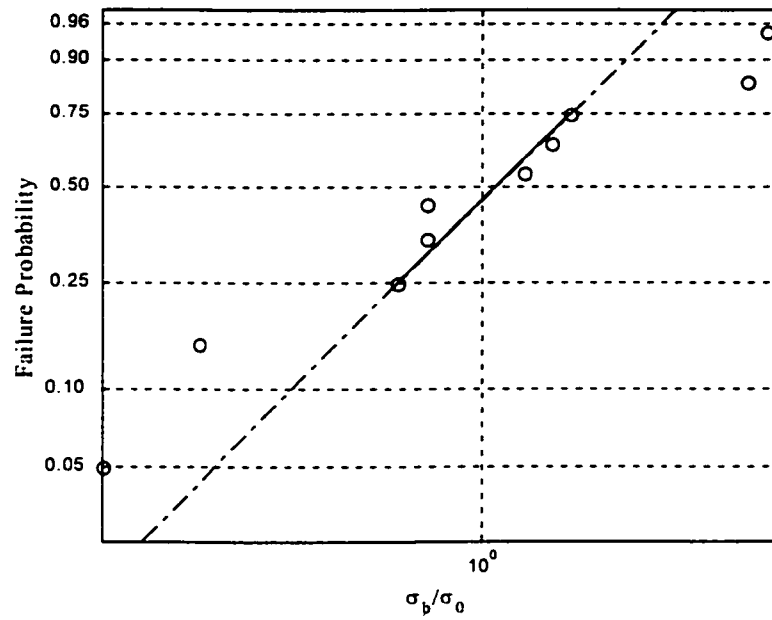
Figure 3. 11 Weibull probability plot of the biaxial flexural strength of 3Y from the piston-on-3-ball experiments at ambient temperature.

Table 3. 3
Weibull parameters fitted from experimental results and biaxial flexural strengths at ambient temperature

Ceramic Alias	Weibull Parameters		Strength (MPa)	
	m	V_c	Mean	std.
8YSZ	7.44	0.62	310.8	51.1
	(5.24, 9.65)*	(0.40, 0.84)		
1A	8.36	0.61	322.3	46.9
	(4.51, 12.21)	(0.31, 0.92)		
2A	7.93	0.62	276.9	41.9
	(4.30, 11.56)	(0.30, 0.93)		
3A	8.69	0.62	333.0	48.0
	(2.13, 15.25)	(0.14, 1.10)		
1Y	5.68	0.64	257.6	56.5
	(4.37, 7.00)	(0.40, 0.87)		
2Y	10.04	0.61	317.4	37.7
	(4.48, 15.60)	(0.29, 0.92)		
3Y	8.81	0.62	342.6	46.0
	(2.69, 14.92)	(0.24, 1.00)		

* Inside the brackets is the 95% confidence interval.

In order to verify that the thickness of specimen does not contribute to the final cumulative probability distribution form, another group of 8YSZ specimens with different thickness were tested. The results are shown in Figure 3.12 and listed in Table 3.4. The 95% confidence intervals of the Weibull parameters from these two groups of tests overlap and their mean strengths are close to each other. These test results also

verify the validity of the new model for biaxial flexural strength under piston-on-3-ball

loading conditions developed in this study.
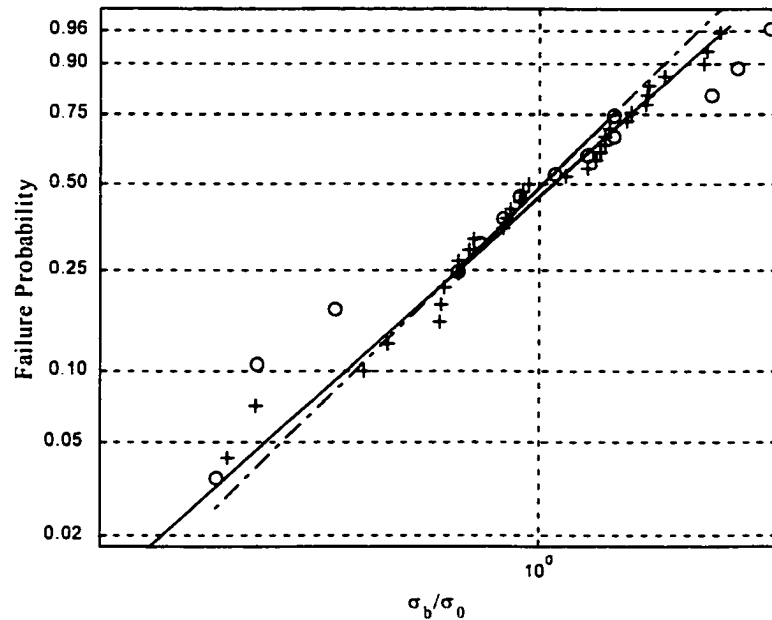
Figure 3. 12 Weibull probability plots of the biaxial flexural strengths of 8YSZ with different thickness (+, solid line, h = 0.76 mm; o, dashed line, h = 0.41 mm) from the piston-on-3-ball experiments at ambient temperature.

Table 3. 4
Weibull parameters and biaxial flexural strength for 8YSZ with different specimen thickness

Thickness (mm)	Weibull Parameters		Strength (MPa)	
	m	V_c	Mean	std.
0.76	7.44	0.62	310.8	51.1
	$(5.24, 9.65)^*$	$(0.40, 0.84)$		
0.41	5.83	0.64	342.6	46.0
	$(2.62, 9.04)$	$(0.30, 0.98)$		

* Inside the brackets is the 95% confidence interval.

3.4 Summary

Failure probability distribution function formulae for piston-on-3-ball loading conditions have been derived following Chao and Shetty's (1991) procedure for surface defects and using Batdorf's theory for biaxial flexural bending statistical model (Batdorf and Crose, 1974; Batdorf and Heinisch, 1978; Batdorf and Chang, 1979; Batdorf and Sines, 1980), and Bassali's (1957) theory for the evaluation of biaxial flexural bending stresses. The final formulae are in a form of the Weibull cumulative probability distribution function. Therefore, the experimental data from piston-on-3-ball tests can be processed with the Weibull treatment. The Weibull parameters are proven to be the characteristics of the population of surface defects. Therefore, these Weibull parameters can be used to predict the failure behavior of the tested material under other loading conditions.

Seven different compositions of 8YSZ with dopants were tested using the piston-on-3-ball method. The experimental results were processed using the Weibull treatment. The experimental data of 8YSZ with different thickness verify the fact that the thickness of the specimen does not have an effect on the failure probability distribution, which is derived from the statistical models. This fact indicates that the fracture of the 8YSZ substrates is indeed a result of surface defects.

CHAPTER 4

DYNAMIC BIAXIAL FLEXURAL STRENGTH UNDER PISTON-ON-3-BALL LOADING CONDITION

In this chapter, a dynamic piston-on-3-ball experimental technique is developed for a biaxial flexural strength test of thin ceramic substrates at high loading rates. Analytical modeling of the technique guides the experimental design and is used to judge the validity of experimental results.

Although material models have been proposed to describe the dynamic constitutive behavior of brittle materials under constant strain-rate loading, few efforts can be found to explain such dynamic behavior under constant stress-rate loading, which is the condition presenting many dynamic experimental techniques and is significant in practical use. In this chapter, a new model for dynamic strength under constant stress-rate loading for brittle materials is formulated based on the concept of cumulative damage. Pure and doped ceramic material 8YSZ thin sheets are tested with the newly developed dynamic piston-on-3-ball method under high stress-rate loading conditions. The experimental results with the dynamic piston-on-3-ball loading as well as those with the quasi-static piston-on-3-ball loading presented in chapter 3 are used to determine the constants in this new model. The model is found to give a good description of the dynamic constitutive behavior of brittle thin sheets under biaxial bending.

4.1 Dynamic piston-on-3-ball technique

The solid oxide electrolyzer on a spacecraft has to survive impact and vibration during launching from Earth and landing on other planets in order to produce oxygen in-situ, which is critical to return missions and human space exploration. It is mandatory to ensure the structural integrity of the electrolyzer over the duration of the entire space mission, which also calls for reliable multiaxial strength data under dynamic loading conditions. Unfortunately, there is a lack of experimental techniques that can provide such critical data for thin and brittle sheets of materials. In this section, an experimental method is presented that can determine the dynamic biaxial flexural strength (dynamic modulus of rupture). This new technique is based on a quartz-crystal-embedded split Hopkinson pressure bar (Chen, Lu, and Zhou, 2000) and the piston-on-3-ball testing configuration. The desired dynamic loading rates can be properly controlled under laboratory conditions. The range of loading rates from which valid data can be obtained is analytically determined. Using this new technique, the loading rate effects on the modulus of rupture of 8YSZ thin substrates are determined.

4.1.1 Experimental setup

Although a hydraulically driven material testing system can also provide a ramp loading with flexible adjustments to control parameters, it is not proper to perform an impact test since the limited dimensions of the system prevent the possibility to obtain the transmitted force signal without overlapping with the reflected signal. Since no pure

transmitted force signal available, it is impossible to judge if the specimen is in a force equilibrium state, which is important to avoid the inertial effects on the test results. In addition, the load cells used on a hydraulically driven material testing system is based on a strain gage technique, which offer only a limited frequency response range that is usually not wide enough for an impact test.

In order to maintain the same experimental conditions, except for the loading rates, the test section of the dynamic piston-on-3-ball experimental facility is identical to the test section of the standard quasi-static piston-on-3-ball setup. The configuration of the dynamic piston-on-3-ball method is shown schematically in Figure 4.1.
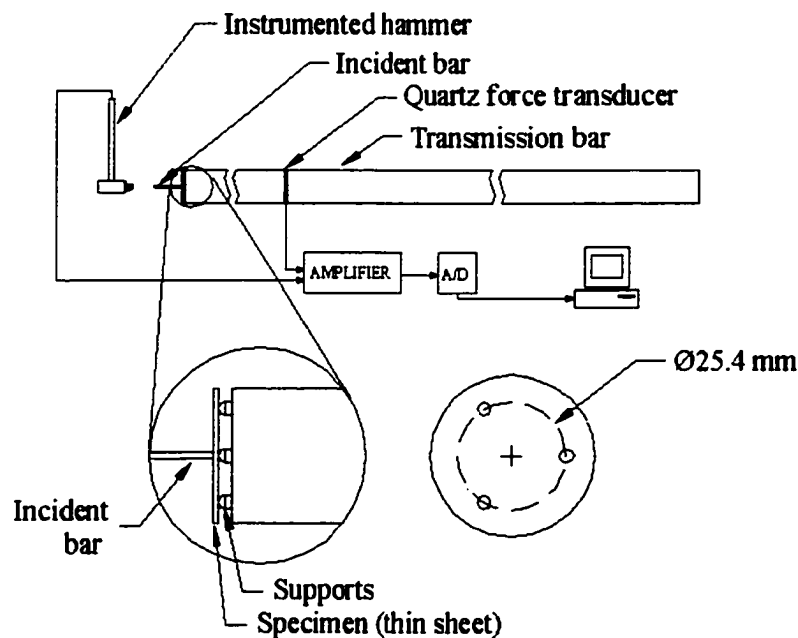
Figure 4. 1 A schematic of the dynamic piston-on-3-ball setup.

The working principle of the new method is similar to that of a split Hopkinson pressure bar (SHPB) (Graff, 1975; Gray, 2000). A valid SHPB test should be the same as a quasi-static compression test except for the loading rates. Similarly, the dynamic piston-on-3-ball test is the same as its standard quasi-static counterpart except for the loading rates.

In the experimental setup shown in Figure 4.1, a PCB impact hammer (model 086C01), which can output the impulse force signal by its embedded force transducer and adjust the impulse shape (loading rate) by applying different hammer tips, is used as the dynamic load generator. The incident bar is made of stainless steel with a diameter of 1.60 mm and a length of 80 mm. The thin specimen is supported by three 3.18-mm-diameter ball bearings. All of the parameters associated with the piston-on-3-ball setup are the same as those suggested in the ASTM standard F 394-78. The transmission bar is made of a 32-mm-diameter 7075-T6 aluminum alloy bar with a Valpey-Fisher X-cut quartz crystal disk of the same diameter embedded in the middle of the bar about 560 mm from the end close to the specimen to directly measure the time-resolved transmitted force. This quartz-crystal-embedded transmission bar technique can significantly increase the signal-to-noise ratio (SNR) during a SHPB test of a weak material without affecting the wave propagation (Chen, Lu, and Zhou, 2000). A National Instrument NI6110 A/D board, whose sampling rate per channel can be up to 5 MS/s, is used to sample the force signals from the hammer and quartz. A computer program developed using LabVIEW 6i is used to control the sampling processes during experiments.

The test procedure for the dynamic piston-on-3-ball experiment is similar to that of a SHPB test (Gray, 2000). An impulse load is applied on the center of the ceramic substrate specimen by the hammer through the incident bar. Part of the loading pulse is then transmitted through the specimen to the transmission bar. The time-resolved impulse forces in the hammer and the transmission bar are recorded simultaneously. Because of the wave propagation effects, the force signal from the transmission bar possesses a phase delay to the force signal from the hammer. The specimen is broken when the impulse force applied by the hammer reaches a high enough amplitude. The impulse peak and the loading rate can be determined from the recorded signals. Once the load peak is determined, the biaxial flexural strength, σ_F, at the center of the specimen surface in tension can be calculated using equation (2.1) derived by Kirstein and Wooley (1967) for quasi-static experiments, which requires the forces on both sides of the ceramic substrate to be in equilibrium.

To obtain the dynamic material strength data without the effects of inertia, which is commonly associated with impact loading, the forces on both sides of the specimen must be nearly the same during a dynamic experiment. If inertia effects are included in the axial force records, material strength data cannot be determined reliably, resulting in an invalid dynamic experiment. To examine if the specimen is in dynamic force equilibrium, the impulse force histories from both the hammer and the transmission bar are recorded; the loading rates can then be calculated from these two force records. The specimen is considered to be in dynamic equilibrium if these two loading rates are nearly equal to each other before the specimen is broken. When the loading rate exceeds a

certain level, it will be impossible to achieve dynamic force equilibrium. As discussed in the next section, this sets the upper limit of the loading rate for this experimental method.

4.1.2 Design of valid dynamic experiments

To evaluate the biaxial flexural strength of thin substrates without the effects of inertia using equation (2.1), it is necessary to maintain the dynamic force equilibrium on the specimen through the employment of a nearly constant slope ramp-loading. A ramp-loading pulse eliminates axial acceleration over most of the loading duration. This requirement of equilibrium limits the range of the allowable loading rates within which the dynamic force equilibrium can be achieved. Similar to the case of understanding the valid strain rate range in SHPB experiments on ceramics (Ravichandran and Subhash, 1994a), it is important to know the limits of the loading rate for valid results on biaxial flexural strength. The loading rate and the frequency components of a force pulse can be determined approximately by its amplitude and duration. To determine if a specific loading profile can produce valid data, it is necessary to determine the first resonant frequency of the specimen within the specific boundaries of the experimental setup. If the highest frequency component of the loading pulse is much lower than the first resonant frequency of the specimen, the specimen is approximately in its equilibrium state. Furthermore, if the loading rate is nearly constant, the brittle specimen will deform at a nearly constant velocity, which eliminates the inertia effects. To study the problem of specimen dynamic equilibrium, the experimental configuration is modeled as a multi-body dynamic system as shown in Figure 4.2.
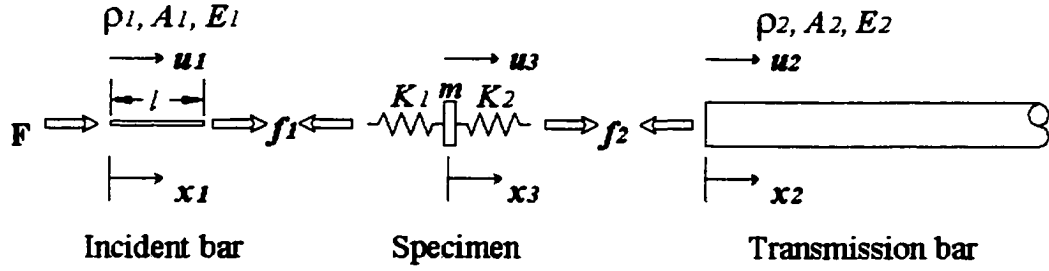
Figure 4. 2 Free-body diagrams of the analysis model.

In this model, the ceramic substrate specimen is modeled as a single-degree mass-spring system with mass m and elastic constants K_1 and K_2 because only the frequencies under the first mode of the disk are concerned. The elastic constants K_1 and K_2 of the springs can be assumed to be half the elastic constant obtained from quasi-static piston-on-3-ball experiments on the ceramic substrate. The incident bar is modeled as a short longitudinal rod with length l, cross-section area A_1, Young' modulus E_1, and material density ρ_1, while the transmission bar is modeled as a half infinite-length longitudinal rod with cross-section area A_2, Young's modulus E_2, and material density ρ_2. The loading pulse, F, generated by the hammer is applied to one end of the incident bar. The coordinate x and displacement u with subscript 1 are associated with the incident bar, while those with subscript 2 are associated with the transmission bar. One-dimensional wave propagation theory is used to model the waves in the two bars.

In general, the equation of motion for a straight and constant cross-section rod is

$$\frac{\partial^2 u}{\partial x^2} - \frac{1}{c_0^2}\frac{\partial^2 u}{\partial t^2} = 0 \qquad (4.1)$$

where $c_0 = \sqrt{E/\rho}$ is the bar wave velocity in the elastic rod. The D'Alembert solution

(Graff, 1975) to this equation is

$$u(x,t) = f(x - c_0 t) + g(x + c_0 t) \tag{4.2}$$

The first term on the right-hand side represents a forward-moving wave and the second a

backward-moving wave. In an idealized half infinite-length longitudinal rod such as the

transmission bar, only a forward-moving wave exists. In a short bar such as the incident

bar, waves travel back and forth and overlap each other.

To facilitate the computer simulation, spectral analysis method based on a discrete

Fourier transform (DFT) (Doyle, J., 1989) is applied. Therefore, Equation (4.2) can be

transformed into

$$u(x,t) = \sum_{n=0}^{N-1} U(x;n) e^{i\omega_n t} \tag{4.3}$$

where N is the length of the DFT, $U(x;n)$ are the DFT components of the displacement

$u(x,t)$, ω_n is the angular frequency, and n is an index. Substitution of Equation (4.3) into

(4.1) yields an ordinary differential equation, which has a solution as

$$U(x,n) = ae^{-ikx} + be^{ikx} \tag{4.4}$$

where $k = \omega_n/c_0 = \omega_n \sqrt{\rho/E}$. The coefficients a and b are undetermined amplitudes that

depend on each frequency. Substitution of Equation (4.4) back into Equation (4.3) yields

the final solution, which includes a forward-moving wave and a backward-moving wave as the D'Alembert solution,

$$u(x,t) = \sum_{n=0}^{N-1} a e^{-i(kx-\omega_n t)} + \sum_{n=0}^{N-1} b e^{i(kx+\omega_n t)}$$

(4.5)

Equation (4.5) is a general DFT solution to the longitudinal wave propagation in rods and can be applied to both incident and transmission bars. However, the second term does not exist in the transmission bar where no backward-moving waves exist. Therefore, the displacements of the incident bar and transmission bar are

$$u_1(x,t) = \sum_{n=0}^{N-1} a_1 e^{-i(k_1 x - \omega_n t)} + \sum_{n=0}^{N-1} b_1 e^{i(k_1 x + \omega_n t)}$$

(4.6)

and

$$u_2(x,t) = \sum_{n=0}^{N-1} a_2 e^{-i(k_2 x - \omega_n t)}$$

(4.7)

Boundary conditions must be applied to determine the coefficients a_1, b_1 and a_2. One end of the incident bar is subjected to the load F(t) generated by the hammer. The other end is resisted by force f_1, which is from the spring K_1. When the bar material is linearly elastic, both forces can be related to the respective displacement gradient at the bar ends in the forms of

$$E_1 A_1 \left. \frac{\partial u_1(x_1, t)}{\partial x_1} \right|_{x_1 = 0} = F(t) = \sum_{n=0}^{N-1} F(n) e^{i\omega_n t}$$

(4.8)

and

$$E_1 A_1 \left. \frac{\partial u_1(x_1,t)}{\partial x_1} \right|_{x_1=l} = f_1(t) = \sum_{n=0}^{N-1} f_1(n) e^{i\omega_n t} \tag{4.9}$$

The end of the transmission bar is subjected to the force f_2, which is the resistive force of the spring K_2,

$$E_2 A_2 \left. \frac{\partial u_2(x_2,t)}{\partial x_2} \right|_{x_2=0} = f_2(t) = \sum_{n=0}^{N-1} f_2(n) e^{i\omega_n t} \tag{4.10}$$

The lumped mass of the specimen moves according to Newton's second law,

$$f_2 - f_1 = m \frac{d^2 u_3}{dt^2} \tag{4.11}$$

which should vanish in an ideal dynamic experiment. In addition, the linear elasticity of the springs is described by

$$f_1 = K_1 [u_3 - u_1(l,t)] \tag{4.12}$$

and

$$f_2 = K_2 [u_2(0,t) - u_3] \tag{4.13}$$

These boundary conditions can be written in terms of the corresponding Fourier components as follows:

$$-ik_1 E_1 A_1 a_1 + ik_1 E_1 A_1 b_1 = F \tag{4.14}$$

$$-ik_1 E_1 A_1 e^{-ik_1 l} a_1 + ik_1 E_1 A_1 e^{ik_1 l} b_1 = f_1 \tag{4.15}$$

$$-ik_2 E_2 A_2 a_2 = f_2 \tag{4.16}$$

$$f_2 - f_1 = -m\omega_n^2 U_3 \tag{4.17}$$

$$f_1 = K_1 U_3 - K_1 a_1 e^{-ik_1 l} - K_1 b_1 e^{ik_1 l} \tag{4.18}$$

$$f_2 = K_2 a_2 - K_2 U_3 \tag{4.19}$$

In matrix form, Equations. (4.14) – (4.19) are written as follows:

$$
\begin{bmatrix}
-ik_1 E_1 A_1 & ik_1 E_1 A_1 & 0 & 0 & 0 & 0 \\
-ik_1 E_1 A_1 e^{-ik_1 l} & ik_1 E_1 A_1 e^{ik_1 l} & 0 & -1 & 0 & 0 \\
0 & 0 & ik_2 E_2 A_2 & 0 & 1 & 0 \\
0 & 0 & 0 & -1 & 1 & m\omega_n^2 \\
K_1 e^{-ik_1 l} & K_1 e^{ik_1 l} & 0 & 1 & 0 & -K_1 \\
0 & 0 & K_2 & 0 & -1 & -K_2
\end{bmatrix}
\begin{bmatrix}
a_1 \\
b_1 \\
a_2 \\
f_1 \\
f_2 \\
U_3
\end{bmatrix}
=
\begin{bmatrix}
F \\
0 \\
0 \\
0 \\
0 \\
0
\end{bmatrix}
\tag{4.20}
$$

While these equations can be solved explicitly, an examination of the dynamic equilibrium of the specimen by means of analyzing the transfer function between f_1 and f_2 will be made here. From Equation (4.20), the transfer function, $H_1(\omega_n)$, between f_1 and f_2, which should be unity in an ideal experiment, can be solved.

$$H_1(\omega_n) = \frac{f_2}{f_1} = \frac{1}{\left(1 - \dfrac{m\omega_n^2}{K_2}\right) + i\left(\dfrac{m\omega_n}{A_2\sqrt{\rho_2 E_2}}\right)} \tag{4.21}$$

Since the parameters m and K_2 are determined by the material and geometry of the specimen, and ρ_2 and E_2 are determined by the transmission bar material (aluminum alloy), the only parameter that can be adjusted is the cross-sectional area A_2 of the transmission bar. Increasing A_2 can reduce the deviation of H_1 from unity. However, the choice of A_2 depends on the cross-sectional area of the available quartz embedded in the

transmission bar. A typical variation of H_1 as a function of frequency is shown in Figure 4.3, with the parameters taken from the experimental setup for this research, where the specimen mass m is 3.314×10^{-3} kg, the specimen elastic constant K_2 is 0.3569×10^5 N/m, the transmission bar cross-sectional area A_2 is 7.9173×10^{-4} m^2, the transmission bar material density ρ_2 is 2800 kg/m^3, and the transmission bar material Young's modulus E_2 is 72 GPa. As shown in Figure 4.3, the first resonant frequency is

$$f_r^{H_1} = 1651.7 \text{ Hz}$$
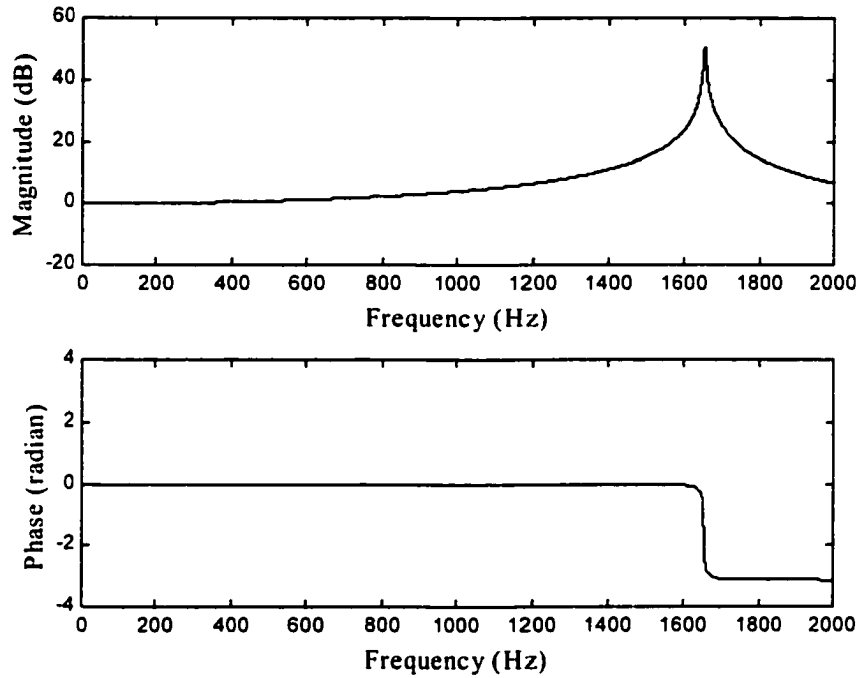
Figure 4. 3 Variation of $f2/f1$ ratio with frequency ($m = 3.314 \times 10^{-3}$ kg, $K_2 = 0.3569 \times 10^5$ N/m, $\rho_2 = 2800$ kg/m^3, $A_2 = 7.9173 \times 10^{-4}$ m^2, and $E_2 = 72$ GPa).

Figure 4.3 also shows that the specimen is approximately in the equilibrium state

if the applied load is bandlimited within H_l's 3-dB point,

$$f_b^{H_1} \leq 892.7 \, \text{Hz}$$

Equation (4.21) is very illustrative in determining the highest frequency

component of the force pulse that can pass through the specimen without significant

dispersion. In practice, however, it is not convenient to use in judging if the specimen is

in the equilibrium state, because the frequency analysis of the signal f_1 is impossible since

the time history of f_1 is not available. Therefore, another tool must be devised to ensure

specimen equilibrium.

Equation (4.20) also facilities the transfer function H_2 between F and f_2, which is

the dynamic force response at the point of the quartz force transducer in the transmission

bar due to the applied load of the hammer.

$$H_2(\omega_n) = \frac{f_2}{F} = \frac{2\lambda}{\gamma_1(1-\lambda^2)\left\{\left[\frac{1+\lambda^2}{\gamma_1(1-\lambda^2)} - \frac{1}{K_1}\right]\left[1 - \frac{m\omega_n^2}{K_2} - \frac{m\omega_n^2}{\gamma_2}\right] - \frac{1}{m\omega_n^2}\right\}} \tag{4.22}$$

where $\gamma_1 = ik_1E_1A_1$, $\gamma_2 = ik_2E_2A_2$, and $\lambda = e^{ik_1l}$. The time histories of both F and f_2 are

available from the signal records of a test.

A typical transfer function, H_2, whose parameters are m $(3.314\times10^{-3}$ kg), K_l

$(0.3569\times10^5$ N/m), K_2 $(0.3569\times10^5$ N/m), l (0.08m), ρ_l $(7800$ kg/m$^3)$, A_l $(2.0111\times10^{-6}$

m$^2)$, E_l $(200$ GPa$)$, ρ_2 $(2800$ kg/m$^3)$, A_2 $(7.9173\times10^{-4}$ m$^2)$, and E_2 $(72$ GPa$)$ is shown in

Figure 4.4. Again, these are the actual values used in this research. The first resonant

frequency is

$$f_r^{H_2} = 1344.4 \text{ Hz}$$
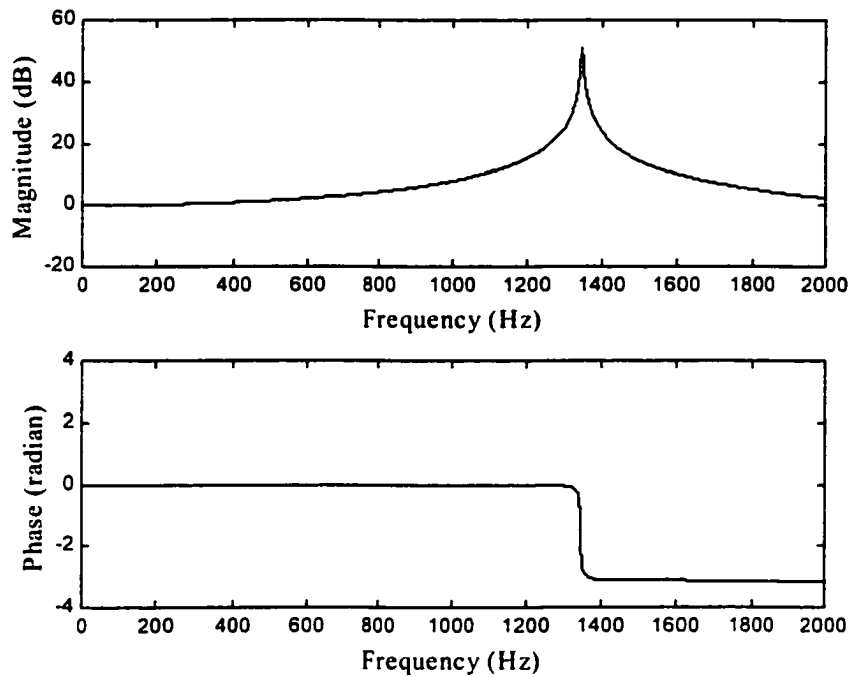
Figure 4. 4 Variation of $f2/F$ ratio with frequency ($m = 3.314 \times 10^{-3}$ kg, $K_1 =$ 0.3569×10⁵ N/m, $K_2 = 0.3569 \times 10^5$ N/m, $l = 0.08$ m, $\rho_1 = 7800$ kg/m³, $A_1 = 2.0111 \times 10^{-6}$ m², $E_1 = 200G$ Pa, $\rho_2 = 2800$ kg/m³, $A_2 = 7.9173 \times 10^{-4}$ m², and $E_2 = 72$ GPa).

It is shown in Figure 4.4 that the load pulse applied by the hammer will propagate to the

transmission bar without significant dispersion if the applied load by the hammer is

bandlimited within H_2's 3-dB point,

$$f_b^{H_2} = 684.1 \text{ Hz}$$

The first resonant frequency of H_1 ($f_r^{H_1} = 1651.7$ Hz)—the first resonant frequency of the specimen/transmission bar system—is definitely higher than the first resonant frequency of H_2 ($f_r^{H_2} = 1344.4$ Hz)—the first resonant frequency of the incident bar/specimen/transmission bar system—because H_1 is a subsystem of H_2. The first resonant frequency of a system cannot be higher than that of its subsystem.

As a result, if the hammer load is bandlimited within $f_b^{H_2}$, the load will propagate through without significant dispersion and, therefore, the specimen is in a dynamic equilibrium state. In other words, the specimen is in a dynamic equilibrium state if the input load pulse by the hammer can propagate through the specimen into the transmission bar without dispersion, i.e., all of the frequency components of the input pulse can pass through with gain 1 and without phase distortion.

The decrease in the first resonant frequency of $H_1(f_r^{H_1})$ is due to the incident bar. A parametric study shows that the smaller the length, diameter, and mass density of the incident bar, the closer the first resonant frequency of $H_1(f_r^{H_1})$ to the first resonant frequency of $H_2(f_r^{H_2})$. The Young's modulus of the incident bar is not a significant factor since the out-of-plane stiffness of the thin ceramic specimen is much lower than the stiffness of the incident bar. The effects of the length, diameter, and mass density of the incident bar on the first resonant frequency of $H_1(f_r^{H_1})$ are shown in Figures (4.5)~(4.7), respectively. In these figures, the parameters of the whole system are the same as before except for the one being examined.
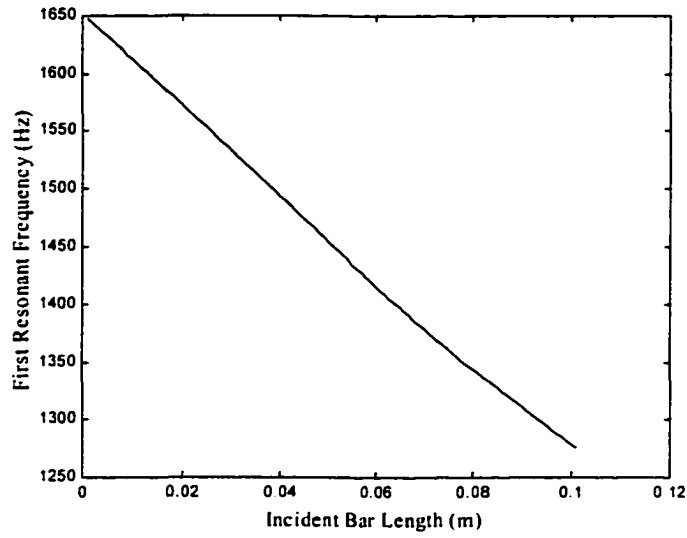
Figure 4. 5 Variation of the first resonant frequency with the length of incident bar (m = 3.314×10^{-3} kg, K_1 = 0.3569×10^5 N/m, K_2 = 0.3569×10^5 N/m, ρ_1 = 7800 kg/m^3, A_1 = 2.0111×10^{-6} m^2, E_1 = 200 GPa, ρ_2 = 2800 kg/m^3, A_2 = 7.9173×10^{-4} m^2, and E_2 = 72 GPa).
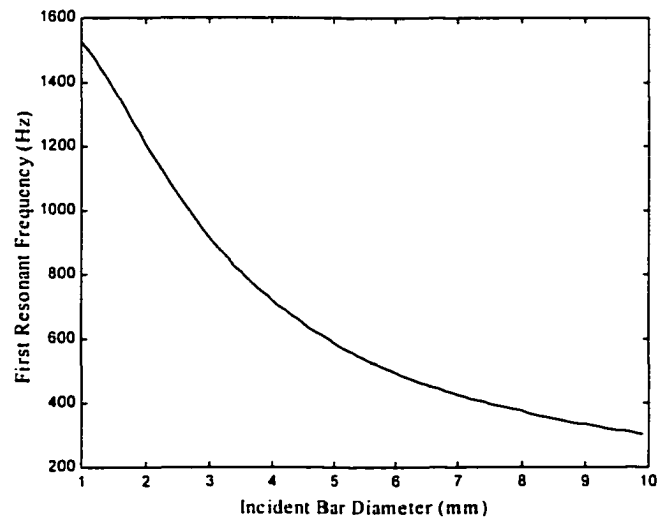
Figure 4. 6 Variation of the first resonant frequency with the diameter of incident bar (m = 3.314×10^{-3} kg, K_1 = 0.3569×10^5 N/m, K_2 = 0.3569×10^5 N/m, l = 0.08 m, ρ_1 = 7800 kg/m^3, A_1 = 2.0111×10^{-6} m^2, E_1 = 200 GPa, ρ_2 = 2800 kg/m^3, A_2 = 7.9173×10^{-4} m^2, and E_2 = 72 GPa).
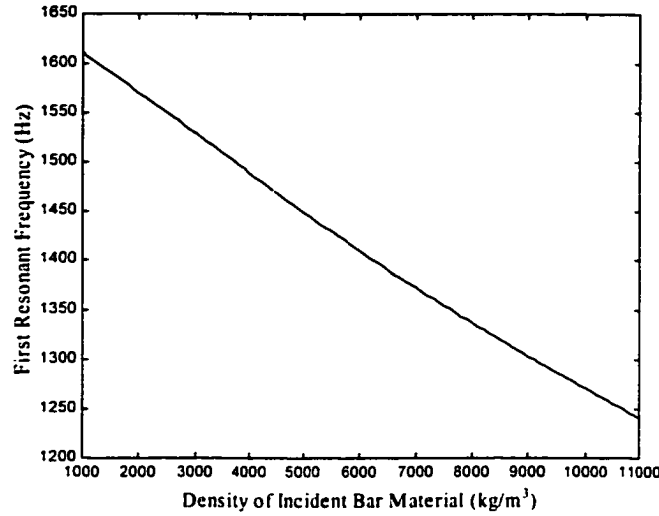
Figure 4. 7 Variation of the first resonant frequency with the density of incident bar $(m = 3.314\times10^{-3}$ **kg,** $K_1 = 0.3569\times10^5$ **N/m,** $K_2 = 0.3569\times10^5$ **N/m,** $l = 0.08$ **m,** $\rho_1 = 7800$ **kg/m^3,** $A_1 = 2.0111\times10^{-6}$ **m^2,** $E_1 = 200$ **GPa,** $\rho_2 = 2800$ **kg/m^3,** $A_2 = 7.9173\times10^{-4}$ **m^2, and** $E_2 = 72$ **GPa).**

The upper limit of the first resonant frequency of $H_2(f_r^{H2})$, which is the first resonant frequency of $H_1(f_r^{H1})$, is determined by the mass and stiffness of the specimen provided all of the parameters of the transmission bar are given. Fortunately, ceramics usually possess high stiffness, which allows a high loading rate while maintaining dynamic equilibrium. Therefore, reducing the mass of the specimen will raise the first resonant frequency of $H_2(f_r^{H2})$. On the other hand, the lower limit in the loading rate is set by the length of the transmission bar. The rise time of the loading pulse must be increased if the loading rate decreases. When the length of the transmission bar is finite, the forward-moving wave and the backward-moving wave reflected from the free end will overlap if the rise time of the loading pulse is long enough. The criterion for the upper limit of the rise time is as follows:

$$T_{loading} \leq \frac{2L_2^r}{c_0^T}$$ (4.23)

where $T_{loading}$ is the rise time of the loading pulse, L_2^r is the length of the transmission bar

section between the quartz force transducer and the free end, and c_0^T is the bar wave

velocity of the transmission bar.

In summary, the design of a valid dynamic biaxial bending experiment involves

the proper selection of a set of experimental parameters for a given specimen. When a

specific thin ceramic substrate needs to be tested for dynamic strength, the specimen out-

of-plane stiffness K is measured by the quasi-static piston-on-3-ball experiment first.

Then, the highest possible frequency component of the loading pulse is determined by

Equation (4.21). The aluminum alloy of the transmission bar material is a requirement for

the quartz-crystal-embedded split Hopkinson pressure bar technique because the

mechanical impedance of an aluminum alloy is approximately equal to that of the quartz

crystal. The diameter of the transmission bar is 32 mm, according to the diameter of the

specimen suggested by the standard of ASTM F 394-78. A proper hammer tip then can

be designed according to the desired loading rate, where the loading pulse must only

comprise frequency components with a frequency much lower than the first resonant

frequency of $H_1(f_r^{H_1})$. At this stage, the hammer impulse spectrum is analyzed to create

the relation between the loading rate and the highest frequency components in the loading

pulse. An incident bar is then designed using Equation (4.22). A proper incident bar

design facilitates judging of the specimen equilibrium by comparing the hammer load

signal and the transmission force signal. The specimen is in an equilibrium state if the hammer load propagates without dispersion. Finally, the length of the transmission bar is determined by Equation (4.23). The length of the transmission bar before the embedded quartz should be greater than 20 diameters of the transmission bar (Kennedy and Jonse, 1969).

The dynamic piston-on-3-ball experimental setup designed for this research purpose is shown in Figure 4.8. Figure 4.9 shows the test section of this experimental setup as well as the instrumented hammer. There is also a set of laser device shown in these pictures, which is used for the purpose of specimen deflection measurements.
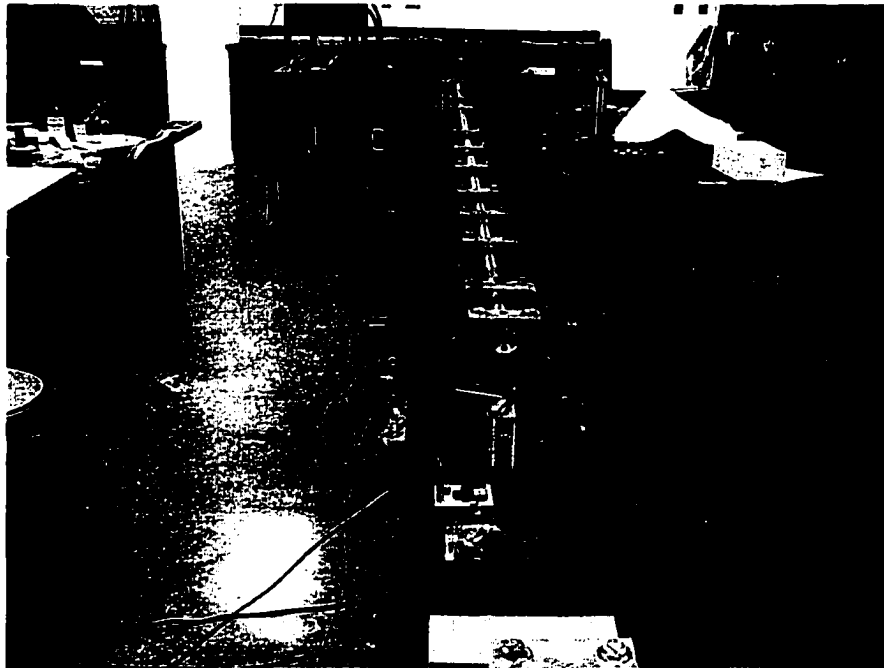
Figure 4. 8 Overall view of the dynamic piston-on-3-ball experimental setup

Figure 4. 9 Test section with the instrumented hammer and a set of laser device for specimen deflection measurements.

4.1.3 Experiments

Experiments on 8YSZ substrates and its doped versions are conducted using the dynamic piston-on-3-ball technique.

4.1.3.1 Data processing

Calibrations of measurement instruments are important for obtaining accurate data from experiments. The instrumented hammer has been well calibrated by the manufacturer, PCB Piezotronics Inc., with linearity error < 1.0% on the calibration certificate. However, the quartz crystal disk embedded in the transmission bar for measuring transmitted forces is assembled in the lab. The vender, Valpey-Fisher,

provided only a nominal sensitivity. Therefore, it is necessary to calibrate this transducer with its accessory, a charge amplifier.

Many methods can be employed to calibrate the quartz crystal disk embedded in the transmission bar. In this research, the well-calibrated hammer is used as a standard transducer to calibrate the quartz crystal disk. The calibrating procedure is only hitting the end of the transmission bar without the test section installed on. Signals from the hammer and the quartz crystal disk are sampled simultaneously. In this case, the force generated by the hammer must transmit into the transmission bar without significant dispersion. Since the sensitivity of the instrumented hammer is known, the sensitivity of the quartz crystal disk can be obtained by comparing these two force signals.

Another problem must be solved before calculating the final strength of the specimen is the 60-Hz electrical noise. It is difficult to apply a physical shield on the 4-meter long transmission bar (Figure 4.8) to avoid the effect of static electricity. Therefore, digital signal processing is a practical method to filter the 60-Hz electrical noise, which always exists in the force signals recorded from the quartz crystal disk embedded in the transmission bar, as shown in Figure 4.10. The amplitude of the 60-Hz electrical noise is large enough to affect the accurate evaluation of the peak load if not filtered.
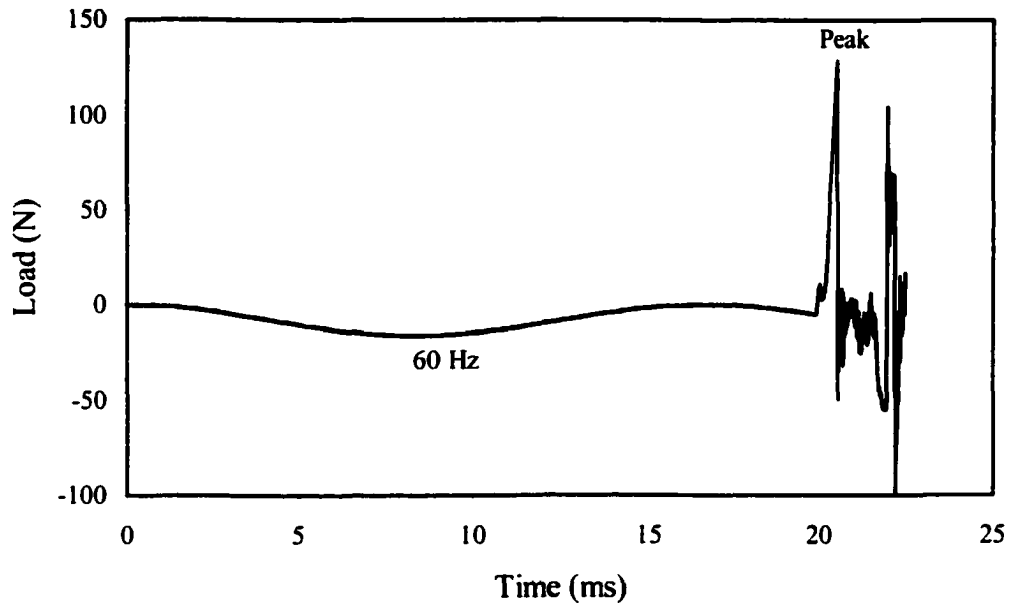
Figure 4. 10 Typical recorded force signal from the transmission bar.

Many digital filter design method can be used to design a band-resist filter to exterminate the 60-Hz component in this signal. However, even a linear phase finite impulse response (FIR) digital filters will inevitably change the wave shape of this signal since a digital filter filters 60-Hz electricity noise as well as the 60-Hz component of the loading signal. Since the signal needs no real-time processing, a relative simple processing method can be applied. The recorded force signal from the quartz crystal disk embedded in the transmission bar can be expressed as linear combination of a 60-Hz sinusoidal wave and a pulse wave.

$$S_{Quartz}(t) = a\cos(120\pi t + \varphi) + S_T(t)$$

where the first term on the right hand side is the 60-Hz sinusoidal wave with amplitude a

and phase delay φ, and the second term is the desired pulse wave. We can just over-

sample the quartz crystal disk signal with a large pre-trigger scans as shown in Figure

4.10. The front part of pure 60-Hz electricity noise then can be used to identify the

amplitude a and phase delay φ of the sinusoidal wave by employing a non-linear least

squares data fitting technique such as the function *nlinfit* provided by MATLAB 5.1

statistics toolbox. Once the 60-Hz sinusoidal wave is determined, the desired pulse wave

can be obtained by simply subtracting the 60-Hz sinusoidal wave from the quartz crystal

disk signal.

$$S_T(t) = S_{Quartz}(t) - a\cos(120\pi t + \varphi)$$

Here, it has been assumed that the 60-Hz electricity noise is stable within a short period

of time (~25 ms).

Typical force traces involving a 32-mm diameter, 0.72-mm thick 8YSZ ceramic

specimen after removing the 60-Hz electricity noise are presented in Fig. 4.11. Figure

4.11 shows that the specimen was in the dynamic force equilibrium state, since the

loading rate in hammer (3.3958×10^5 N/s) was almost the same as in the quartz

(3.3974×10^5 N/s).
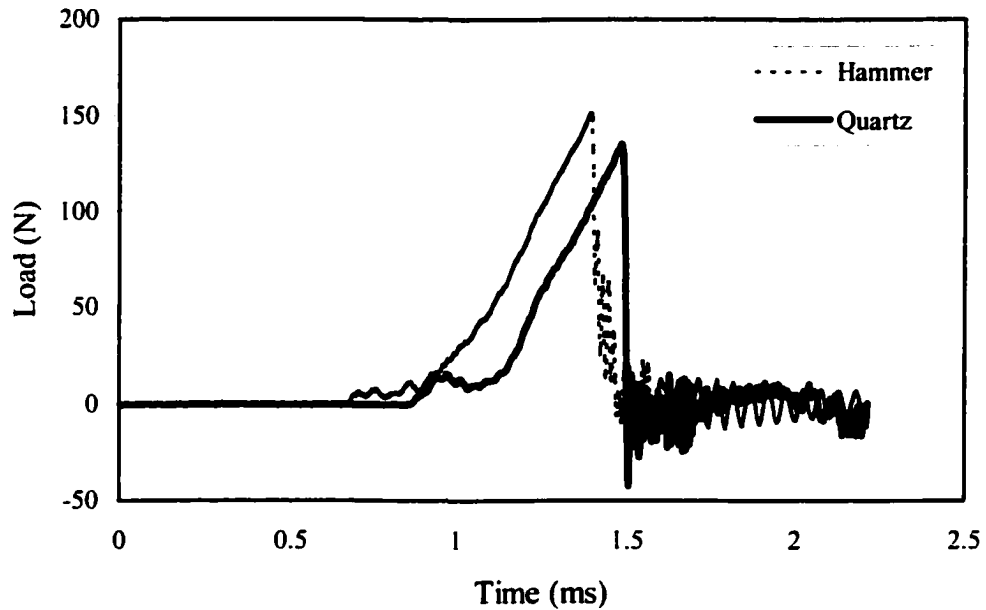
Figure 4. 11 Typical force traces after filtering the 60 Hz noises.

The transmitted force signal represents the actual load applied on the specimen provided the length of the transmission bar before the embedded quartz is larger than 20 diameters (Kennedy and Jonse, 1969) and the length after the quartz is enough to avoid overlapping of the reflected wave on the forward-moving wave. The force peak from the hammer is always higher than the force peak from the quartz signal because the specimen failure signal needs time to propagate through the incident bar back to the hammer. Therefore, the biaxial flexural strength of the specimen should be evaluated using the signal recorded by the quartz force transducer in the transmission bar.

4.1.3.2 Experimental results

Dynamic piston-on-3-ball experiments were performed on all the available specimens with chemical compositions listed in Table 1.2.

The strength data were evaluated by the peak load from the quartz force transducer in the transmission bar using the equation for the stress at the center of the tensile surface, Equation (2.1). The Poisson's ratios for these material compositions are chosen to be 0.315 as suggested by Selçuk and Atkinson (2000), since Poisson's ratio for YSZ ceramics is reported in literatures to be 0.30~0.32 and is relative insensitive to both composition and temperature (Kandil, Greiner, and Smith, 1984; Hendriksen and Jørgensen, 1996). The final experimental results, dynamic strengths, are listed in Table 4.1 with corresponding constant stress rate.

It is hard to obtain an overall picture of the dynamic strengths through the limited number of data listed in Table 4.1 if the scatter characteristic of the strength of ceramics is taken into consideration. An analytical model is needed therefore to describe the dynamic strength behavior under high stress-rate loading. The data in Table 4.1 can then be used to estimate parameters associated with such model. In next section, a new dynamic strength model under constant stress-rate loading is developed with parameters identified from these data listed in Table 4.1 using a nonlinear least squares method.

Table 4. 1
Dynamic biaxial flexural strength (MPa) / stress-rate (GPa/s)

8YSZ	1A	2A	3A	1Y	2Y	3Y
534.3/495.5	372.6/828.7	315.1/692.2	466.2/678.4	380.9/756.2	539.7/1308.1	424.4/1238.9
518.1/1446.9	364.1/831.8	320.1/482.2	584.0/908.2	186.9/429.5	369.2/578.4	447.6/1010.6
360.9/404.2	501.5/524.5	526.7/930.9	519.9/1016.9	497.2/1140.2	481.6/1312.1	447.5/404.8
531.3/500.4	425.8/722.0	550.1/470.3	516.7/1088.0	353.0/1424.2	471.9/1238.2	339.9/435.9
217.5/494.8	398.9/358.3	457.1/738.9	553.6/490.2	296.1/532.9	492.0/933.4	490.3/578.3
	374.3/402.6	474.5/1332.6	536.4/1450.3	473.2/512.3	440.1/829.8	570.5/1382.6
	719.3/1043.5	373.0/957.7	378.8/405.6	272.4/1024.6	456.8/1092.9	537.9/684.5
	592.3/836.8	319.8/638.4	548.5/510.2		489.1/813.8	407.1/792.5
	459.0/1207.0	252.3/321.2	238.5/500.5		393.4/1016.3	532.9/843.7
	529.4/931.6	249.6/974.5	471.6/980.7		443.2/515.8	378.3/365.5
	516.4/1068.1					
	376.8/595.0					
	581.8/678.9					
	503.7/1350.2					
	430.2/1093.6					
	367.3/836.3					
	465.1/1059.4					
	369.2/659.1					

4.2 Dynamic strength

The dynamic piston-on-3-ball experimental technique can be used to investigate the biaxial flexural strength of ceramic materials under a constant stress-rate loading condition. However, it is not economic and practical to obtain a relationship between biaxial flexural strength and stress-rate for a ceramic material by conducting a large number of experiments at each loading rate. The requirement for a large number of experiments at each loading rate is due to the scatter behavior of strengths of ceramic materials. Therefore, analytical modeling of strength at high loading rate is important for using experimental data to explain dynamic strength behavior of ceramic materials.

4.2.1 Introduction

The behavior of brittle materials such as ceramics under high-speed loading has been the subject of many studies during the past. Many experiments revealed that rapidly loaded structures could bear stresses that considerably exceeded the critical levels under static loading conditions (Grady, 1998; Bourne et al., 1998; Clifton, 2000). The most recent review of the field of dynamic failure mechanics is that of Rosakis and Ravichandran (2000). The development of new experimental techniques for dynamic tests and improvements in existing measuring devices made it possible to study the process of fracture in brittle materials under high-speed loading (Morozov and Petrov, 2000). Now, precise dynamic constitutive models can be developed to accurately

describe the mechanical responses and failure behaviors of brittle materials under high-speed loading.

Most modeling efforts on dynamic failure behaviors of brittle materials have been based on fracture mechanics and/or damage mechanics. Fracture mechanics is well enough developed to describe the crack propagation and dynamic fracture of brittle materials. However, it can only be applied when an initial crack is well defined or assumed, with its shape, size, location, and orientation determined. The material bulk is considered to be a continuum other than a crack. On the other hand, damage mechanics describes the effects of micro-cracking on the mechanical properties (such as elastic stiffness degradation, induced anisotropy, and anelastic strains) of the brittle material as micro-cracking develops. Distributed crack models are inevitably included in the dynamic material models based on damage mechanics (Mazars and Pijaudier-Cabot, 1996).

Freund (1990) formulated a dynamic material model to describe the time-dependent strength of brittle materials under high strain-rate loading by applying a Weibull's crack density model and an effective elastic stiffness model proposed by Delameter et al. (1975). He stated that the macroscopic stress in a brittle specimen subjected to high strain-rate loading can continue to increase as the macroscopic deformation proceeds during the incubation time, which is the delay time between the initial crack propagation and the final failure of the structure. During this incubation period, the critical level of stress needed to produce crack growth can be reached at many other defects in the specimen. Crack growth can thus be initiated at many flaws if the

loading is applied rapidly. As the cracks in the specimen continue to grow, the effective

elastic stiffness of the cracked specimen continues to degrade. Finally, the stress in the

specimen fails to increase further. The stress at this moment was defined by Freund as the

impact strength at a certain constant strain-rate. Later on, many researchers modified

Freund's constant strain-rate model by applying different effective elastic stiffness

models. For example, Chen and Ravichadran (1992) modified this model using an

effective elastic stiffness model developed by Kemeny and Cook (1986). Chen (1995)

modified Freund's model using another effective elastic stiffness model given by

Budiansky and O'Connell (1976).

Most existing constitutive models for high-speed loading are constant strain-rate

models. In most cases, the constant strain-rate models were developed based on a

uniaxial loading condition, Ravichandran and Subhash (1994b) developed a constitutive

model applicable to brittle materials such as ceramics subjected to biaxial compressive

loading and Rajendran (1994) developed a constitutive model for ceramics under

multiaxial loading.

In order to describe the dynamic strength behavior of brittle materials accurately,

it is necessary to develop high stress-rate models, also. The importance of such models is

conditioned by two circumstances. First, besides constant strain-rate loading, material

tests under constant stress-rate loading are also rather routine and equally valuable to

determine dynamic material behavior. For example, a split Hopkinson pressure bar

(SHPB) can generate either a uniaxial constant strain-rate (Lambert and Ross, 2000) or

constant stress-rate loading condition in a specimen if the incident pulse is properly

controlled (Gray, 2000; Frew, Forrestal, and Chen, 2001; Frew, Forrestal, and Chen, 2002). Many other dynamic experimental techniques, such as the drop ball test (DBT) (Bouzid et al, 2001) and the dynamic piston-on-3-ball test developed in this dissertation, generate a constant stress-rate loading condition in the specimen. Second, in many applied problems, the substitution of the real stress velocity by some averaged value for the whole process does not lead to a significant error (Morozov and Petrov, 2000).

Denoual et al. (1997) developed a model for fragmentation of brittle materials under constant stress-rate loading using a probabilistic approach. They used a high-speed camera in their experiments and observed that the velocities of crack tips were less than the velocity of the crack damage wave front (Riou, Denoual, and Cottenot, 1998). A crack nucleates when the local tensile stress reaches a critical value and stops when other defects nucleate in front of it and relax the local tensile stresses. Based on this observation, a model for constant stress-rate loading was formulated through a probabilistic approach, which predicated that the dynamic strength of brittle materials under constant stress-rate is proportional to $(\dot{\sigma})^{n/(n+m)}$, where $\dot{\sigma}$ is the stress-rate applied to the brittle material specimen, m is the Weibull parameter of this material under static loading, and n is the space dimension (i.e., 3 for volume, 2 for surface, and 1 for length). This model was later successfully used in a numerical simulation of the damage process in a brittle material (Denoual and Hild, 2000).

Bouzid et al. (2001) proposed a damage model to describe the failure of a glass under constant stress-rate impact loading. They introduced a damage parameter to

describe the degree of damage to the specimen and observed three different damage stages in their experiments on a float glass. At low loading rates (< 20 GPa/s), cracks are initiated from one site of the specimen without any crack branching. In the middle loading rate range (about 1000 GPa/s), multiple fragmentations are caused by numerous crack bifurcations. In this range of loading rates, the crack propagation speed is not large enough to prevent new crack growths from being initiated in front of the propagating crack, causing this crack to stop propagating because of local stress relaxation. At high loading rates (about 3630 GPa/s), complete perforation by the impactor is reached without significant crack propagation in the glass bulk.

These various models are based on many ideal assumptions. The complicated details of propagation of each crack in the material bulk are avoided. This is necessary in order for a model to have a limited number of parameters and to be used in the practical processing of experimental data. There are also limitations associated with each model. For example, Denoual et al.'s model (Denoual, Barbier, and Hild, 1997) covers only part of loading-rate range, and the starting point of this range is unknown. Bouzid et al.'s model (Bouzid et al., 2001) shows that the degree of damage is a function of loading rate and applied stress, but provides no explicit relationship between loading rates and the dynamic strength of brittle materials. These drawbacks make it difficult to design proper experiments for these models to identify parameters associated with the dynamic strength of brittle materials. The dependence of dynamic failure strength on the loading rate needs to be systematically explored in order to better understand the strength-loading rate relationships. It is desired to formulate explicit relationships between dynamic strength

and stress loading-rate. In addition, fracture mechanics points out that the strength of a brittle material is dependent on the loading modes and the loading rates, as well as the initial crack sizes and orientations (Lawn, 1993). The dynamic strength of a brittle material should then be related to its strength under static loading conditions.

In the following sections, a new model is proposed to describe the dynamic strength of brittle materials under a constant stress-rate loading condition. Experimental results performed on thin sheets of 8YSZ and its doped versions with the dynamic piston-on-3-ball technique, Table 4.1, are used to estimate the parameters associated with this new model. This new model is found to give a good description to the experimental results.

4.2.2. Strength Model under Constant Stress-Rate Loading

Tuler and Butcher (1968) proposed a general failure criterion based on the concept of damage accumulation. The spall stress σ is dependent on the stress pulse duration in the form

$$\int_0^{t_s} \left[\sigma(t) - \sigma_0\right]^{\lambda} dt = \text{Constant} \tag{4.24}$$

where σ_0 is a threshold stress, t_s is the time to failure from $\sigma(t) = \sigma_0$, and λ is a material constant. This model indicates that a longer t_s corresponds to a lower spall stress, $\sigma_s = \sigma(t_s)$. They found a good correlation between the spall stress values estimated by

Equation (4.24) and those obtained experimentally for a spalling layer of aluminum specimens. Freund (1990) recast Tuler and Butcher's model in the form

$$\int_0^{t_s} \left[\frac{\sigma(t)}{\sigma_w} - 1 \right]^{\beta} dt = C \tag{4.25}$$

where $\sigma(t)$ is a representative stress (such as the remote tensile stress in the case of uniaxial loading and/or the central stress on the tensile surface in the case of biaxial loading, e.g., piston-on-3-ball loading), σ_w is the stress threshold for the beginning of damage accumulation, t_s is the time required for the stress to start from σ_w and to reach its maximum level, and β and C are experimentally determined material constants. Freund (1990) proved that this model is consistent with his constant strain-rate loading model.

The new model is based on Tuler and Butcher's (1968) general failure criterion, Equation (4.25), which represents a relationship between dynamic strength and constant stress-rate with an emphasis on the stress-rate effects. Two idealized assumptions have been introduced in the development of this model. First, the threshold stress, σ_w, is approximately the same as the strength of the same material under static loading. The dynamic strength of a brittle material always increases from its static strength with increasing strain rate as commonly observed from experiments (Grady, 1998; Bourne, Millett, Rosenberg, and Murry, 1998; Clifton, 2000). Second, the dynamic strength depends only on the loading history after the stress load exceeds the static strength. This means the loading mode has no effect on the dynamic strength if the stress load is less than the static strength. This is consistent with the "weakest link" concept in fracture

mechanics (Jayatilaka, 1979), which indicates that the critical crack propagation determines the strength of a brittle material. In other words, the crack size distribution in the material bulk does not change if the applied load is under its static strength. Therefore, as pointed out previously, the initial time can be set at the point where stress load passes the static strength. The loading stress history after passing σ_w can then be expressed as

$$\sigma(t) = (\dot{\sigma}t + \sigma_w)H(t) \qquad (4.26)$$

where $H(t)$ is the Heaviside function and $\dot{\sigma}$ is the applied constant stress-rate.

Substituting (4.26) into (4.25), we obtain

$$\frac{\dot{\sigma}^\beta}{\sigma_w^\beta} \frac{t_s^{\beta+1}}{\beta+1} = C \qquad (4.27)$$

The stress, $\sigma(t)$, increases linearly from σ_w at $t = 0$ to the dynamic strength, σ_s, at $t = t_s$ in this constant stress-rate strength model, i.e.,

$$\sigma_s = \dot{\sigma}t_s + \sigma_w \qquad (4.28)$$

By eliminating t_s in Equations (4.27) and (4.28), we obtain

$$\sigma_s = \sigma_w \left[1 + \left(\frac{\dot{\sigma}}{\dot{\sigma}_r} \right)^{\frac{1}{1+\beta}} \right] \qquad (4.29)$$

where the reference stress-rate, $\dot{\sigma}_r$, is defined as

$$\dot{\sigma}_r = \frac{\sigma_w}{(1+\beta)C}$$

4.2.3.Modeling of Dynamic Experimental results

Dynamic piston-on-3-ball experiments were performed on all the available specimens listed in Table 1.2 along with their chemical compositions. The dynamic test data are listed in Table 4.1. It is very difficult to obtain a group of experimental results with identical loading rates since the loading rate can only be controlled within a certain range. Therefore, a regular statistical method to process data with the same loading rates is infeasible. These data are thus fitted to Equation (4.29) using an overall nonlinear least squares method. The threshold stress for each material composition is chosen as the corresponding mean strength at the quasi-static state, see Table 3.3. The final resulting parameters are listed in Table 4.2. Figures 4.12~4.18 give the fitting curves for a stress-rate range from 0 to 1600 GPa/s. Although the number of experimental results of some compositions is very small, for example, only 5 results for the pure 8YSZ composition are available, these fitting curves are close to each other. This indicates that the variations of the dynamic strengths of these compositions are not significant, which is consistent with the static strength results on these compositions.

Table 4. 2
Dynamic strength parameters

Ceramic Alias	Reference stress-rate $\dot{\sigma}_r$	Parameter β
8YSZ	2574	0.490
1A	2589	0.414
2A	2867	0.429
3A	2530	0.459
1Y	3398	0.434
2Y	3121	0.454
3Y	3709	0.470
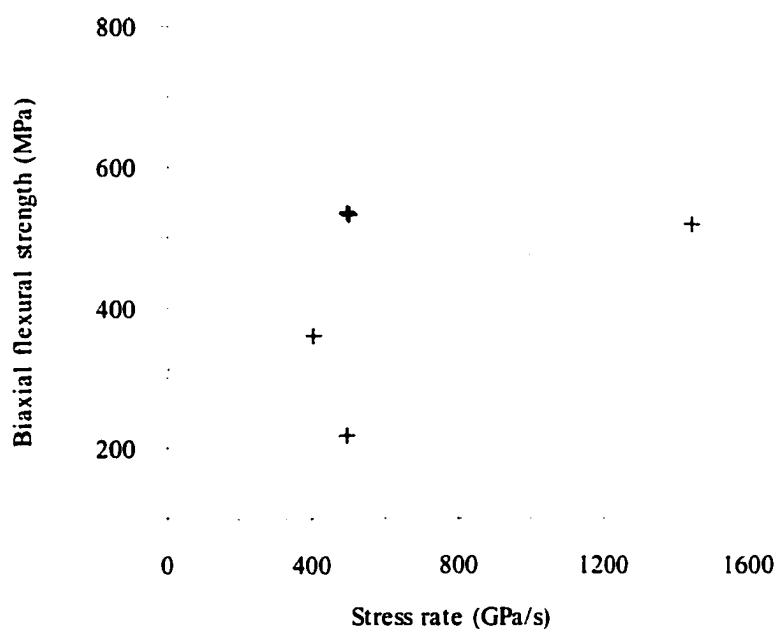
Figure 4. 12 Variation of dynamic biaxial flexural strength of 8YSZ as a function of stress-rate.
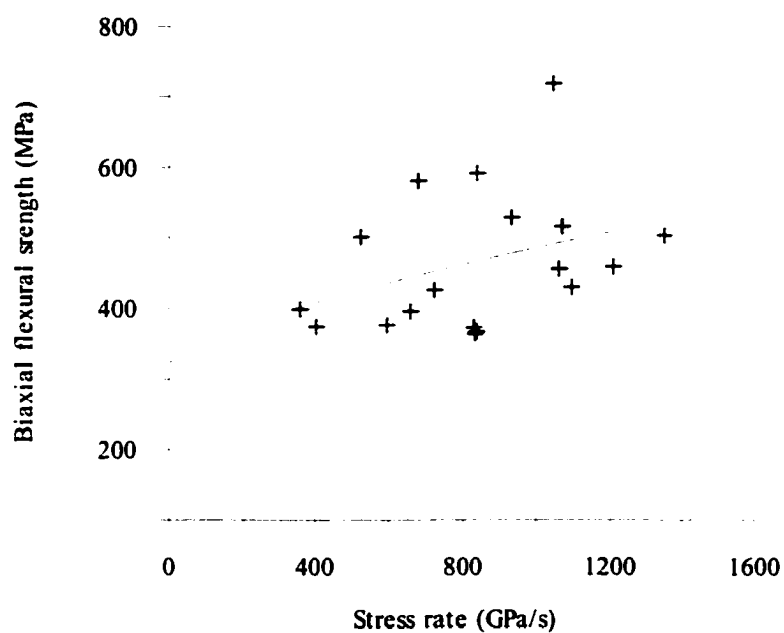
Figure 4. 13 Variation of dynamic biaxial flexural strength of 1A as a function of stress-rate.
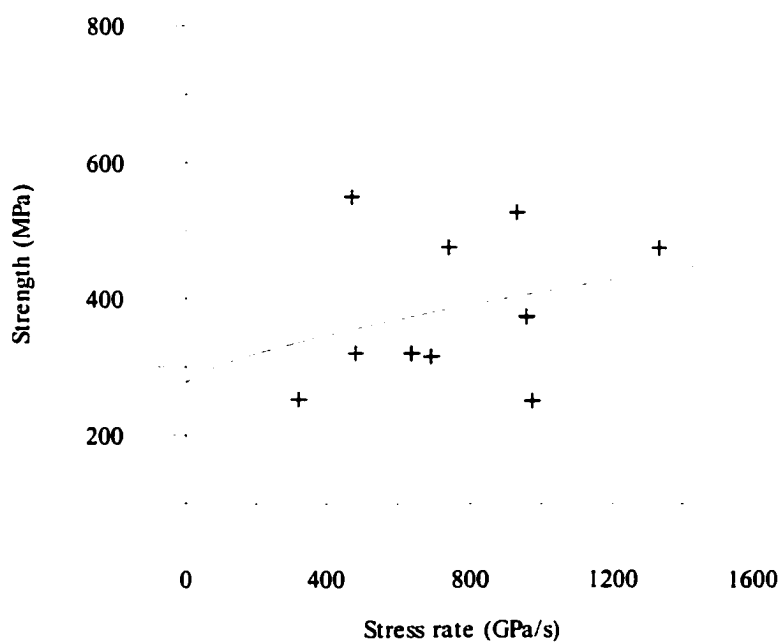
Figure 4. 14 Variation of dynamic biaxial flexural strength of 2A as a function of stress-rate.
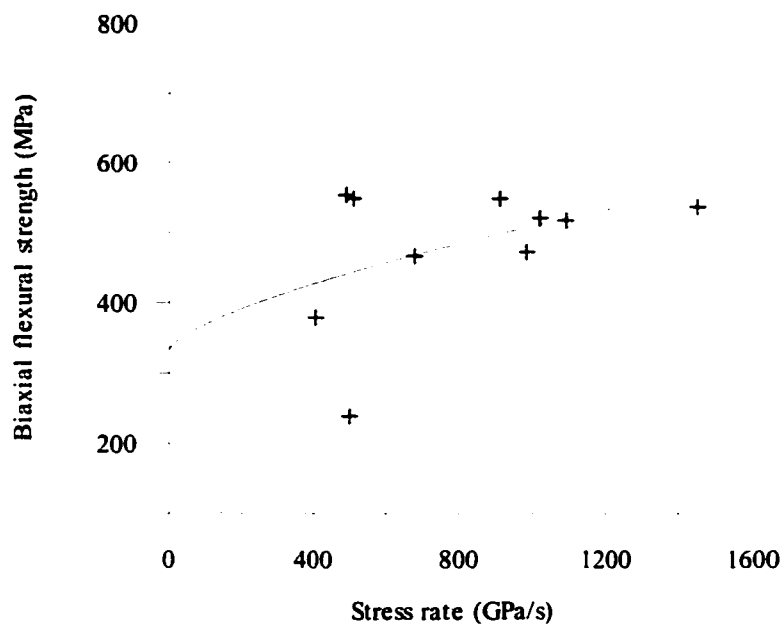
Figure 4. 15 Variation of dynamic biaxial flexural strength of 3A as a function of stress-rate.
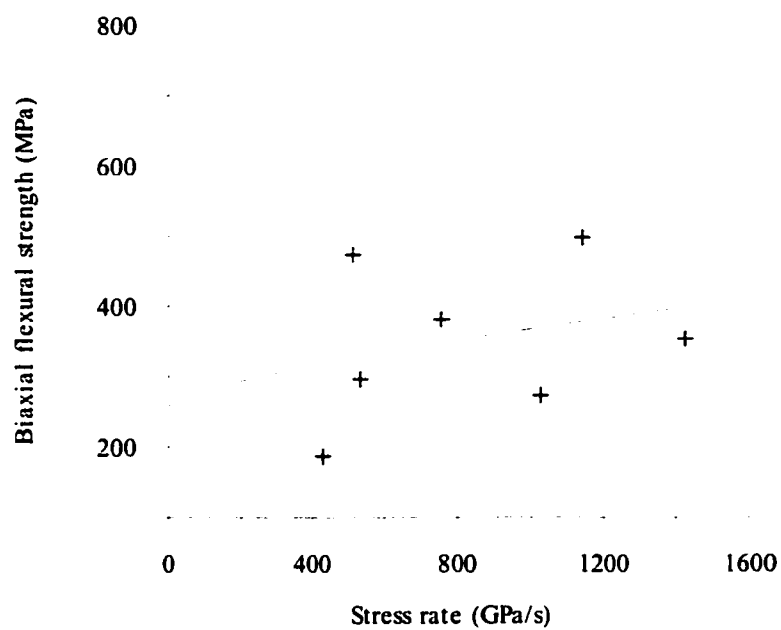
Figure 4. 16 Variation of dynamic biaxial flexural strength of 1Y as a function of stress-rate.
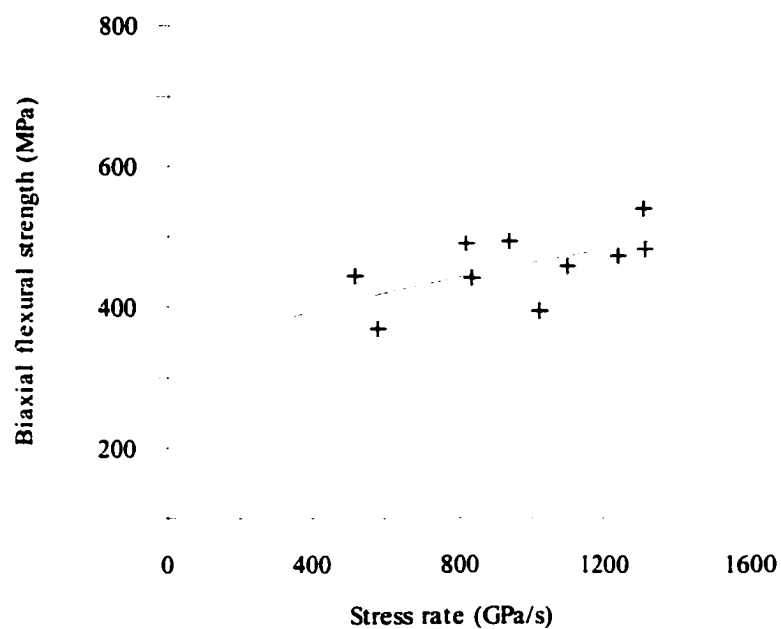
Figure 4. 17 Variation of dynamic biaxial flexural strength of 2Y as a function of stress-rate.
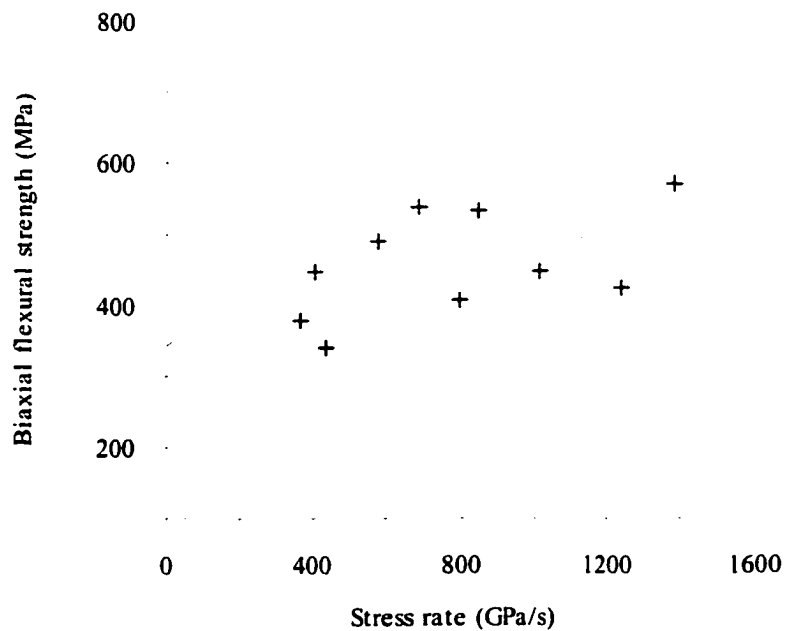
Figure 4. 18 Variation of dynamic biaxial flexural strength of 3Y as a function of stress-rate.

4.2.4. Discussions

The model for dynamic strength at high stress-rate loading as expressed by Equation (4.29) recovers the strength at the quasi-static state as the loading rate approaches zero. In other words, this model covers the stress-rate range from zero, which is not the case for other models in the literature. Denoual's high stress-rate fracture strength model (Denoual and Hild, 2000) and Morozov's high stress-rate yield strength model (Morozov and Petrov, 2000) cover only a stress-rate range that starts at some finite value. This finite value has to be experimentally estimated for each material, causing difficulties in the application of these models in practice.

Although Equation (4.29) enforces the quasi-static strength to be recovered, some precautions concerning the use of this equation are appropriate. First, in spite of the fact that Freund's model for constant high strain-rate loading (Freund, 1990) is consistent with Tuler and Butcher's criterion (Tuler and Butcher, 1968) and that the modeling procedure involves only straight mathematical manipulation, it is still difficult to provide rigorous theoretical or experimental proof to verify the validity of this model. Moreover, Equation (4.29) holds for specimens with the same threshold stress (static strength), but this cannot be guaranteed for individual specimens due to the randomly distributed strength of ceramic specimens. The quasi-static strength typically possesses a Weibull distribution (see Equation 3.20) (Jayatilaka, 1979) with a mean strength

$$\bar{\sigma}_b = \frac{\sigma_0}{V_e^{1/m}} \Gamma\left(1 + \frac{1}{m}\right) \qquad (4.30)$$

where Γ is the Euler function of the second kind.

As described by Equation (4.29), the dynamic strength under constant stress-rate loading is a linear function of the quasi-static strength. Therefore, the dynamic mean strength is

$$\left(\overline{\sigma}_s\right)^{(D)} = \frac{\sigma_{w}}{V_e^{1/m}}\Gamma\left(1+\frac{1}{m}\right)\left[1+\left(\frac{\dot{\sigma}}{\dot{\sigma}_r}\right)^{1/(1+\beta)}\right] \tag{4.31}$$

where the superscript, (D), indicates a dynamic loading condition with a constant stress rate.

Theoretically, we need at least 30 experiments (ASTM C 1161-94, 1995) for each stress-rate to estimate the statistical distribution of strength results without a material model such as Equation (4.29). This is neither economical nor practical since a huge amount of data must be acquired by experiments. With the help of the dynamic strength model, Equation (4.29), it is possible to fit all experimental data with different stress-rates together. Therefore, this method helps to reduce the minimum requirement for the number of experiments. Table 4.2 shows that about 10 experiments are possible to obtain relatively stable fitting results. However, the small number of specimens in this study was due to the limited number of specimens available, not to the experimental design.

4.3 Summary

An experimental technique for determining the biaxial flexural strength of thin ceramic substrates at high loading rates has been developed and verified by experiments. The loading configuration is the same as the quasi-static piston-in-3-ball experimental technique, making the high loading rate results directly comparable to the standard quasi-static results. The upper and lower limits of the loading-rate range for a valid experiment with a specific specimen were analyzed.

A new model for dynamic strength under constant high stress-rate loading for brittle materials was developed based on the concept of cumulative damage. The parameters in this model were experimentally identified using an overall least squares curve-fitting technique with all of the data at different loading stress-rates.

Ceramic material 8YSZ and six of its doped compositions with Al_2O_3 and 3YSZ were tested with the dynamic piston-on-3-ball experimental technique. The experimental results show that the new dynamic strength model for brittle materials describes both the quasi-static strength and the dynamic strength behavior appropriately.

CHAPTER 5

BIAXIAL FLEXURAL STRENGTH AT ELEVATED

TEMPERATURES UNDER QUASI-STATIC PISTON-ON-3-BALL

LOADING CONDITION

The working temperature of electrolytes is 800~1000°C. Many researches revealed that ceramic materials show different mechanical behaviors at elevated temperatures from that at ambient temperature (24°C). In this chapter, the quasi-static piston-on-3-ball experimental technique at ambient temperature is adapted to an environment with controlled temperatures. Therefore, piston-on-3-ball biaxial flexural strength of ceramic substrates at elevated temperatures can be experimentally investigated. This is important to the design of a reliable electrolyte.

5.1 Introduction

The mechanical properties of ceramic materials at elevated temperatures are different from that at ambient temperature (24°C). Rice (1997) provided a comprehensive review in this field. For zirconia material, most research efforts focused on the variations of its Young's modulus, tensile strength, and fracture mode with temperatures.

While Young's modulus of ceramic materials is one of physical properties, relationships between theoretical strengths in shear and tension have been created by Frenkel in 1926 and Orowan in 1949, respectively (Kelly and MacMillan, 1986). Although these relationships are approximate, they revealed that the strengths of ceramic materials are dependent on their Young's moduli. The variations of Young's moduli of 3YSZ and 8YSZ materials at ambient temperature with their porosities were studied by Selçuk and Atkinson (1997).

At elevated temperatures, Kandil, Greiner, and Smith (1984) found that cubic phase zirconia single crystals containing 11.1, 12.1 15.5 and 17.9 mol% yttria show a typical Young's modulus decrease about 1~2% per 100°C with increasing temperature to their limit of testing (700°). However, their results about 8.1 mol% yttria stabilized zirconia crystals did not follow the trend. For polycrystalline materials, Shimada et al. (1984) reported a continuous decrease of the Young's modulus of 3YSZ with increasing temperature till 700°C. Their curve of Young's modulus vs. temperature showed a higher decreasing rate before 350°C, which is similar to the Adams et al.'s results (Adams, Ruh, and Mazdiyasni, 1997). Adams et al. showed that the Young's modulus of cubic phase 6.5 mol% yttria stabilized zirconia was 222 GPa at 25°C. It decreased to about 180GPa at 400°C, and then kept relatively constant with increasing temperature up to 1350°C.

Adams et al.'s experiments (Adams, Ruh, and Mazdiyasni, 1997) also showed that the fast fracture four-point bending flexural strength of cubic phase 6.5 mol% yttria stabilized zirconia decreased to about 20% of its ambient temperature value at

750°~1000°C, then appeared to increase slightly as the temperature further increased to 1500°C. Similar trend was reported by Mori et al. (1994) about 8YSZ materials. They found that the temperature dependence of bending strength of 8YSZ showed a minimum value at 500°C. The strength at 1000°C was 250MPa, almost comparable to that at room temperature. They explained that the phenomenon of the high strength of 8YSZ at 1000°C might be due to the small contribution of plastic deformation.

The fracture mode of cubic phase 6.5 mol% yttria stabilized zirconia was transgranular at low temperatures (<~500°C), mixed mode at intermediate temperatures (~500°C-1000°C), and intergranular at high temperatures (>1000°C) (Adams, Ruh, and Mazdiyasni, 1997). The four-point flexural strength of the hot-pressed and sintered Zyttrite® yttria-stabilized zirconia showed a minimum value at about 760°C and 960°C, respectively. The facts that mechanical properties of ceramic materials at elevated temperatures behave so differently from that at ambient temperature and that the electrolytes work mainly at elevated temperatures show the necessity to investigate the strengths of 8YSZ ceramic substrates at elevated temperatures.

5.2 Piston-on-3-ball technique at elevated temperatures

The strength of brittle materials such as ceramics depends significantly on specimen size and loading conditions (Weibull, 1939; Richerson, 1992; Hoshide, Murano, and Kusaba, 1998). To avoid any possible ambiguity about the explanations of experimental data introduced by different specimen geometries and loading conditions, the ASTM standard quasi-static piston-on-3-ball experimental technique (ASTM F 394-78, 1995) is adapted to an experimental method at elevated temperatures, since there is still no standard experimental method for measuring biaxial flexural strength at elevated temperatures.

To obtain an elevated temperature test environment, a furnace is designed whose temperature is controlled by a WATLOW 982 temperature-controller with a type K thermocouple. The temperature rising procedures can then be programmed. The variation in temperature during test period can be controlled within $\pm 2^\circ C$. In order to maintain the same experimental conditions, except for the environmental temperature, the test sections of both the ambient and elevated temperature experimental facilities are identical—a standard piston-on-3-ball setup. The fixture for the elevated temperature experiments is made of SiC, which is inert and oxidation resistant at temperatures up to at least $1200^\circ C$. The configuration of the quasi-static piston-on-3-ball method at elevated temperatures is the same as the quasi-static piston-on-3-ball method at ambient temperature shown schematically in Figure 2.2 except that the test section is placed inside the furnace.

Flexural strength at elevated temperatures may be strongly dependent on loading rate, a consequence of creep, stress corrosion, or subcritical crack growth. Therefore, proper loading rates must be carefully chosen to minimize these effects because the purpose is to determine the load peak associated with fast fracture of the specimen at elevated temperatures. The experiments were performed using a hydraulically driven material testing system (MTS 810) with a piston moving speed of about 1.27 μm/sec for the 8YSZ ceramic substrates in this research, which is the same as in the ambient temperature tests.

Specimens were placed on the experimental fixture within a cold furnace. A gap between the piston end surface and the specimen surface was provided to avoid loading caused by thermal expansions during heating up. The piston was perpendicular to the top surface of the specimen by adjusting an alignment system manufactured by MTS Company. The furnace was then raised to the test temperature at a constant heating rate of 3°C per minute to avoid effects of thermal shock, as suggested in the standard three- or four-point test methods for flexural strength of advanced ceramics at elevated temperatures (ASTM C 1211-92, 1995). The test temperature was then held constant for at least 1 hour for the specimen and furnace to come to an equilibrium state. The remaining test procedure is the same as that at ambient temperature.

The effects of thermal expansion have been incorporated into Equation (2.1) by introducing a thermal expansion term into all the linear dimensions. The thermal expansion coefficients for 8YSZ and its doped versions listed in Table 1.2 were determined to be 10.5 μm/m-°C as provided by MarkeTech International Inc.. Numerical

experiments show that this typically will lead to a bias in the flexural strength on the order of 1 to 3%. However, the scatter, or Weibull modulus, will be unaffected if the distribution in thermal expansion is not taken into account, since all specimens experience the identical error.

5.3 Experimental results

Quasi-static piston-on-3-ball experiments at elevated temperatures were performed on all the available specimens with chemical compositions listed in Table 1.2. The strength data were evaluated by the peak load using the equation for the stress at the center of the tensile surface, Equation (2.1). The Poisson's ratios for these material compositions are chosen to be 0.315 as suggested by Selçuk and Atkinson (2000), since Poisson's ratio for YSZ ceramics is reported in literatures to be 0.30~0.32 and is relative insensitive to both composition and temperature (Kandil, Greiner, and Smith, 1984; Hendriksen and Jørgensen, 1996). The final experimental results are listed on Tables 5.1~5.7 with corresponding temperatures.

Table 5. 1
8YSZ biaxial flexural strength (MPa) data at elevated temperatures

No.	300°C	500°C	800°C	1000°C
1	247.9	230.2	289.0	281.2
2	159.1	185.1	190.0	254.9
3	293.6	222.9	287.3	237.7
4	276.1	233.0	212.0	
5	112.0	233.0	243.0	
6	192.0		224.4	
7			230.2	
8			220.5	
9			255.7	
10			226.7	
11			235.4	
Mean	213.4	220.8	237.6	257.9
std.	71.1	20.4	30.1	21.9

Table 5. 2
1A biaxial flexural strength (MPa) data at elevated temperatures

No.	300°C	500°C	800°C	1000°C
1		236.8	286.7	
2		203.0	245.2	
3		233.8	229.9	
4		216.1	235.9	
5		196.7	246.0	
Mean		217.1	248.8	
std.		18.2	22.2	

Table 5. 3
2A biaxial flexural strength (MPa) data at elevated temperatures

No.	300°C	500°C	800°C	1000°C
1	263.6	191.2	247.0	258.6
2	236.5	235.9	275.0	221.6
3	214.2	210.7	272.2	263.5
4	150.5	215.4	240.0	247.0
5	255.5	163.7	207.9	194.0
6		166.4	242.1	
7		180.3	290.1	
8		222.9	242.6	
9		213.5	289.3	
10		247.6	239.8	
Mean	224.1	204.8	254.6	236.9
std.	45.3	28.5	26.2	28.9

Table 5. 4
3A biaxial flexural strength (MPa) data at elevated temperatures

No.	300°C	500°C	800°C	1000°C
1		177.5	195.0	
2		264.3	196.9	
3		173.7	255.0	
4		151.8	267.6	
5		198.8	199.3	
Mean		193.2	222.7	
std.		43.1	35.5	

Table 5. 5
1Y biaxial flexural strength (MPa) data at elevated temperatures

No.	300°C	500°C	800°C	1000°C
1		154.4	223.9	
2		177.1	156.7	
3		162.8	207.1	
4		174.5	184.5	
5		135.5	144.7	
6			206.0	
7			138.2	
8			168.9	
9			132.1	
10			235.4	
Mean		160.9	179.8	
std.		16.9	37.1	

Table 5. 6
2Y biaxial flexural strength (MPa) data at elevated temperatures

No.	300°C	500°C	800°C	1000°C
1	183.3	159.5	182.2	195.4
2	209.9	186.6	212.0	213.0
3	195.2	184.4	173.1	190.2
4	217.4	171.7	192.6	189.7
5	233.9	156.6	207.1	232.2
6			188.8	
7			163.3	
8			221.3	
9			225.6	
10			229.0	
Mean	207.9	171.7	199.5	204.1
std.	19.6	13.8	22.9	18.4

Table 5. 7
3Y biaxial flexural strength (MPa) data at elevated temperatures

No.	300°C	500°C	800°C	1000°C
1		240.3	258.5	
2		204.6	194.6	
3		250.5	224.5	
4		264.0	270.7	
5		220.2	241.1	
Mean		235.9	237.9	
std.		23.7	29.9	

5.4 Discussions

Some Weibull moduli were obtained by fitting these data into the Weibull distribution function, Equation (3.20), using a method of maximum likelihood (Jayatilaka, 1979). The linearized Weibull plots for experimental data at 800°C are shown in Figures 5.1~5.7, and the associated Weibull parameters, as well as biaxial flexural strengths at 800°C, are listed in Table 5.8. The 95% confidence intervals of these Weibull parameters are larger than those at ambient temperature in Table 3.3 because of limited number of experimental data available at 800°C. Although the large 95% confidence intervals of these Weibull parameters show a high level uncertainty of the results, it can

still be observed that the Weibull modulus, m, of each material composition at 800°C is larger than that at ambient temperature, while the representative volume, V_e, remains almost the same. The small increase in the Weibull modulus is probably due to the thermal expansion effects on the cracks in the material. As proved in chapter 3, the crack size distribution determines the Weibull parameters. Therefore, Weibull modulus increases with increasing temperature, which increases the sizes of cracks by thermal expansion.
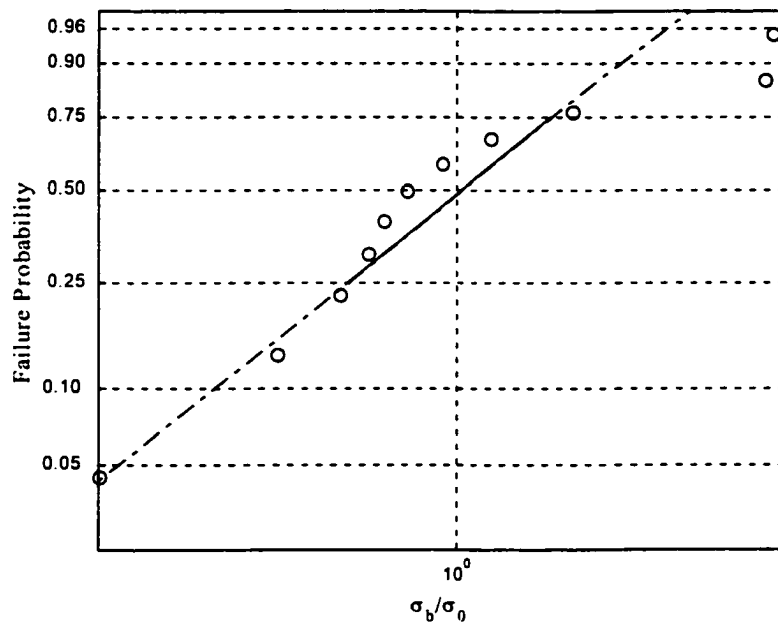
Figure 5. 1 Weibull probability plot of the biaxial flexural strength of 8YSZ from the piston-on-3-ball experiments at 800°C.
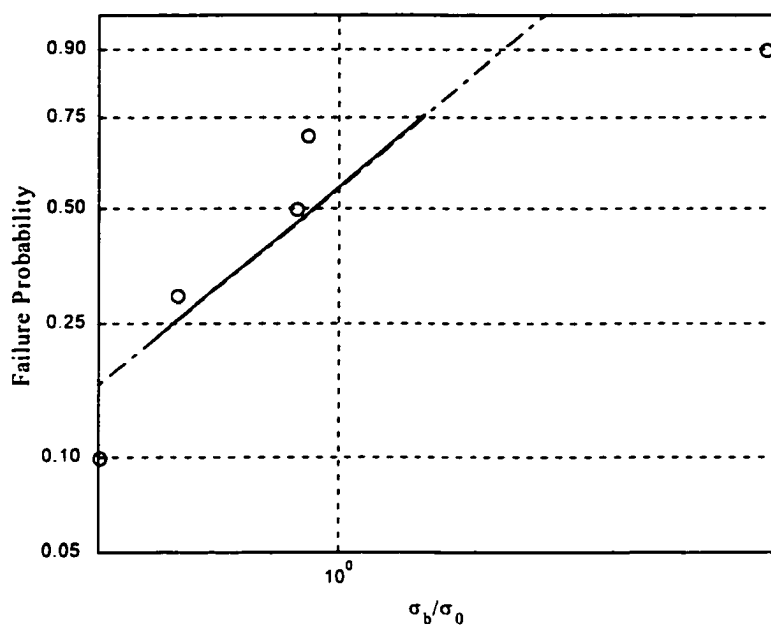
Figure 5. 2 Weibull probability plot of the biaxial flexural strength of 1A from the piston-on-3-ball experiments at 800°C.
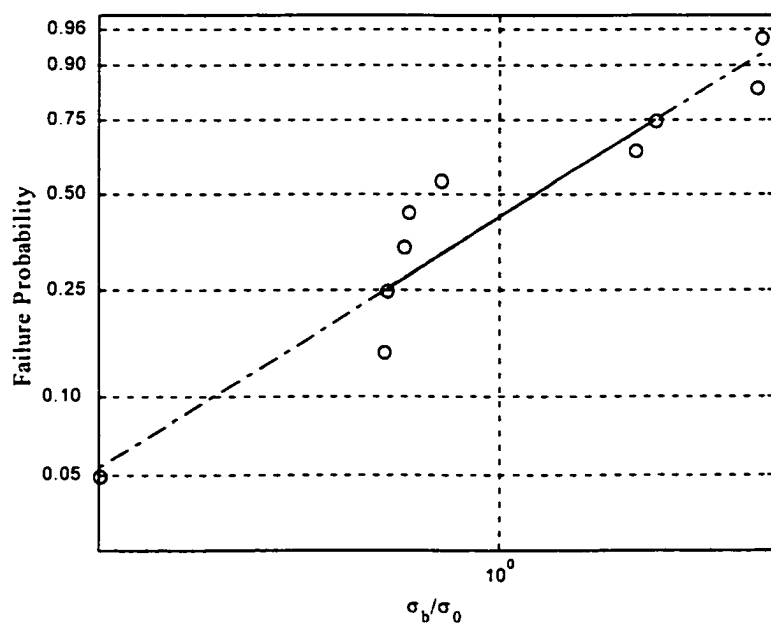
Figure 5. 3 Weibull probability plot of the biaxial flexural strength of 2A from the piston-on-3-ball experiments at 800°C.

Figure 5. 4 Weibull probability plot of the biaxial flexural strength of 3A from the piston-on-3-ball experiments at 800°C.

Figure 5. 5 Weibull probability plot of the biaxial flexural strength of 1Y from the piston-on-3-ball experiments at 800°C.

Figure 5. 6 Weibull probability plot of the biaxial flexural strength of 2Y from the piston-on-3-ball experiments at 800°C.

Figure 5. 7 Weibull probability plot of the biaxial flexural strength of 3Y from the piston-on-3-ball experiments at 800°C.

Table 5. 8
Weibull parameters fitted from experimental results and biaxial flexural strengths at 800°C

Ceramic Alias	Weibull Parameters		Strength (MPa)	
	m	V_c	Mean	std.
8YSZ	8.48	0.63	237.6	30.1
	(1.4, 15.6)*	(0.29, 0.98)		
1A	11.59	0.64	248.8	22.2
	(-16.3, 39.4)	(0.15, 1.12)		
2A	11.64	0.60	254.6	26.2
	(2.1, 21.1)	(0.21, 0.99)		
3A	7.61	0.62	222.7	35.5
	(-12.8, 28.0)	(0.05, 1.20)		
1Y	5.76	0.64	179.8	37.1
	(1.0, 10.5)	(0.22, 1.05)		
2Y	10.88	0.60	199.5	22.9
	(1.9, 19.8)	(0.19, 1.01)		
3Y	11.05	0.59	237.9	29.9
	(-0.1, 22.2)	(0.00, 1.18)		

* Inside the brackets is the 95% confidence interval.

The conclusion that Weibull modulus increases with increasing temperature can also be observed from the experimental results on the 2A substrates at different temperatures. Table 5.9 lists the Weibull parameters fitted from the experimental results and biaxial flexural strengths of 2A substrates at different temperatures, and the associated linearized Weibull plots are shown in Figures 3.7, 5.8, 5.9, 5.3, and 5.10.

Table 5. 9
Weibull parameters fitted from experimental results and biaxial flexural strengths
of 2A substrates at different temperatures

Temperatures	24°C	300°C	500°C	800°C	1000°C
m	7.93	7.61	8.80	11.64	12.17
	(4.30, 11.56)*	(1.05, 14.16)	(1.10, 14.51)	(2.14, 21.15)	(-1.55, 25.88)
V_e	0.62	0.59	0.61	0.60	0.57
	(0.30, 0.93)	(-0.11, 1.29)	(0.22, 1.01)	(0.22, 0.99)	(-0.07, 1.21)
σ_F (MPa)	276.8	224.1	204.8	254.6	236.9
std. (MPa)	41.9	45.3	28.5	26.2	28.9

* Inside the brackets is the 95% confidence interval.
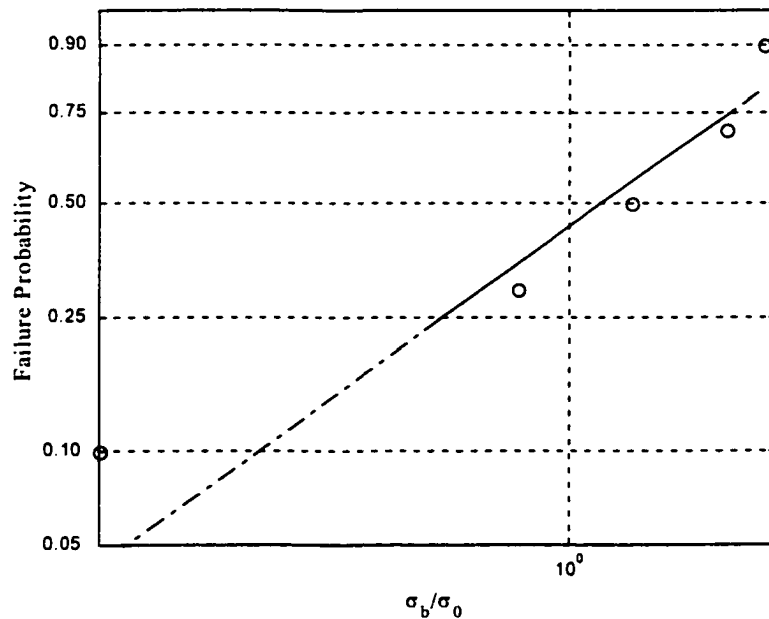
Figure 5. 8 Weibull probability plot of the biaxial flexural strength of 2A substrates
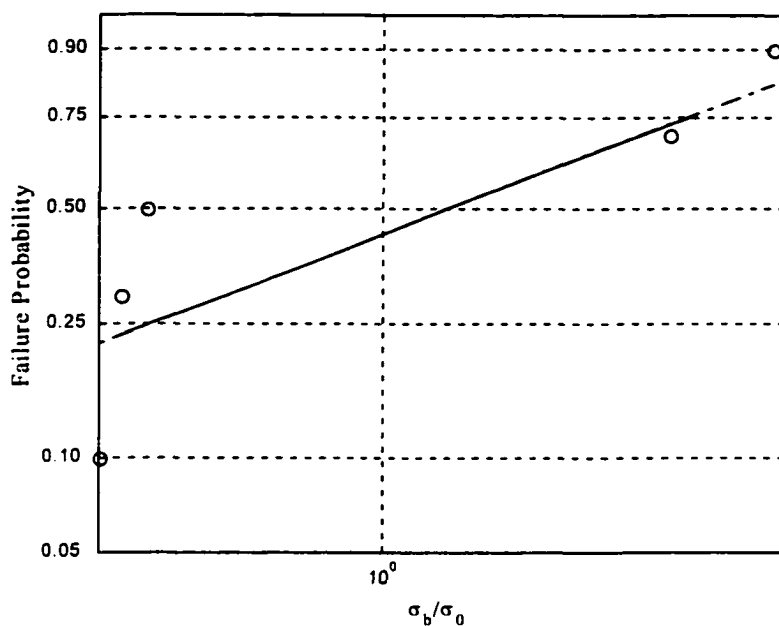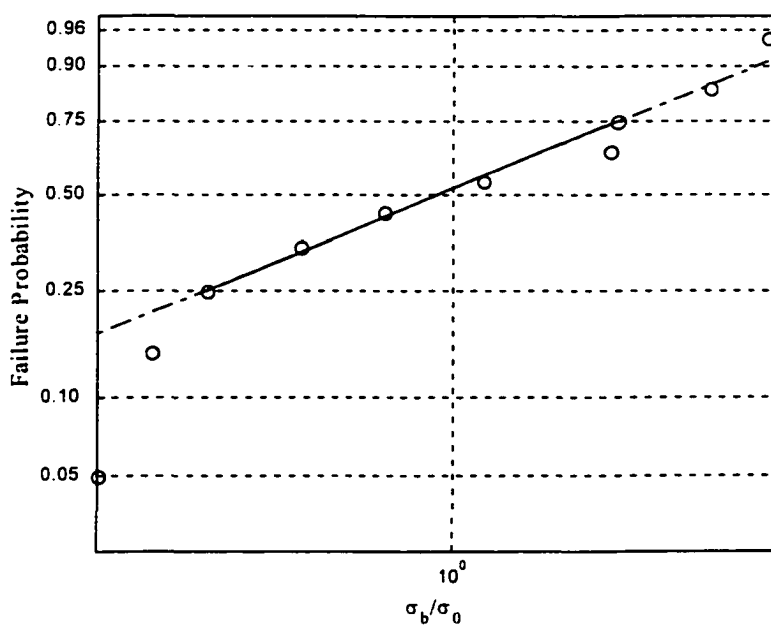from the piston-on-3-ball experiments at 300°C.
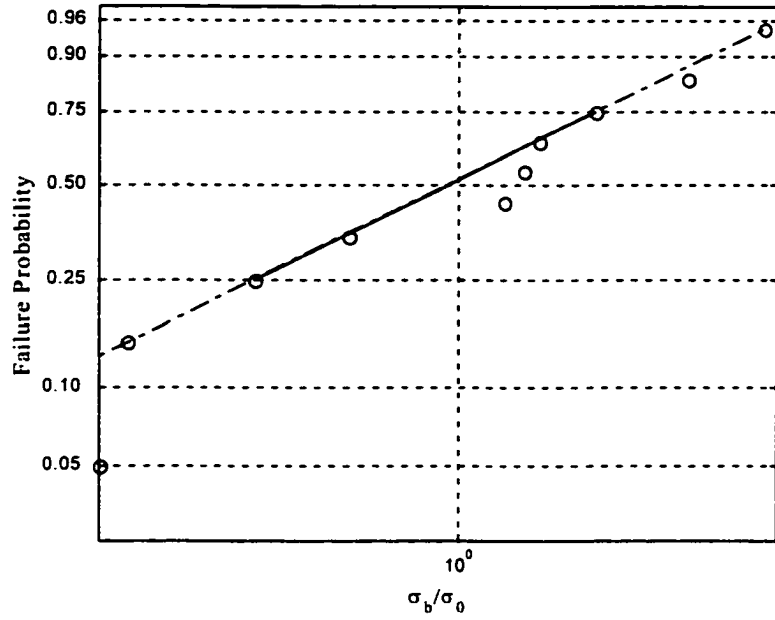
Figure 5. 9 Weibull probability plot of the biaxial flexural strength of 2A substrates from the piston-on-3-ball experiments at 500°C.
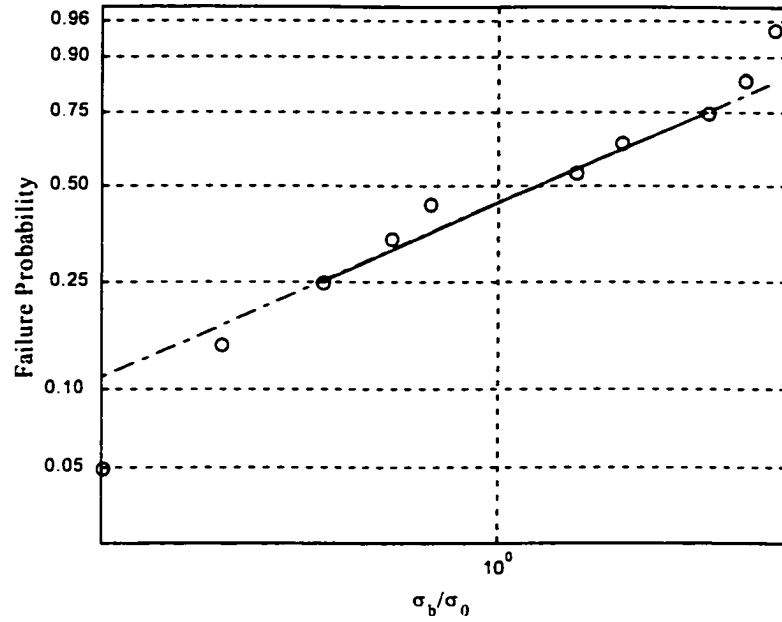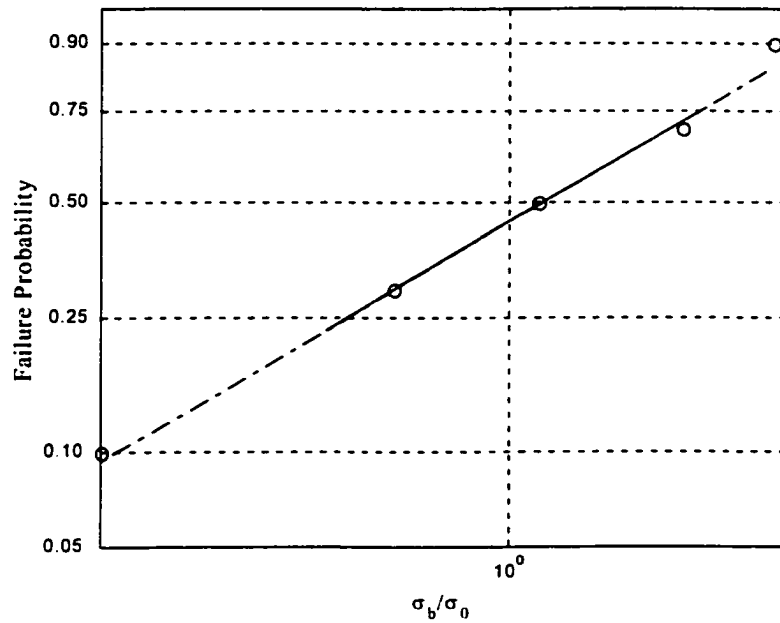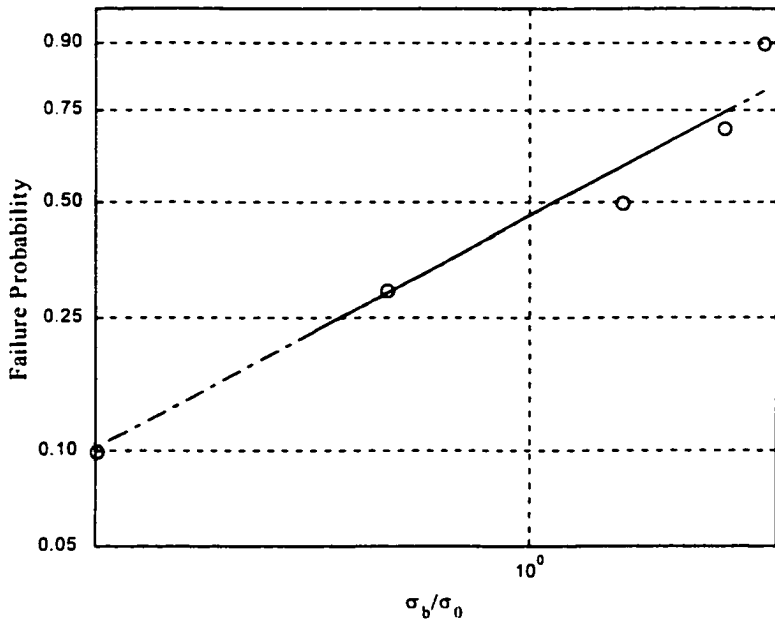

Figure 5. 10 Weibull probability plot of the biaxial flexural strength of 2A substrates from the piston-on-3-ball experiments at 1000°C.

The temperature dependences of the piston-on-3-ball biaxial flexural strength of 8YSZ, 2A, and 2Y are shown in Figures 5.11~5.13. The two-direction error-bars are sample standard deviations. The common characteristic of these temperature dependences is that the biaxial strengths show a minimum at 500°C. Although the biaxial flexural strengths are not as high as those at ambient temperature, this characteristic is similar to Mori et al.'s results (Mori et al., 1994). The strengths increase with increasing temperatures until at least 1000°C except that the biaxial strength of 2A substrates at 1000°C is lower than that at 800°C, but still higher than that at 500°C. This is probably due to the limited number of experimental data.
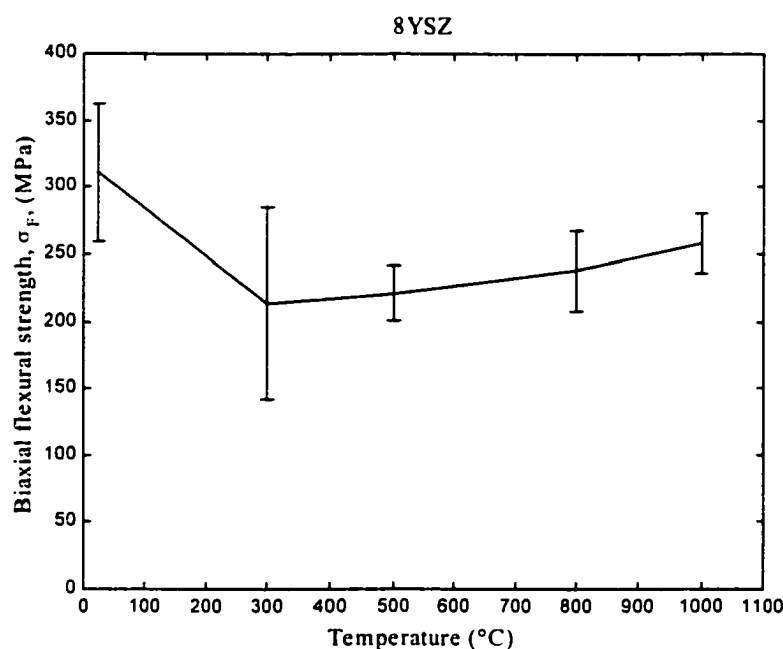
Figure 5. 11 Variation of biaxial flexural strength of 8YSZ substrates as a function of temperature.
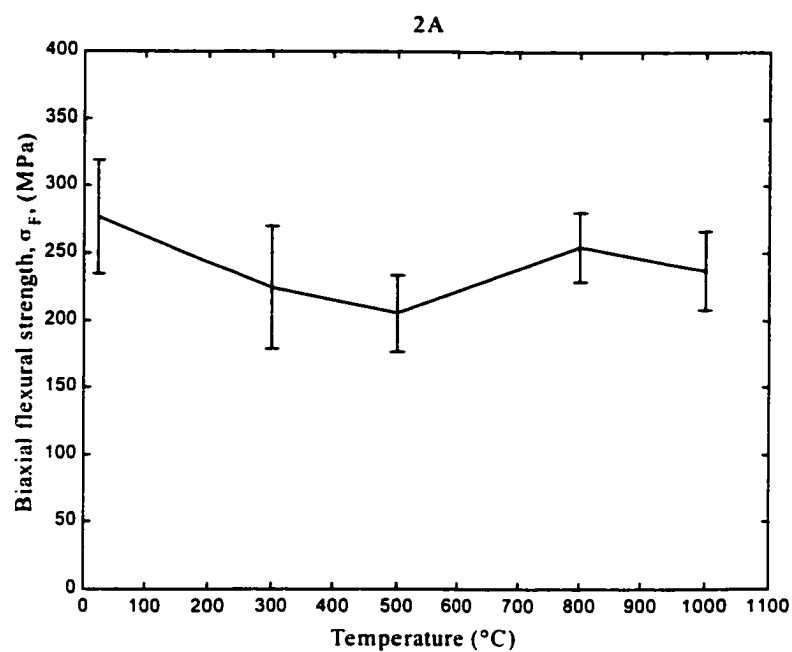
Figure 5. 12 Variation of biaxial flexural strength of 2A substrates as a function of temperature.
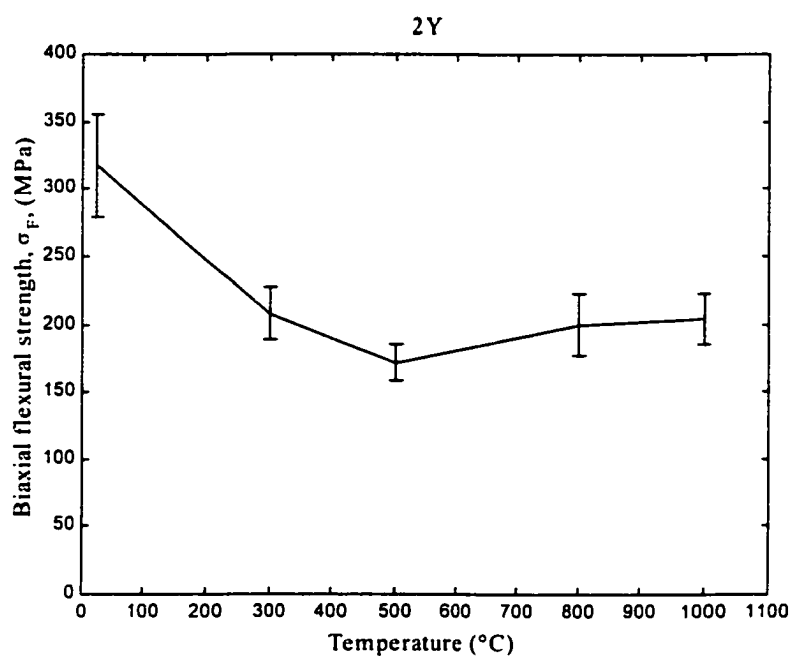
Figure 5. 13 Variation of biaxial flexural strength of 2Y substrates as a function of temperature.

Since there are not enough experimental data to form a statistically sound base, the conclusion that the biaxial strengths of 8YSZ, 2A, and 2Y show a minimum at 500°C cannot be derived from experimental results of other material compositions listed in Table 1.2. However, the general observation that the strengths at 800°C are higher than those at 500°C for all the material compositions is consistent with the above conclusion.

5.5 Summary

The quasi-static piston-on-3-ball biaxial flexural strength test method, which is an ASTM standard test method used to measure the biaxial flexural strength of ceramic substrates at room temperature, has been evolved into an experimental technique for measuring the biaxial flexural strength of ceramic substrates at elevated temperatures. 8YSZ and its doped versions listed in Table 1.2 have been tested with this experimental technique. The biaxial flexural strengths of these ceramic substrates showed a different characteristic at elevated temperatures from that at ambient temperature.

CHAPTER 6

EFFECTS OF DOPANTS ON THE BIAXIAL FLEXURAL

STRENGTH OF 8YSZ CERAMIC SUBSTRATES

One of the objectives of this research is to determine a material composition among those possible candidates listed in Table 1.2, which have been reported by another group that they possess approximately the same electric conductivity as pure 8YSZ material. Therefore, the mechanical properties of these material composition candidates must be compared. In other words, the effects of dopants on the biaxial flexural strength of 8YSZ ceramic substrates must be investigated, since the biaxial flexural strength is the main mechanical property concerned in this research.

6.1 Quasi-static biaxial flexural strength

The variations of strength as a function of material composition at different temperatures are shown in Figures 6.1~6.10 with data from Tables 3.3 and 5.1~5.7. The two-direction error-bars are sample standard deviations.

The Al_2O_3 additive with amount up to 3 mol% cannot change the biaxial flexural strength of 8YSZ material significantly if the scatter characteristic of ceramic materials is taken into account. Figures 6.1~6.5 show that the biaxial flexural strengths of 8YSZ, 1A,

2A, and 3A are approximately the same with temperature range from ambient to 1000°C. Although some differences exist among their mean strengths, the variations are within their standard deviations.
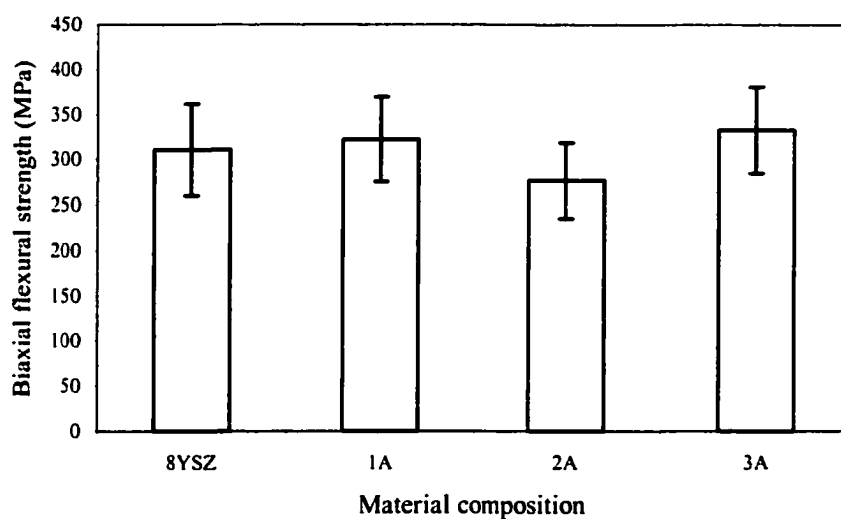
Figure 6. 1 Variation of biaxial flexural strength of 8YSZ material as a function of the amount of Al_2O_3 additive at ambient temperature with error-bars representing standard deviations.
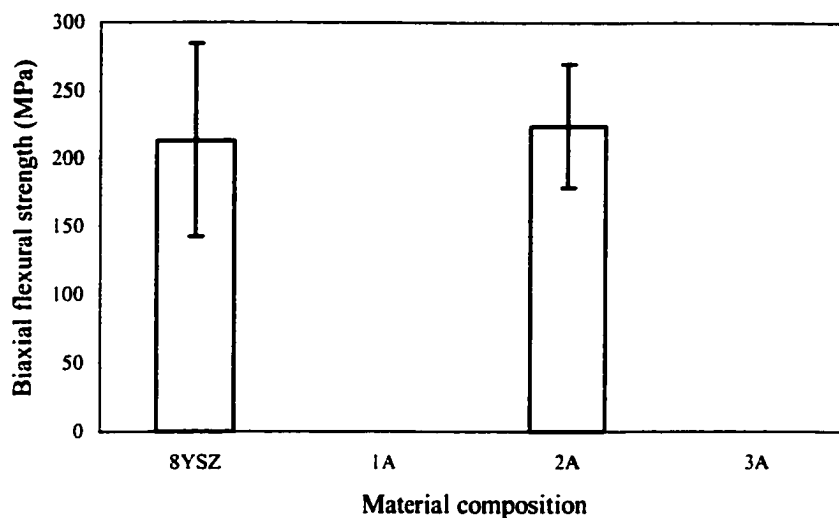
Figure 6. 2 Variation of biaxial flexural strength of 8YSZ material as a function of the amount of Al₂O₃ additive at 300°C with error-bars representing standard deviations.
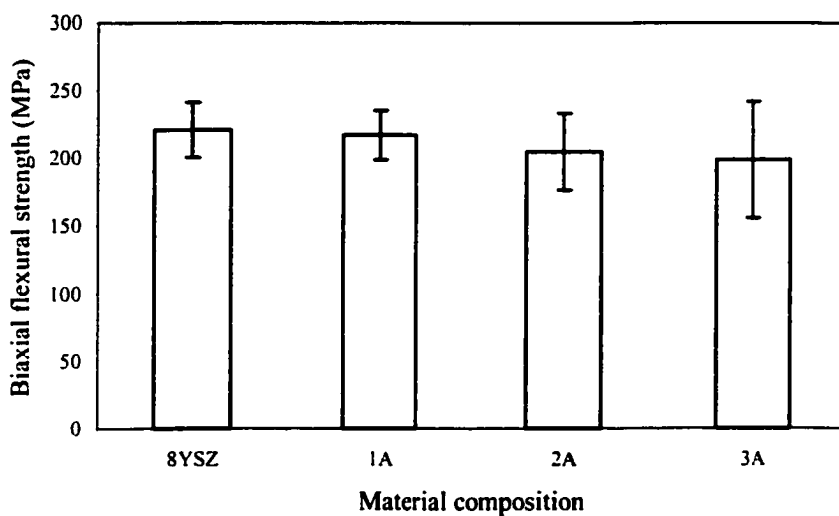
Figure 6. 3 Variation of biaxial flexural strength of 8YSZ material as a function of the amount of Al₂O₃ additive at 500°C with error-bars representing standard deviations.

Figure 6. 4 Variation of biaxial flexural strength of 8YSZ material as a function of the amount of Al₂O₃ additive at 800°C with error-bars representing standard deviations.

Figure 6. 5 Variation of biaxial flexural strength of 8YSZ material as a function of the amount of Al₂O₃ additive at 1000°C with error-bars representing standard deviations.

Figure 6. 6 Variation of biaxial flexural strength of 8YSZ material as a function of the amount of 3YSZ additive at ambient temperature with error-bars representing standard deviations.
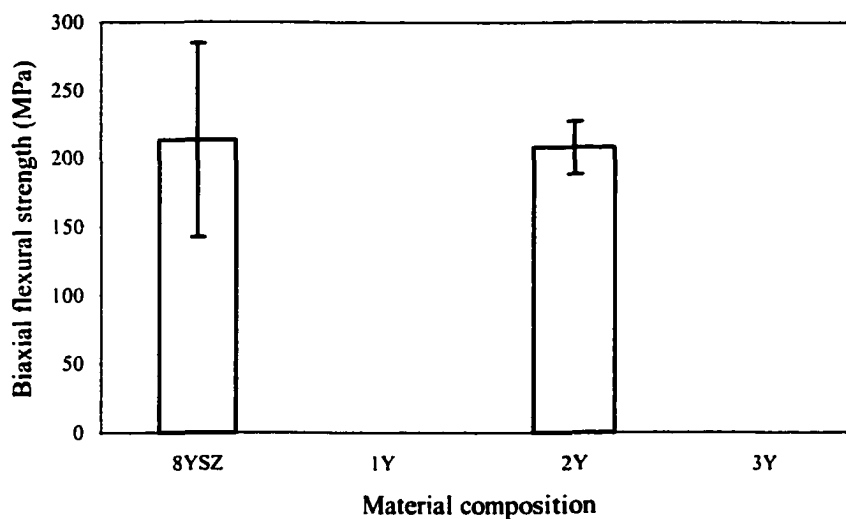
Figure 6. 7 Variation of biaxial flexural strength of 8YSZ material as a function of the amount of 3YSZ additive at 300°C with error-bars representing standard deviations.
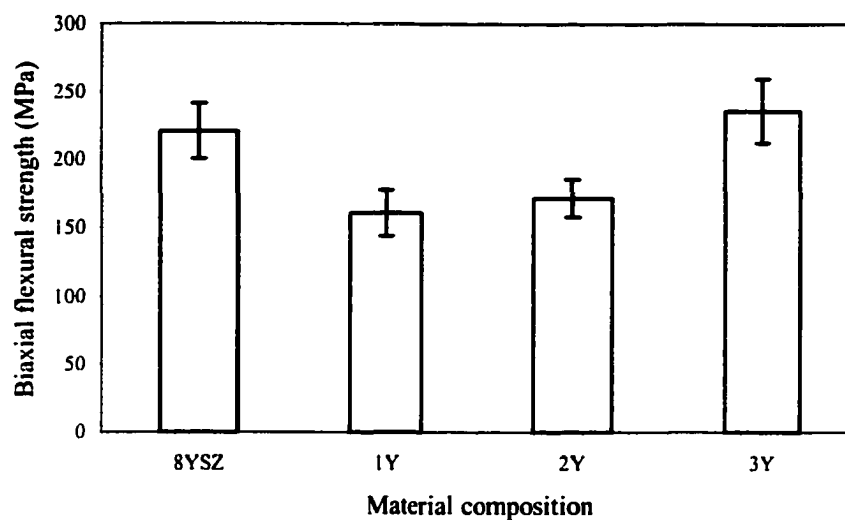
Figure 6. 8 Variation of biaxial flexural strength of 8YSZ material as a function of the amount of 3YSZ additive at 500°C with error-bars representing standard deviations.

Figure 6. 9 Variation of biaxial flexural strength of 8YSZ material as a function of the amount of 3YSZ additive at 800°C with error-bars representing standard deviations.

Figure 6. 10 Variation of biaxial flexural strength of 8YSZ material as a function of the amount of 3YSZ additive at 1000°C with error-bars representing standard deviations.

The observation that the Al_2O_3 additive with amount up to 3 mol% cannot change the biaxial flexural strength of 8YSZ material significantly is also supported by the fact that the Weibull parameters of 8YSZ, 1A, 2A, and 3A compositions at ambient temperature (see Table 3.3) are approximately the same. Figure 6.11 shows the variation of the Weibull modulus, m, of the biaxial flexural strength of 8YSZ material as a function of the amount of Al_2O_3 additive at ambient temperature. The error-bar represents 95% confidence intervals. The associated representative volumes, V_e, have the same value, 0.62, except of a small difference for 2A, whose representative volume is 0.61. The variation of the representative volume of the Weibull distribution of the biaxial flexural strength of 8YSZ material as a function of the amount of Al_2O_3 additive at ambient temperature is shown in Figure 6.12. At 800 °C, the 95% confidence intervals of the

Weibull moduli, Figure 6.13, are much bigger than those at ambient temperature. This is probably due to lack of enough experimental data for statistical data processing. However, the variation of the Weibull modulus, m, of the biaxial flexural strength of 8YSZ material as a function of the amount of Al_2O_3 additive at 800°C is not significant. In other words, the Al_2O_3 additive with amount up to 3 mol% has little effects on the biaxial flexural strength of 8YSZ material at 800°C. This is further confirmed by the behavior of the Weibull representative volumes of these material compositions, which is shown in Figure 6.14. The variation range of the Weibull representative volume of the biaxial flexural strength of 8YSZ material as a function of the amount of Al_2O_3 additive up to 3 mol% at 800°C is from 0.60 to 0.64.
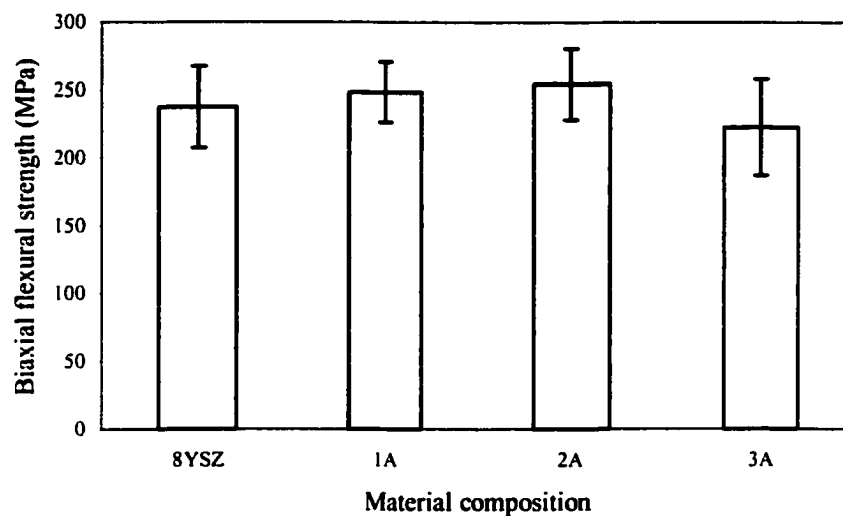

Figure 6. 11 Variation of the Weibull modulus, m, of the biaxial flexural strength of 8YSZ material as a function of the amount of Al_2O_3 additive at ambient temperature with error-bars representing 95% confidence intervals.
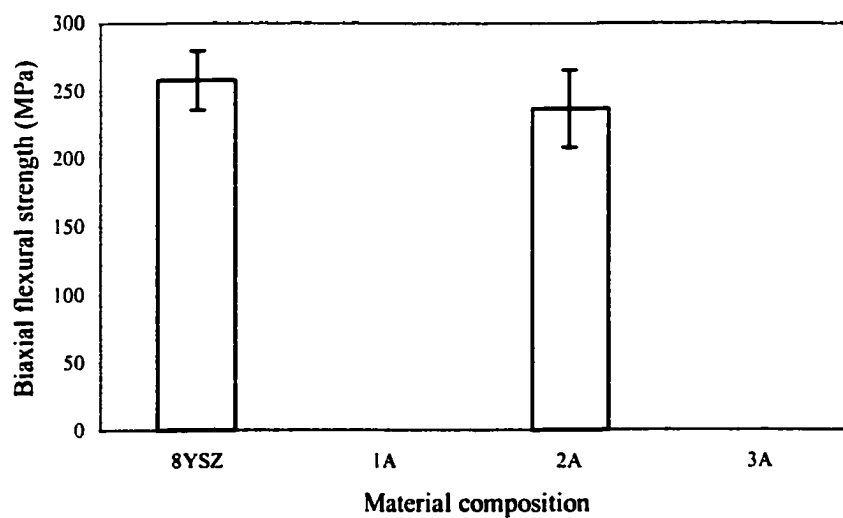
Figure 6. 12 Variation of the Weibull representative volume, V_r, of the biaxial flexural strength of 8YSZ material as a function of the amount of Al_2O_3 additive at ambient temperature with error-bars representing 95% confidence intervals.

Figure 6. 13 Variation of the Weibull modulus, m, of the biaxial flexural strength of 8YSZ material as a function of the amount of Al_2O_3 additive at 800°C with error-bars representing 95% confidence intervals.
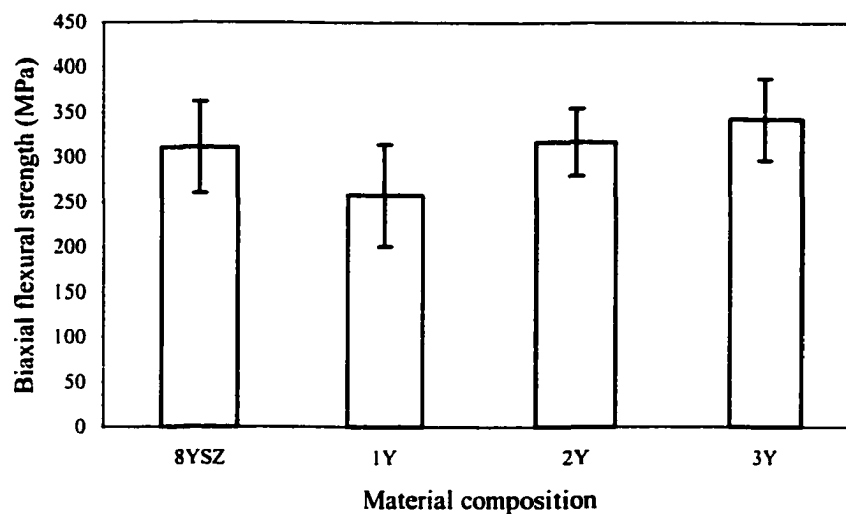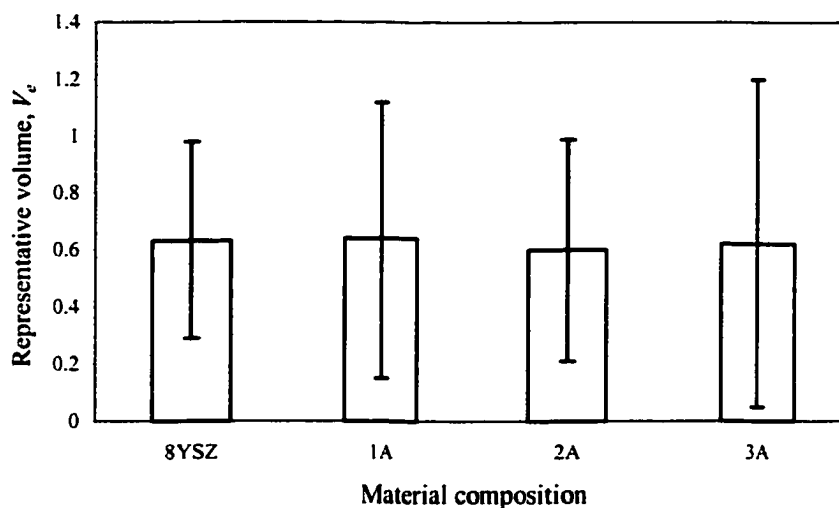
Figure 6. 14 Variation of the Weibull representative volume, V_e of the biaxial flexural strength of 8YSZ material as a function of the amount of Al_2O_3 additive at 800°C with error-bars representing 95% confidence intervals.

Although the effects of Al_2O_3 additive with amount up to 3 mol% on the biaxial flexural strength of 8YSZ material are insignificant, it is difficult to make the same concl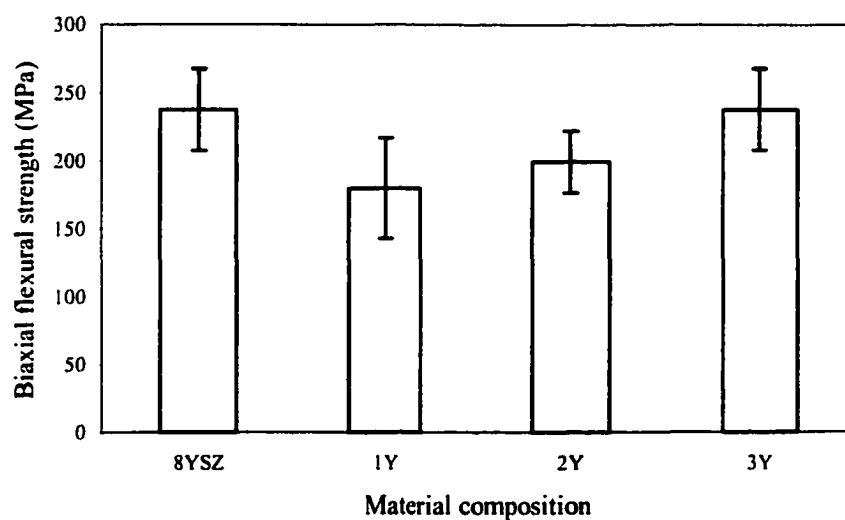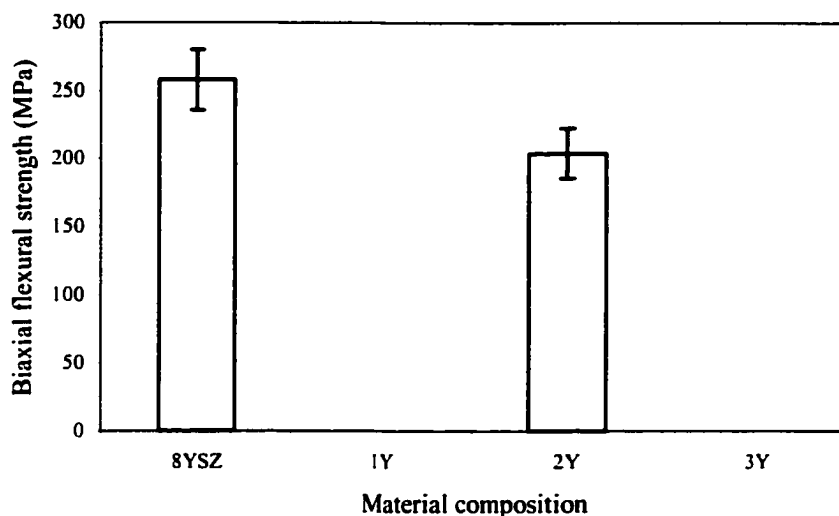usion to the 3YSZ additive with amount up to 30 wt%. Figures 6.6~6.10 show the variation of biaxial flexural strength of 8YSZ material as a function of the amount of 3YSZ additive at different temperatures. The strengths of 8YSZ and 2Y are in a same level at ambient temperature and 300°C. At temperatures range from 500°C to 1000°C, the strength of 2Y is obviously lower than that of 8YSZ, regardless of the fact that their error-bars cover a common range. In fact, the 3YSZ additive increases the degradation of the biaxial flexural strength of 8YSZ material at elevated temperature 500°C and higher. The strength of 1Y is lower and the strength of 3Y is higher than that of the 8YSZ at

ambient temperature. In addition, Figures 6.6, 6.8 and 6.9 show that the strength of the

3YSZ-doped 8YSZ increases with increasing amount of 3YSZ from 10 wt% to 30 wt%.

The variations of Weibull parameters of 3YSZ doped 8YSZ are more obvious

than those of Al_2O_3 doped 8YSZ, which can be seen in Figures 6.15 and 6.17. Although

Weibull modulus of 1Y is lower than the others at both ambient temperature and 800°C,

it is difficult to make a conclusion because of the large 95% confidence intervals of the

other materials, which may be due to limited number of experimental data. However, the

variation range of the Weibull representative volume of the biaxial flexural strength of

8YSZ material as a function of the amount of 3YSZ additive up to 30 wt% is relatively

small, which is from 0.61 to 0.64 at ambient temperature and from 0.59 to 0.64 at 800°C.
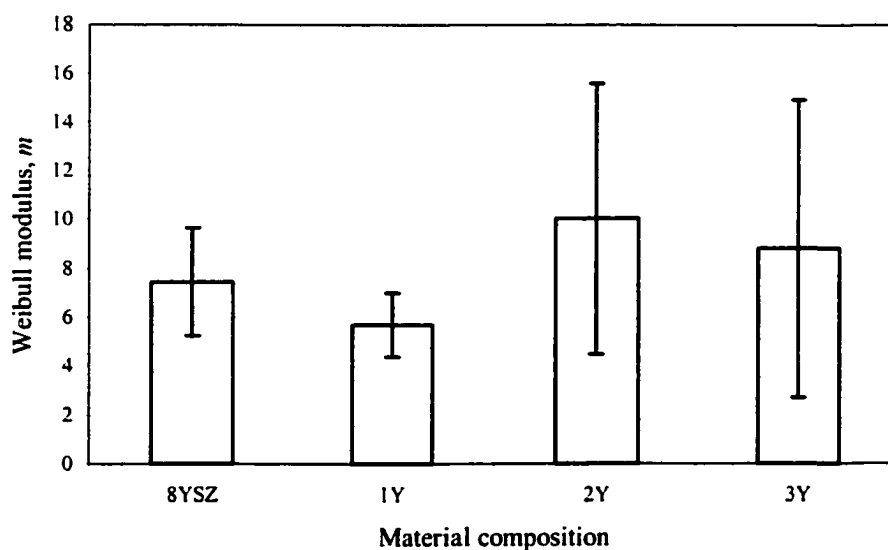
Figure 6. 15 Variation of the Weibull modulus, *m*, of the biaxial flexural strength of 8YSZ material as a function of the amount of 3YSZ additive at ambient temperature with error-bars representing 95% confidence intervals.
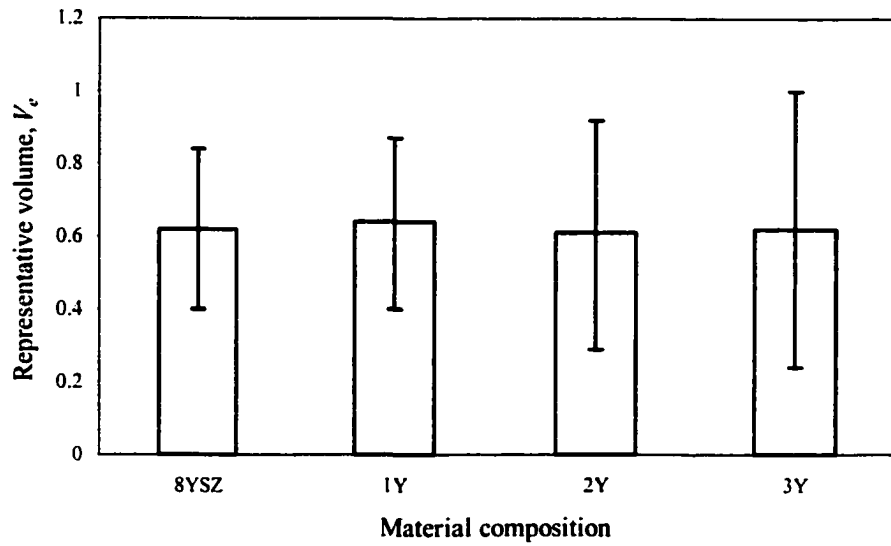
Figure 6. 16 Variation of the Weibull representative volume, V_e, of the biaxial flexural strength of 8YSZ material as a function of the amount of 3YSZ additive at ambient temperature with error-bars representing 95% confidence intervals.
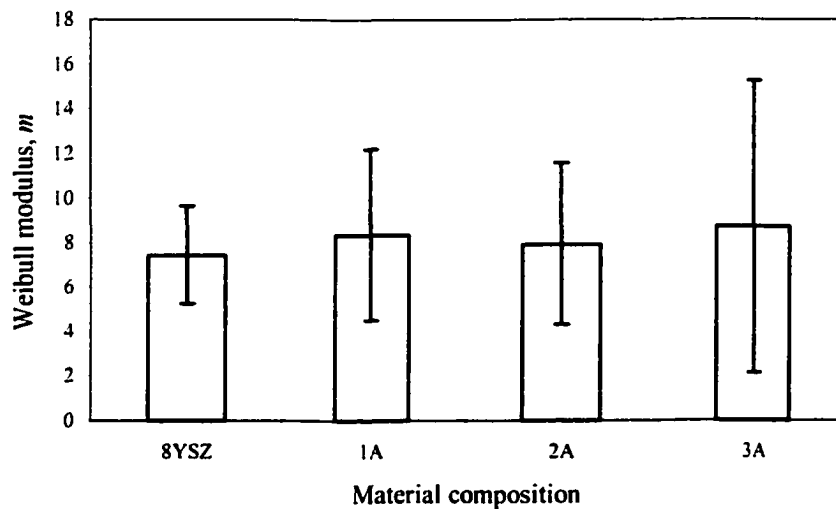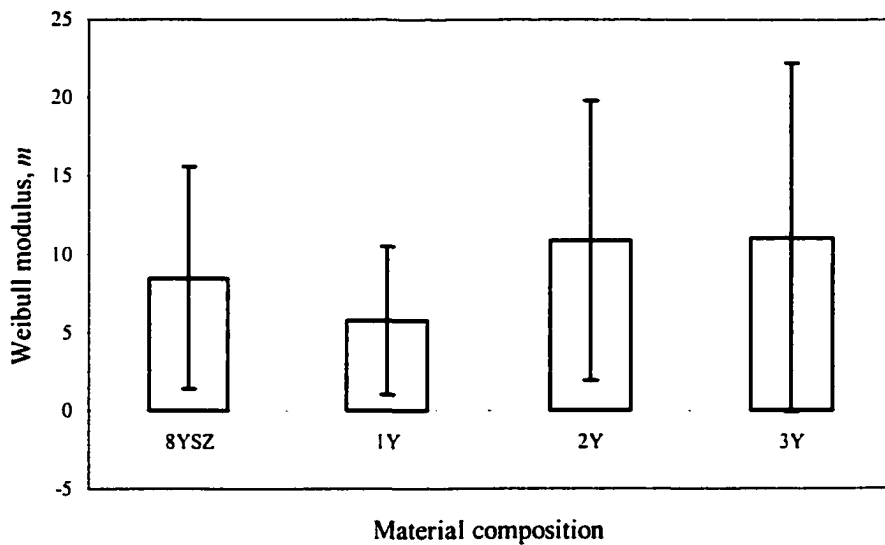

Figure 6. 17 Variation of the Weibull modulus, m, of the biaxial flexural strength of 8YSZ material as a function of the amount of 3YSZ additive at 800°C with error-bars representing 95% confidence intervals.
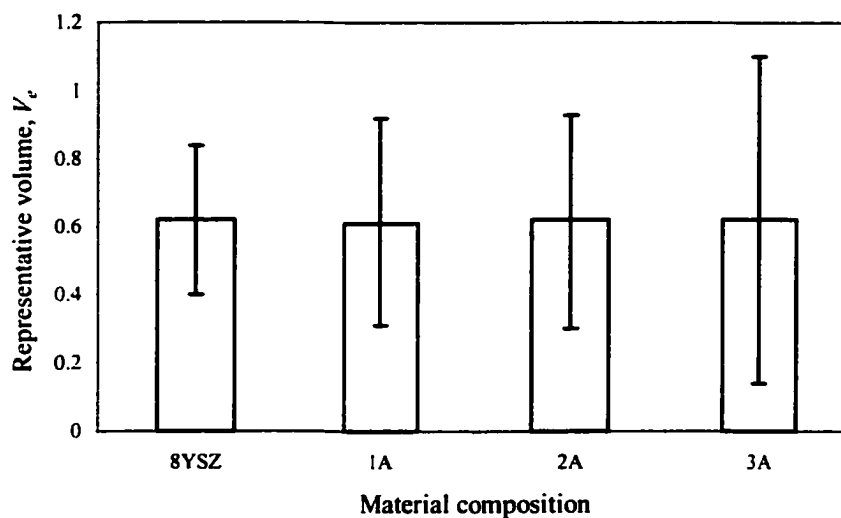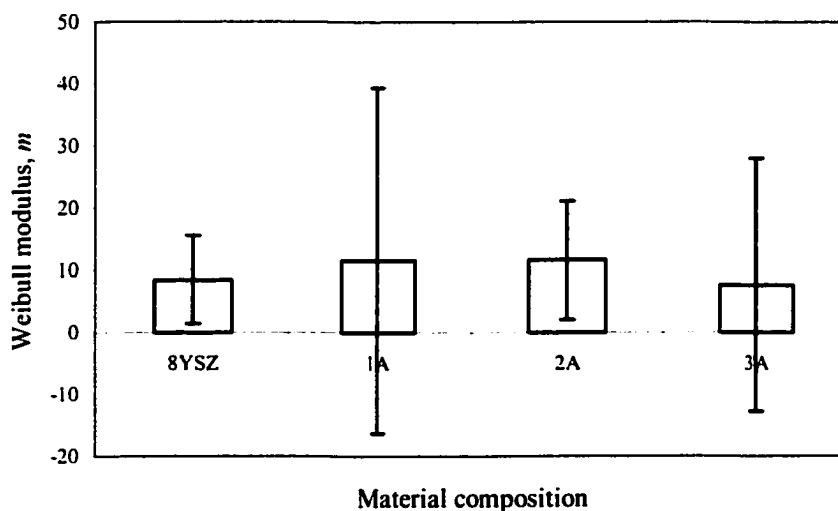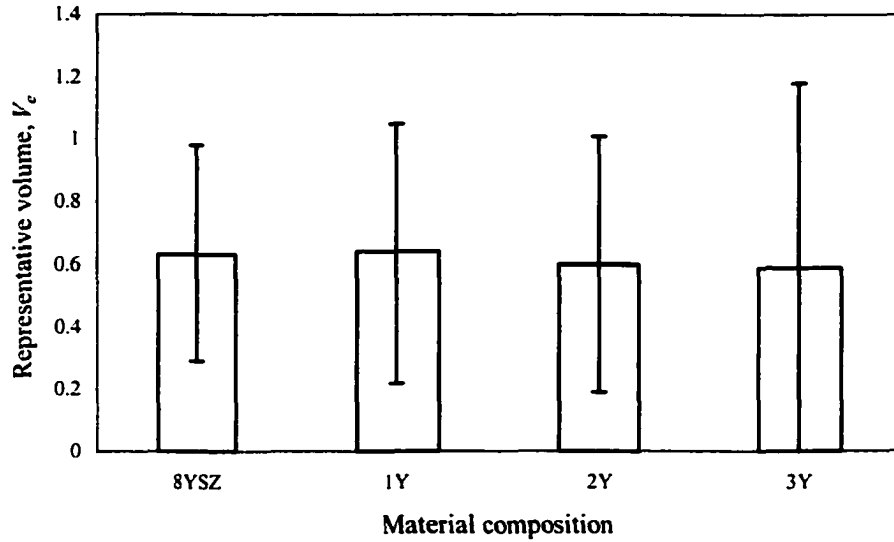
Figure 6. 18 Variation of the Weibull representative volume, V_e, of the biaxial flexural strength of 8YSZ material as a function of the amount of 3YSZ additive at 800°C with error-bars representing 95% confidence intervals.

In the linear elastic fracture mechanics approach such as the Irwin approach and Griffith approach (Jayatilaka, 1979), strength is found to depend on a combination of a material property (intrinsic) and a flaw size (extrinsic). The associated material property is toughness, K_{IC}, or critical energy release rate, G_{IC}, and it depends on the microstructure of the material such as grain size, boundary phase, and additives. In the Irwin approach, the mode I fracture toughness for a brittle solid is expressed as

$$K_{IC} = \sigma_F \sqrt{c} Y \tag{6.1}$$

where σ_F is the strength, c the appropriate crack size, and Y a geometrical factor. From this relationship, if the value of fracture toughness, K_{IC}, is known for a material, the size of a flaw it can tolerate at a given stress can be calculated. Alternatively, if both the

strength and fracture toughness are known, it is possible to estimate the critical flaw size. Thus, the knowledge of the toughness is important to evaluate the mechanical behavior of a ceramic material. In the next section, a micro indentation technique is employed to evaluate the fracture toughness of the ceramic materials listed in Table 1.2. The test results are used to further evaluate the mechanical properties of these material compositions.

6.2 Fracture toughness evaluation by Vickers micro-indentation technique

6.2.1 Introduction

Indentation techniques are well developed for hardness study. The American Society of Testing and Materials (ASTM) has developed a standard test method for Vickers indentation hardness of advanced ceramics (ASTM C 1327-96a, 1996). Conventionally, indentation is considered micro when the applied indenter load is less than 5 N; otherwise, it is called macro indentation.

The indentation techniques have also been widely used for studying toughness of brittle materials such as ceramics and glasses since the surface crack traces were first recognized as being indicative of the fracture toughness of the material by Palmqvist in 1957. The mode-I fracture toughness (K_{IC}) and microstructure were examined in arc-melted ZrO_2-Y_2O_3 alloys with an yttria content up to 8 mol% by Sakuma, Eda, and Suto (1983). They found that mode-I fracture toughness (K_{IC}) changed markedly with an yttria

content between 1 and 3 mol%, the peak value of about 15 MPa m$^{1/2}$ being observed in 1.8 mol% yttria stabilized zirconia. The marked change in the mode-I fracture toughness (K_{IC}) with yttria content was found being related to the microstructural change in the alloy.

In general, the procedure of indentation toughness test includes producing an indentation on a plane surface of the material by a standard hardness tester and studying the induced cracks by a microscope. With the indenter load and the dimensions of the induced cracks, it is possible to evaluate the toughness of the material. For example, the Vickers hardness tester usually makes a diamond indentation with cracks emanating from the diamond corners as schematically illustrated in Figure 6.19.
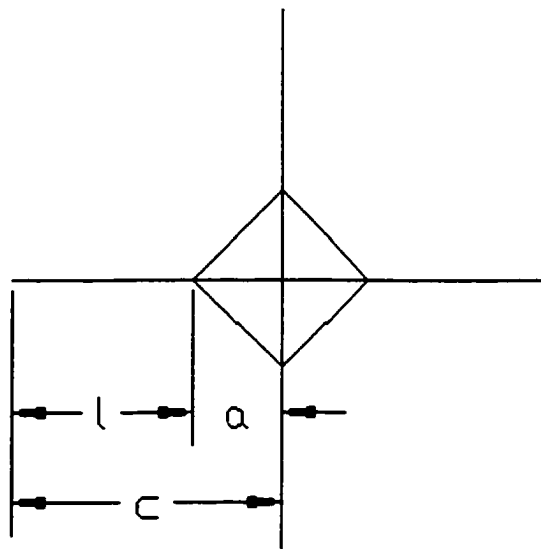
Figure 6. 19 Plane view of Vickers indentation with radial cracks.

Many models have been proposed for the evaluation of toughness by using the indentation techniques. Ponton and Rawlings reviewed 19 equations published in the literature (Ponton and Rawlings, 1989a) and examined these equations by experiments (Ponton and Rawlings, 1989b). For most models published in the literature, the c/a or l/a ratio was limited in a range. For example, Niihara et al. proposed the following equation based on the Palmqvist cracks which requires l/a to be between 0.25 and 2.5 (Niihara, Morena, and Hasselman, 1982).

$$K_{IC} = 0.0193 \left(H_V a \right) \left(\frac{E}{H_V} \right)^{\frac{2}{5}} \left(l^{-\frac{1}{2}} \right)$$ (6.2)

where K_{IC} is mode-I toughness, E Young's modulus, $H_V = \frac{0.4636 P}{a^2}$ Vickers hardness, and P indenter load.

The advantage of this indentation toughness technique is time and cost effective. The specimen preparation is relatively simple, requiring only a plane surface. At least 10 tests can be performed on a surface of only 100 mm^2. However, the disadvantage of this technique is the difficulty in accurate measurements of the crack length c or l. The crack length is usually measured under an optical microscope. The indentation induced cracks are often hard, if not impossible, to observe. Therefore, Ponton and Rawlings recommended a minimum indenter load of about 50 N. They believed that only to apply indenter load high enough could produce visible cracks for accurate measurement. This opinion prevailed in the literature and some researcher claimed that micro indentation

produced no cracking (Anton and Subhash, 2000). Thus, almost all indentation toughness tests were performed on macro hardness testers.

In order to improve the observability, the specimen surfaces were polished to at least 5 μm diamond finish by most researchers. Although Ponton and Rawlings claimed that processes such as polishing could produce residual stresses on the surface to prevent correct test results (Ponton and Rawlings, 1989b), polishing seemed to be a necessary process for specimen preparation in the literature. However, almost all the Vickers indentation models so far are based on the assumption that there are no pre-existing surface stresses. Although proper heat treatment could remove the residual stresses, it may change the properties of the material either.

Thin ceramic substrates are widely used as electrolytes in solid oxide electrolyzers. The solid oxide electrolytes are typically made by a tape-cast process. After sintering, the products are usually in the form of thin sheets. The thickness of these sheets is typically 0.5 mm or less in engineering applications. As a result, indenter load as high as 50 N breaks the specimen substrates. Actually, most such thin ceramic substrates can only be indented by micro indentation. Cook and Pharr (1990) found that radial crack forms extremely early (possibly instantly) in the loading process (typically 0.8 N). This fact indicates that indentation cracking is possible on thin sheets if the load is low enough, which leads to micro indentation toughness study in this research.

Since as-fired surface condition is usually used in service and polishing surface may get incorrect test results, it is necessary to develop a micro indentation toughness test technique for thin ceramic substrates without surface polishing. The critical aspect of this

technique is how to observe and measure the micro cracks induced by micro indentations effectively and economically. The purposes of this section are to show that micro indentation can induce cracks and these cracks can be measured accurately enough for the evaluation of toughness by a standard optical microscope.

6.2.2 Experimental procedure

The specimens used for these micro indentation toughness tests are those broken pieces of quasi-static piston-on-3-ball experimental test specimens. The micro Vickers indentation was made using a MICROMET®3 micro hardness tester which was the product of BUEHLER LTD. The indenter load applied was 4.91 N—in practice, the indenter load should be determined by trial and error to ensure the c/a to be in a range required by the associated model for the evaluation of the fracture toughness. The half-diagonal length (a) of the indentation was measured directly by the hardness tester.

The total length ($2c$) of the induced crack was measured by an IM 35 inverted microscope of ZEISS. Under normal lighting conditions, the induced cracks could not be observed even the image was magnified 500 times. When the magnification was switched to 1000, the image could not be focused anymore due to surface roughness. It seemed impossible to observe any cracks by this microscope. However, once a shadow was introduced close to the indentation and the focusing was properly adjusted, the expected cracks manifested. Figures 6.20 and 6.21 illustrate the effect of shadows for crack observation.
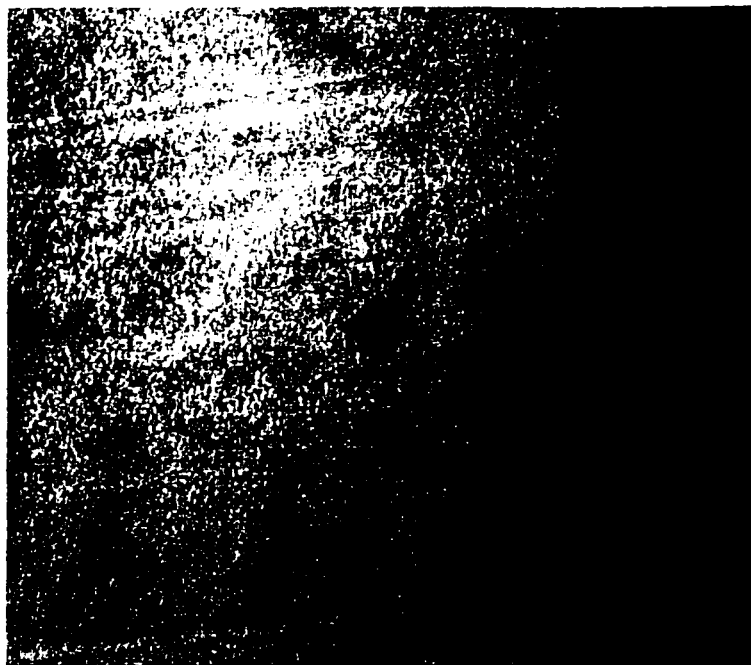
Figure 6. 20 Vickers indentation in 8YSZ.
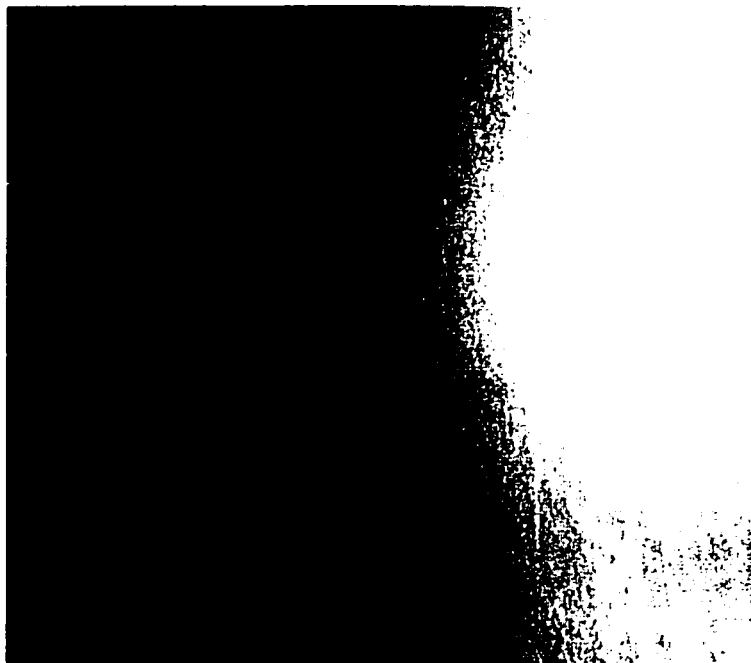
Figure 6. 21 The same Vickers indentation as in Figure 6.20 with shadows introduced from left.

The method to introduce a shadow is only the adjustment of the position of one of the illuminating lenses. The IM 35 inverted microscope is a metallurgical microscope. The illuminating ray path starts from a light source and a lamp condenser. Afterwards there are two illuminating lenses. Sliding the last illuminating lens to the halfway (not normal working position) can cast a shadow on the image. The same method was tried on a BUEHLER® metallurgical microscope (BUEHLER® VERSAMET 3 METALLOGRAPH) and the same effect was observed.

6.2.3 Results and discussions

All the material compositions listed in Table 1.2 were tested using this experimental technique. More than 30 tests were performed on each composition. With the indenter loads and the dimensions of indentation and cracks, the test results were processed to obtain toughness value using the following equations (Selçuk and Atkinson, 2000).

$$K_{IC} = 0.035 \frac{H_V a}{\phi} \left(\frac{E\phi}{H_V} \right)^{\frac{2}{5}} \left(\frac{l}{a} \right)^{-\frac{1}{2}} \text{ for } 0.25 \leq \frac{l}{a} \leq 2.5 \tag{6.2}$$

$$K_{IC} = 0.0143 \left(\frac{E}{H_V} \right)^{\frac{2}{3}} \left(\frac{P}{c^{\frac{3}{2}}} \right) \left(\frac{l}{a} \right)^{-\frac{1}{2}} \text{ for } 1 \leq \frac{l}{a} \leq 2.5 \tag{6.3}$$

$$K_{IC} = 0.055 \frac{H_V a^{\frac{1}{2}}}{\phi} \left(\frac{E\phi}{H_V} \right)^{0.4} \log_{10} \left(\frac{8.4a}{c} \right) \tag{6.4}$$

and

$$K_{IC} = H_V a^{1/2} \left(\frac{E}{H_V} \right)^{2/5} \left(10^F \right)$$

(6.5)

where E is the Young's modulus, H_V the Vickers hardness, ϕ a dimensionless constant (taken to be 2.7), P the applied load, a the half length of the indenter diagonal, c the crack length from the center of the indent, and l the crack length from the corner of the indent (Figure 6.19). In Equation (6.5),

$$F = -1.59 - 0.34x - 2.02x^2 + 11.23x^3 - 24.97x^4 + 16.32x^5$$

where $x = \log_{10} \left(\frac{c}{a} \right)$.

The reason for selecting these four equations is not only that they have been reported to be valid for the Palmqvist-type cracks and more accurate in determining toughness than others, but also that these equations have been used by Selçuk and Atkinson (2000) to evaluate the toughness of 8YSZ ceramic material using macro indentation toughness method, therefore making it possible to compare the test results from different sources.

The Young's modulus used in Equations (6.2)–(6.5) to evaluate toughness values was chosen to be 216 GPa, which was reported by Selçuk and Atkinson (2000) to be the Young's modulus of 8YSZ ceramic material. Through investigating load-deflection curves obtained from quasi-static piston-on-3-ball experiments, the Young's moduli of those material compositions listed in Table 1.2 are at the same level. The final results of micro Vickers indentation toughness tests are those in Table 6.1.

Table 6. 1
Fracture toughness values (K_{IC}, MPa· $m^{1/2}$) measured by micro Vickers indentation technique at ambient temperature

Material	Equation (6.2)		Equation (6.3)		Equation (6.4)		Equation (6.5)	
	K_{IC}	std.	K_{IC}	std.	K_{IC}	std.	K_{IC}	std.
8YSZ	1.90	0.10	1.22	0.21	1.89	0.13	1.80	0.16
1A	1.91	0.07	1.21	0.15	1.89	0.10	1.81	0.12
2A	2.00	0.05	1.41	0.11	2.02	0.06	1.96	0.07
3A	1.99	0.09	1.33	0.19	2.00	0.11	1.93	0.14
1Y	1.94	0.06	1.25	0.12	1.93	0.08	1.86	0.09
2Y	2.04	0.08	1.52	0.19	2.07	0.10	2.02	0.11
3Y	2.23	0.12	2.01	0.32	2.27	0.11	2.24	0.11

Although the toughness values evaluated by different equations have some systematical biases, these results are very useful for material comparison purposes. Table 6.1 shows that the Al_2O_3 additive with amount up to 3 mol% has little effects on the toughness of 8YSZ at ambient temperature, which is consistent with the observations about the biaxial flexural strengths of these material compositions. The toughness of 3YSZ doped 8YSZ materials increases slightly with increasing 3YSZ additive amount up to 30 wt% at ambient temperature. This can be part of the reasons for the behavior of the biaxial flexural strengths of 3YSZ doped 8YSZ materials. The biaxial flexural strength of 8YSZ increases slightly with increasing 3YSZ additive amount up to 30 wt% at ambient temperature.

To investigate the effects of surface polishing on the toughness values, another group of micro Vickers indentation toughness tests were performed on a surface-polished specimen. The test results, which are listed in Table 6.2, confirmed that the surface polishing could significantly change the test results. For design purposes, the tests must be conducted on a specimen with the same surface condition as that in practical service; otherwise, the specimen must be rigorously heat treated to recover the surface condition.

Table 6. 2
Fracture toughness values (K_{IC}, MPa· $m^{1/2}$) of 8YSZ with different surface machining finish measured by micro Vickers indentation technique at ambient temperature

State	Equation (6.2)		Equation (6.3)		Equation (6.4)		Equation (6.5)	
	K_{IC}	std.	K_{IC}	std.	K_{IC}	std.	K_{IC}	std.
As-fired	1.90	0.10	1.22	0.21	1.89	0.13	1.80	0.16
Polished	2.22	0.20	1.99	0.58	2.25	0.17	2.21	0.16

6.3 Conclusions and discussions

The following conclusions can be drawn based on the above discussions and some of the experimental results from previous chapters.

- The Al_2O_3 additive with amount up to 3 mol% has little effects on the biaxial flexural strength of 8YSZ substrates at temperatures from ambient to 1000°C.

- Although the 3YSZ additive with amount up to 30 wt% can change the biaxial flexural strength of 8YSZ substrates, the effects are slight. The biaxial flexural strength of 10-wt% 3YSZ doped 8YSZ is lower than that of pure 8YSZ. While the biaxial flexural strength of 30-wt% 3YSZ doped 8YSZ is higher than that of pure 8YSZ at ambient temperature, the improvement is counterbalanced by its lower biaxial flexural strength at high temperature (1000°). The 3YSZ additive decreases the biaxial flexural strength of 8YSZ at high temperatures.

- The Al_2O_3 additive with amount up to 3 mol% does not change the dynamic biaxial flexural strength of 8YSZ substrates with stress rate lower than 1600 GPa/s, while the 3YSZ additive with amount up to 30 wt% degrades the dynamic biaxial flexural strength of 8YSZ substrates slightly.

In summary, adding additive of Al_2O_3 with amount up to 3 mol% or 3YSZ with amount up to 30 wt% cannot improve the biaxial flexural strength of 8YSZ substrate as an electrolyte material.

The mechanical properties of ceramic materials strongly depend on their microstructures (Rice, 2000). The microstructures of pure 8YSZ and some of its Al_2O_3 or 3YSZ doped composites are shown in Figures 6.22~6.28, which were taken by a field emission scanning electron microscope (FE-SEM) (Hitachi S-4500). An intersection method was used to estimate the average grain size. Lines are drawn on the SEM pictures and the distance between two grain-boundaries is measured along the lines.

The average grain size of pure 8YSZ is found from Figure 6.22 to be 2.1 μm. Figures 6.23~6.25 are the images of microstructures of Al_2O_3 doped 8YSZ. The Al_2O_3 in these SEM micrographs show as dark spots, and most of them are segregated at the grain boundaries. The average grain size of 1 and 2-mol% Al_2O_3 doped 8YSZ is 3.0 μm, slightly larger than that of 8YSZ. The grain size of 3-mol% Al_2O_3 doped 8YSZ shows larger close to the Al_2O_3 particles than that elsewhere. The average grain size of 3-mol% Al_2O_3 doped 8YSZ is 1.8 μm, slightly smaller than that of 8YSZ. In general, the grain size of 8YSZ with Al_2O_3 additive amount up to 3-mol% changes insufficiently. This is consistent with the biaxial flexural strength behavior of 8YSZ with Al_2O_3 additive amount up to 3-mol%.
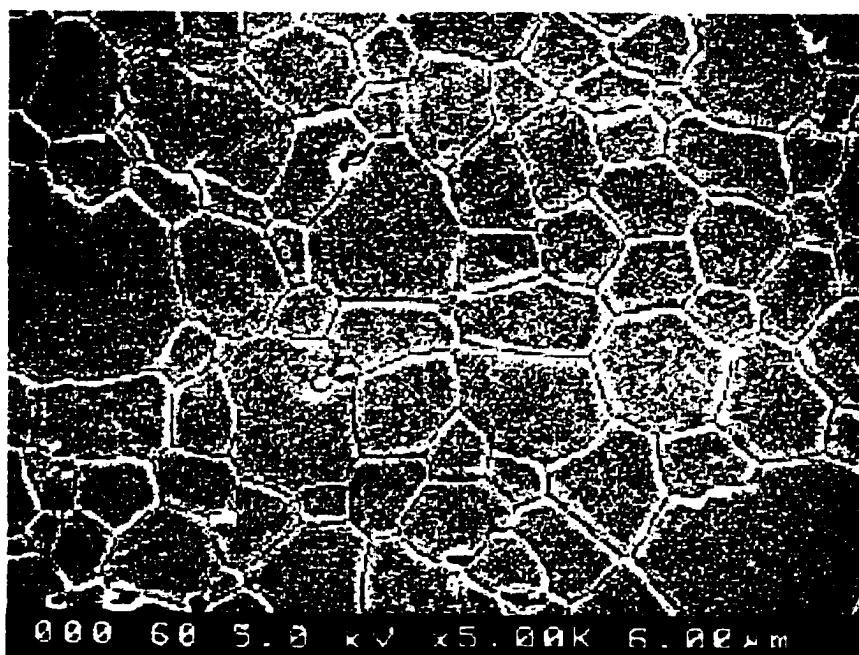
Figure 6. 22 SEM micrograph of pure 8YSZ.
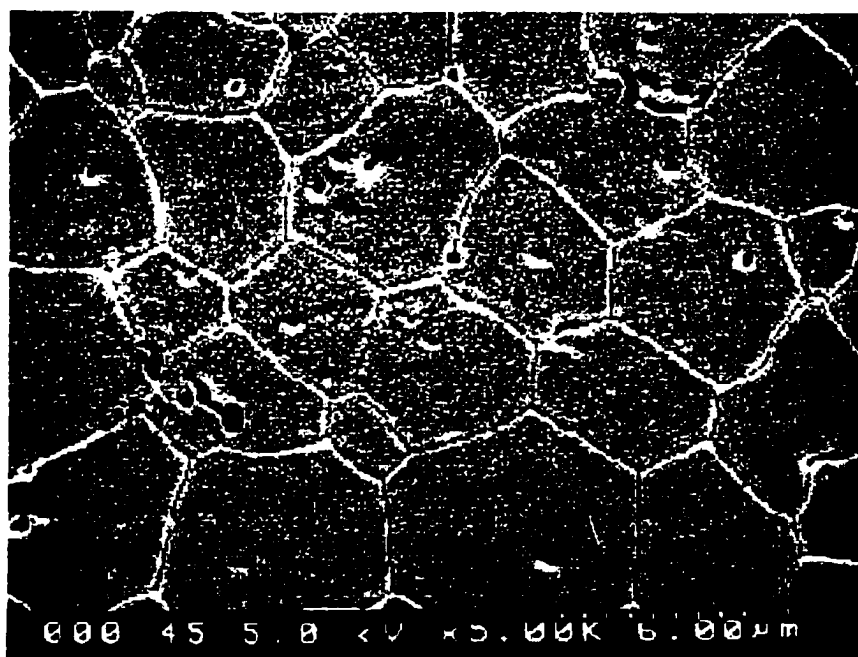
Figure 6. 23 SEM micrograph of 1-mol% AL$_2$O$_3$ doped 8YSZ (1A).
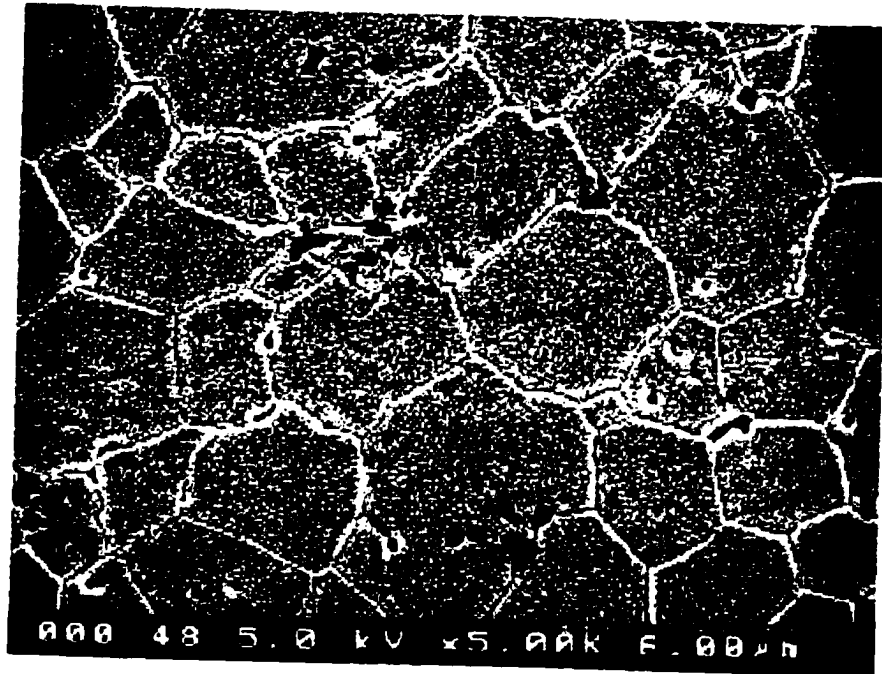
Figure 6. 24 SEM micrograph of 2-mol% AL2O3 doped 8YSZ (2A).
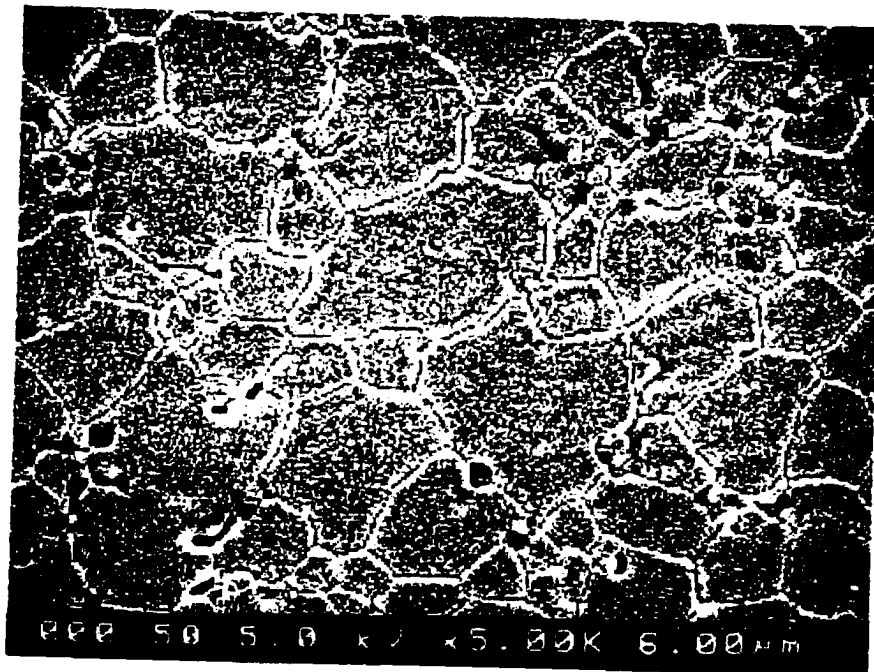
Figure 6. 25 SEM micrograph of 3-mol% AL2O3 doped 8YSZ (3A).
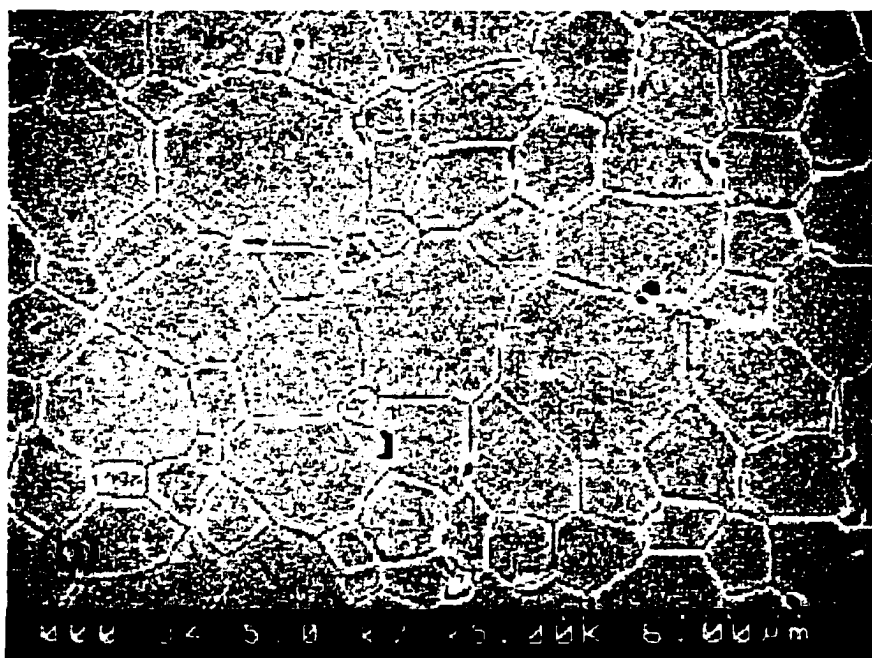
Figure 6. 26 SEM micrograph of 10-wt% 3YSZ doped 8YSZ (1Y).
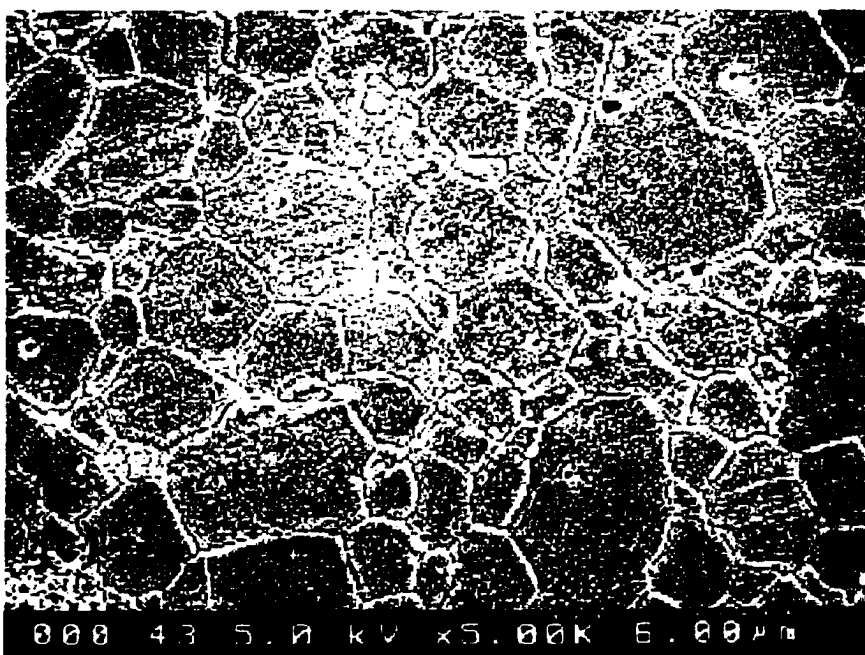
Figure 6. 27 SEM micrograph of 30-wt% 3YSZ doped 8YSZ (3Y).
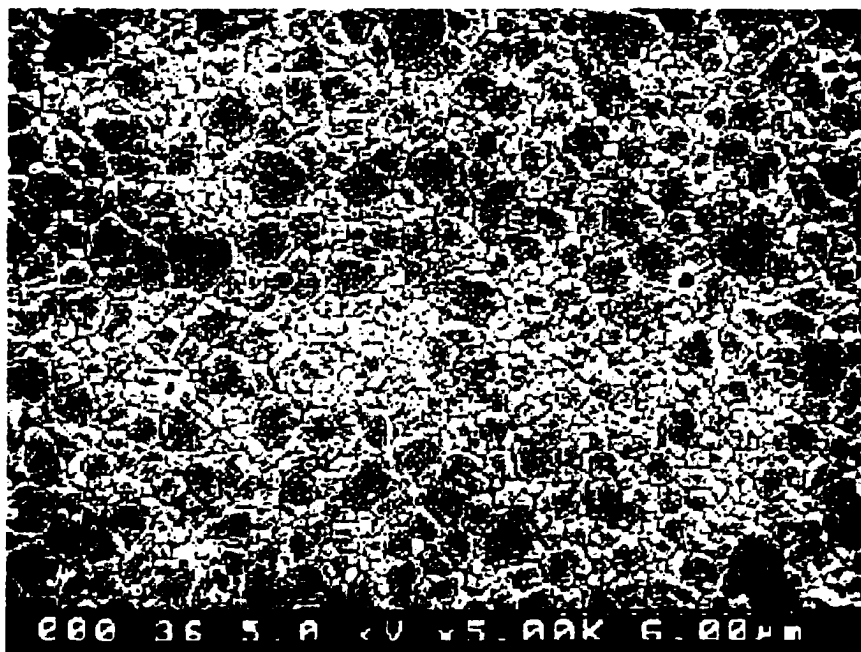
Figure 6. 28 SEM micrograph of 50-wt% 3YSZ doped 8YSZ (5Y).

The microstructures of 3YSZ doped 8YSZ is shown in Figures 6.26~6.28. The average grain size of 3YSZ doped 8YSZ keeps in a same level with 3YSZ amount up to 30 wt%. However, the grain size of 50-wt% 3YSZ doped 8YSZ drastically decreases to 0.7 μm. The 3YSZ additive acts as an inhibitor of 8YSZ to slow down its grain growth. Therefore, it is probably necessary to add 3YSZ additive with amount at least up to 50 wt% to change the biaxial flexural strength significantly. This is consistent with the research results of Allemann et al.'s, who investigated the grain growth of differently doped zirconia (Allemann, Michel, Märki, Gauckler, and Moser, 1995).

The images of microstructures shown in Figures 6.23~6.28 were taken by Brach (2000). Unfortunately, there is no material composition listed in Table 1.2 possessing a

drastically different microstructure from pure 8YSZ. It thus expects no drastic change in their biaxial flexural strength behaviors.

6.4 Summary

The biaxial flexural strength of different material compositions listed in Table 1.2 was compared. No obvious overall improvement to the 8YSZ ceramic substrates in the biaxial flexural strength has been observed by adding Al_2O_3 additive with amount up to 3 mol% or 3YSZ additive with amount up to 30 wt%. The reason might be that the amount of additive is not enough to change the microstructure of 8YSZ drastically. Therefore, there is no obvious advantage to use a doped version of 8YSZ listed in the Table 1.2 to take place of pure 8YSZ as the electrolyte material.

CHAPTER 7

CONCLUSIONS AND FUTURE WORK

The conclusions in this dissertation are summarized in the first section of this chapter. Then, two topics are discussed in the second section for future work—experimental methods as well as associated analytical material models and possible solutions to the strength problem of electrolytes.

7.1 Summary of conclusions

1. The piston-on-3-ball loading configuration was determined to best fit the needs for investigating the biaxial flexural strength of ceramic substrates. Specific stress distribution functions for a specimen under the piston-on-3-ball loading configuration were formulated.

2. Probability distribution functions of biaxial flexural strength for a specimen under the piston-on-3-ball loading condition have been derived using different fracture failure criteria. The final formulae are in a form of the Weibull cumulative probability distribution function. Therefore, the experimental data from piston-on-3-ball tests can be processed with the Weibull treatment. The Weibull parameters are proven to be the

characteristics of the population of surface defects. These Weibull parameters can be used to predict the failure behavior of the tested material under other loading conditions.

3. A dynamic piston-on-3-ball experimental technique for determining the biaxial flexural strength of thin ceramic substrates at high loading rates has been developed and verified by experiments. The loading configuration is the same as the quasi-static piston-in-3-ball experimental technique, making the high loading rate results directly comparable to the standard quasi-static results. Analytical modeling of the technique guided the experimental design and was used to judge the validity of experimental results. The upper and lower limits of the loading rate range for a valid experiment with a specific specimen were analyzed and determined.

4. A new model for dynamic strength under constant high stress-rate loading for brittle materials was developed based on the concept of cumulative damage. The parameters in this model can be experimentally identified using an overall least squares curve-fitting technique for all the data at different loading stress-rates. This model avoids the massive requirements on experimental data that are neither economical nor practical to obtain. It provides an overall insight into the dynamic behavior of the strength of ceramic materials.

5. The quasi-static piston-on-3-ball biaxial flexural strength test method at ambient temperature has been evolved into an experimental technique for

measuring the biaxial flexural strength of ceramic substrates at elevated temperatures, making it possible to investigate the biaxial flexural strength of ceramic substrates at elevated temperatures, which has been proven to be different from that at ambient temperature.

6. A new Vickers micro-indentation toughness measurement technique was developed and used to measure the fracture toughness of ceramic substrates without polishing, making it possible to study the mechanical properties of ceramic substrates with as-fired surface conditions.

7. 8YSZ ceramic substrate and its compositions with Al_2O_3 additive amount up to 3 mol% and 3YSZ additive amount up to 30 wt% have been experimentally investigated at both ambient temperature and elevated temperatures, and under both quasi-static and high stress-rate loading conditions. The experimental results showed that the additives could not change the biaxial flexural strength of 8YSZ drastically.

7.2 Future work

The following work is still need to be conducted if time and resources are available.

7.2.1 Experimental methods and material models

For the electrolyte design purposes, it is necessary to investigate the effects of temperature and loading rate on the biaxial flexural strength of thin ceramic substrates. In this dissertation, quasi-static piston-on-3-ball experimental techniques at both ambient and elevated temperatures were employed to investigate the biaxial flexural strength of 8YSZ and its compositions. A dynamic piston-on-3-ball experimental technique at ambient temperature was developed and employed. For the completeness of the piston-on-3-ball experimental technique series, a dynamic piston-on-3-ball experimental technique at elevated temperatures still need to be developed. Although spall strength can be measured at elevated temperatures through some explosive loading techniques (Kanel et al., 1996), there is no dynamic experimental technique available for measuring dynamic biaxial flexural strength at elevated temperatures.

To develop a dynamic piston-on-3-ball experimental technique at elevated temperatures, the main difficulty is the design of fixture. The fixture style of the dynamic piston-on-3-ball experimental technique at ambient temperature can be kept, while the fixture materials must be chosen to possess their same physical and mechanical properties

at elevated temperature at least up to 1200°C. In addition, the mechanical impedance of the transmission bar material must be carefully designed if the transmission bar is still based on the quartz-crystal-embedded split Hopkinson pressure bar technique (Chen, Lu, and Zhou, 2000).

The Weibull statistical model can be used to describe the strength behavior of ceramic material under quasi-static loading conditions. The new model developed in Chapter 4 can be used to predict the dynamic strength of ceramic materials under constant high stress-rate loading condition. However, there is no model available to relate the strength behavior of ceramic materials at elevated temperatures with its other property parameters. Although many reports can be found in the literature revealing that the strength behavior of ceramic materials is different at elevated temperature from that at ambient temperature (Rice, 2000), there is still no comprehensive description about its physical mechanism, which can result in an analytical model to predict the strength behavior of ceramic materials at elevated temperatures. Discussions were all on some specific material compositions. Therefore, theoretical study in this area still needs more systematic efforts.

7.2.2 Possible solutions to the strength problem of electrolytes

It has been proven that adding Al_2O_3 additive or 3YSZ additive is not a successful solution to the strength problem of 8YSZ substrates as a proper electrolyte material. The other intuitive solution might be hot-isostatic-pressing (HIP), which has been widely used to successfully improve mechanical properties of materials. The strength of dense yttria

stabilized tetragonal zirconia ceramics containing 2~6 mol% Y_2O_3 was enhanced significantly by HIPping (Tsukuma, Kubota, and Tsukidate, 1983). However, HIPping may not be always successful to improve the strength of ceramic materials (Koike, Tashima, Wakiya, Maruyama, and Oikawa, 1996). In this study, some specimens with compositions listed in Table 1.2 were processed by HIPping one hour under 25,000 psi pressure at 1500°C temperature. The HIPped specimens were then tested using the quasi-static piston-on-3-ball experimental technique to measure their biaxial flexural strengths at both ambient and elevated temperatures. Tables 7.1 and 7.2 list the test results at ambient temperature (24°C) and at an elevated temperature (800°C), respectively. By taking scatter characteristic of ceramic materials into account, there is no reason to conclude from these biaxial flexural strength data that the HIPping processing can improve their mechanical properties, at least their biaxial flexural strength.

For the purposes of the design of a reliable electrolyzer, the development of electrolyte material with high strength is one method. Another method is to design an optimal structure to apply proper boundary conditions to the electrolyte. Therefore, only a portion of external loads applies on the electrolyte disk. There are many principles that can be employed for this purpose such as the concept of dynamic vibration absorber and damper (Inman, 2001), in which dynamic external loading mainly absorbed by the dynamic vibration absorber and damper, leaving the electrolyzer almost free of loading.

Table 7. 1
Biaxial flexural strength data (MPa) from quasi-static piston-on-3-ball experiments at ambient temperature (24°C)

No.	8YSZ	1A	2A	3A	1Y	2Y	3Y
1	299.2	178.5	354.7	424.4	376.2	335.8	308.7
2	408.7	398.5	390.8	361.1	332.1	330.3	339.3
3	351.7	248.7	308.4	295.9	311.1	313.1	350.6
4		347.6	327.9	313.4			280.7
Mean	353.2	293.3	345.5	348.7	339.8	326.4	319.8

Table 7. 2
Biaxial flexural strength data (MPa) from quasi-static piston-on-3-ball experiments at elevated temperature (800°C)

No.	8YSZ	1A	2A	3A	1Y	2Y	3Y
1	224.6	269.4	191.6	283.9	215.4	82.1	211.0
2	221.2	213.5	243.6	252.7	84.4	190.7	227.9
3					197.6		
Mean	222.9	241.5	217.6	268.3	165.8	136.4	219.4

The above-mentioned methods may be combined to obtain proper solutions to the strength problem of eletrolyte materials. One kind of such solutions may result from applying proper electrode coatings to electrolyte substrates. Kumar and Sørensen (2001) studied fracture energy and crack growth in surface treated 8YSZ for solid fuel cell (SOFC) applications. The critical part of the electrolyzer is a stack of electrochemical cell

whose central portion includes three different layers: two porous electrodes (an anode and a cathode) separated by a dense, oxygen ion conducting electrolyte (Figure 1.3). There are many possible structures of electrolyzer cell such as a 8YSZ substrate sandwiched between thin layers of platinum (forming ductile/brittle/ductile layered structure) or perovskite (forming brittle/brittle/brittle layered structure) electrodes. The porous materials for electrodes must possess similar thermal expansion property as the electrolyte material, as well as high electrical conductivity at operating temperatures. In addition, we can seek some proper electrode materials from possible candidates of electrode materials to form an electrolyzer structure, which can enhance the strength of the electrolyte substrates. For example, Kumar and Sϕorensen (2001) found that the fracture resistance of the surface coated with NiO-8YSZ cermet was increased from 3.5 to 5.48 J/m^2 in the initiation fracture toughness and from 2.8 to 3.8 J/m^2 in the arrest value, which remained almost unchanged in the case of NiO-MnO2 coating and NiO-LSM (lanthanum (0.85), strontium (0.15), and manganite) composite. The proper coating material as an electrode can significantly increase the frequencies of occurrence of toughening mechanisms such as multiple cracking, grain and crack bridging, and crack deflection. Therefore, searching proper electrode materials and coating processes may exist some potential for the improvement of the strength of the electrolyte.

REFERENCES

Adams, J. W., Ruh, R., and Mazdiyasni, K. S., 1997. Young's Modulus, Flexural Strength, and Fracture of Yttria-Stabilized Zirconia versus Temperature. Journal of the American Ceramic Society, Vol. 80 [4], 903-908.

Allemann, J. A., Michel, B., Märki, H.-B., Gauckler, L. J., and Moser, E. M., 1995. Grain Growth of Differently Doped Zirconia. Journal of European Ceramic Society, Vol. 15, 951-958.

Anton R. J. and Subhash G., 2000. Dynamic Vickers Indentation of Brittle Materials. Wear, 239, 27-35.

ASTM C 1161-94, 1995. Standard Test Method for Flexural Strength of Advanced Ceramics at Ambient Temperature. American Society of Testing and Materials Annual Book of Standards, ASTM, West Conshohocken, PA, Vol. 15.01, 304-310.

ASTM C 1211-92, 1995. Standard Test Method for Flexural Strength of Advanced Ceramics at Elevated Temperatures. American Society of Testing and Materials Annual Book of Standards, ASTM, West Conshohocken, PA, Vol. 15.01, 337-346.

ASTM C 1273-95a, 1995. Standard Test Method for Tensile Strength of Monolithic Advanced Ceramics at Ambient Temperatures. American Society of Testing and Materials Annual Book of Standards, ASTM, West Conshohocken, PA, Vol. 15.01, 383-400.

ASTM C 1327-96a, 1996. Standard Test Method for Vickers Indentation Hardness of Advanced Ceramics. American Society of Testing and Materials Annual Book of Standards, Vol. 15.01, 543-47.

ASTM F 394-78, 1995. Standard Test Method for Biaxial Flexural Strength (Modulus of Rupture) of Ceramic Substrates. American Society of Testing and Materials Annual Book of Standards, ASTM, West Conshohocken, PA, Vol. 15.01, 469-473.

Atkinson, A. and Selçuk, A., 2000. Mechanical Behaviour of Ceramic Oxygen Ion-Conducting Membranes. Solid State Ionics, Vol. 134, 59-66.

Batdorf, S. B. and Chang, D. J., 1979. On the Relation Between the Fracture Statistical of Volume Distributed and Surface-Distributed Cracks. International Journal of Fracture 15, 191-199.

Batdorf, S. B. and Crose, J. G., 1974. A Statistical Theory for the Fracture of Brittle Structures Subjected to Nonuniform Polyaxial Stresses. Journal of the American Ceramic Society 41, 459-65.

Batdorf, S. B. and Heinisch, H. L., Jr., 1978. Weakest Link Theory Reformulated for Arbitrary Fracture Criterion. Journal of the American Ceramic Society 61, 355-58.

Batdorf, S. B. and Sines, G., 1980. Combining Data for Improved Weibull Parameter Estimation. Journal of the American Ceramic Society 63, 214-218.

Bassali, W. A., 1957. The Transverse Flexure of Thin Elastic Plates Supported at Several Points. Proceedings of the Cambridge Philosophical Society 53, 728-743.

Bourne, N., Millett, J., Rosenberg, Z., and Murray, N., 1998. On the Shock Induced Failure of Brittle Solids. Journal of the Mechanics and Physics of Solids, Vol. 46, No. 10, 1887-1908.

Bouzid, S., Nyoungue, A., Azari, Z., Bouaouadja, N., and Pluvinage, G., 2001. Fracture Criterion for Glass Under Impact Loading. International Journal of Impact Engineering, Vol. 25, 831-845.

Brach, S., 2000. Optimization of Electrolyte Material for Use in Solid Oxide Electrolysis Cells. Master's thesis, University of Arizona, Tucson.

Budiansky, B. and O'Connell, R. J., 1976. Elastic Moduli of a Cracked Solid. International Journal of Solids and Structures, Vol. 12, 81-97.

Burelli, M., Maschio, S., and Lucchini, E., 1997. Strength and Toughness of Alumina-Zirconia Ceramics Under Biaxial Stress. Journal of Materials Science Letters, Vol. 16, 661-662.

Cattell, M. J., Chadwick, T. C., Knowles, J. C., Clarke, R. L., and Lynch, E., 2001. Flexural Strength Optimisation of a Leucite Reinforced Glass Ceramic. Dental Materials 17, 21-33.

Chao, L. Y., and Shetty, D. K., 1990. Equivalence of Physically Based Statistical Fracture Theories for Reliability Analysis of Structural Ceramics in Multiaxial Loading. Journal of the American Ceramic Society, Vol. 73, 1917-1921.

Chao, L. Y. and Shetty, D. K., 1991. Reliability Analysis of Structural Ceramics Subjected to Biaxial Flexure. Journal of the American Ceramic Society, Vol. 74, 333-344.

Chen, E. P., 1995. Dynamic Brittle Material Response Based on a Continuum Damage Model. In: Impact, Waves and Fracture, edited by Batra, R. C., Mal, A. K., and MacSmithigh, G. P., AMD-Vol. 205, ASME, pp. 21-34.

Chen, W., Lu, F., and Zhou, B., 2000. A Quartz-Crystal-Embedded Split Hopkinson Pressure Bar for Soft Materials. Experimental Mechanics, Vol. 40, No. 1, 1-6.

Chen, W. and Ravichadran, G., 1992. Micromechanics of Damage in Ceramic Materials Under Dynamic Uniaxial Compression. In: *Advances in Local Fracture/Damage Models for the Analysis of Engineering Problems*, edited by Giovanola, J. H. and Rosakis, A. J., AMD-Vol. 137, ASME, pp. 121-130.

Clifton, R., 2000. Response of Materials Under Dynamic Loading. International Journal of Solids and Structures, Vol. 37, 105-113.

Cook R. F. and Pharr G. M., 1990. Direct Observation and Analysis of Indentation Cracking in Glass and Ceramics. Journal of the American ceramic society, Vol. 73, 787-817.

Delameter, W. R., Herrmann, G., and Barnett, D. M., 1975. Weakening of An Elastic Solid by a Rectangular Array of Cracks. Journal of Applied Mechanics, Vol. 42, 74-80.

Denoual, C., Barbier, G., and Hild, F., 1997. A Probabilistic Approach for Fragmentation of Brittle Materials Under Dynamic Loading. Mechanics of Solids and Structures, 325 (IIb), 685-691.

Denoual, C. and Hild, F., 2000. A Damage Model for the Dynamic Fragmentation of Brittle Solids. Computer Methods in Applied Mechanics and Engineering, Vol. 183, 247-258.

Doyle, J., 1989. *Wave Propagation in Structures—An FFT-based Spectral Analysis Methodology*. Springer-Verlag New York, New York.

Esper, F. J., Friese, K. H., and Geier, H., 1983. Mechanical, Thermal, and Electrical Properties in the System of Stabilized $ZrO_2(Y_2O_3)/\alpha\text{-}Al_2O_3$. In: *Science and Technology of Zirconia II*, edited by Claussen, N., Rühle, M., and Heuer, A. H., The American Ceramic Society, Inc., Columbus, OH. pp. 528-536.

Evans, A. G., 1978. A General Approach for the Statistical Analysis of Multiaxial Fracture. Journal of the American Ceramic Society, Vol. 61, 302-308.

Evans, A. G., 1984. Toughening Mechanisms in Zirconia Alloys. In: *Fracture in Ceramic Materials*, edited by Evans, A. G., pp. 16-55.

Ferber, M. K., Wereszczak, A. A., and Jenkins, M. G., 1998. Fracture Strength. In: *Mechanical Testing Methodology for Ceramic Design and Reliability*, edited by David C. Cranmer and David W. Richerson, Marcel Dekker, Inc., New York, NY.

Fessler, H. and Fricker, D. C., 1984. A Theoretical Analysis of the Ring-on-Ring Loading Disk Test. Journal of the American ceramic society, Vol. 67, 582-588.

Freund, L. B., 1990. *Dynamic Fracture Mechanics*. Cambridge University Press, Cambridge, New York.

Frew, D. J., Forrestal, M. J. and Chen, W., 2001. A Split Hopkinson Pressure Bar Technique to Determine Compressive Stress-Strain Data for Rock Materials. Experimental Mechanics, Vol. 41, No. 1, 40-46.

Frew, D. J., Forrestal, M. J., and Chen, W., 2002. Pulse Shaping Technique for Testing Brittle Materials with a Split Hopkinson Pressure Bar. Experimental Mechanics, Vol. 42, No. 1.

Grady, D. E., 1995. Dynamic Properties of Ceramic Materials. Sandia Report, SAND94-3266, UC-704.

Grady, D. E., 1998. Shock-Wave Compression of Brittle Solids. Mechanics of Materials, Vol. 29, 181-203.

Graff, K., 1975. *Wave Motion in Elastic Solids*. Ohio State University Press, Columbus, OH.

Gray, G., 2000. Classic Split-Hopkinson Pressure Bar Testing. ASM Handbook, Vol. 8, 462-476, ASM International, Materials Park, OH.

Hannink, R., Kelly, P., and Muddle, B., 2000. Transformation Toughening in Zirconia-Containing Ceramics. Journal of the American ceramic society, Vol. 83 [3], 461-487.

Hendriksen, P. V. and Jørgensen, O., 1996. Lattice Expansion Induced Strains in SOFC Stacks and Their Significance for Stack Integrity. In: *Proceedings of the 17th Risø International Symposium on Materials Science, High Temperature Electrochemistry: Ceramics and Metals*, edited by Poulsen, F. W., Bonanos, N., Linderoth, S., Mogensen, M., and Zachau-Christiansen, B., Risø National Laboratory, Roskilde, Denmark.

Hoshide, T., Murano, J., and Kusaba, R., 1998. Effect of Specimen Geometry on Strength in Engineering Ceramics. Engineering Fracture Mechanics, Vol. 59, No. 5, 655-665.

Hulm, B. J., Parker, J. D., and Evans, W. J., 1998. Biaxial Strength of Advanced Materials. Journal of Materials Science, Vol. 33, 3255-3266.

Ingel, R. P., Rice, R. W., and Lewis, D., 1982. Room-Temperature Strength and Fracture of ZrO2-Y2O3 Single Crystals. Journal of the American Ceramic Society, Vol. 65, C-108-C-109.

Ingel, R. P., Lewis, D., Bender, B. A., and Rice, R. W., 1982. Temperature Dependence of Strength and Fracture Toughness of ZrO2-Y2O3 Single Crystals. Journal of the American Ceramic Society, Vol. 65, C-150-C-152.

Inman, D. J., 2001. *Engineering Vibration*, 2rd edition. Prentice Hall, Upper Saddle River, NJ.

Irwin, G., 1965. Crack Extension Force for a Part-Through Crack in a Plate. Journal of Applied Mechanics, Vol. 29 [4], 651-54.

Jayatilaka, A., 1979. *Fracture of Engineering Brittle Materials*. Applied Science Publishers LTD, London.

Kandil, H. M., Greiner, J. D., and Smith, J. F., 1984. Single-Crystal Elastic Constants of Yttria-Stabilized Zirconia in the Range 20° to 700°C. Journal of the American Ceramic Society, Vol. 67 [5], 341-346.

Kanel, G. I., Razorenov, S. V., Bogatch, A., Utkin, A. V., Fortov, V. E., and Grady, D. E., 1996. Spall Fracture Properties of Aluminum and Magnesium at High Temperatures. Journal of Applied Physics, Vol. 79 (11), 8310-8317.

Kao, R., Perrone, N., and Capps, W., 1971. Large-Deflection Solution of the Coaxial-Ring-Circular-Glass-Plate Flexure Problem. Journal of the American Ceramic Society, Vol. 54 (11), 566-571.

Kassir, M. K., and Sih, G. C., 1966. Three-Dimensional Stress Distribution Around an Elliptical Crack Under Arbitrary Loadings. Transactions of the ASME, Series E, 89, 601-611.

Kelly, A., and MacMillan, N. H., 1986. *Strong Solids*, 3rd edition. Oxford University Press, Oxford.

Kemeny, J. and Cook, N. G. W., 1986. Effective Moduli, Non-linear Deformation and Strength of a Cracked Elastic Solid. International Journal of Rock Mechanics and Mining Science & Geomechanics Abstracts, Vol. 23, No. 2, 107-118.

Kennedy, V. and Jonse, O., 1969. Longitudinal Wave Propagation in a Circular Bar Loaded Suddenly by a Radially Distributed End Stress. Journal of Applied Mechanics, Vol. 36, 470-478.

Kirstein, A. F., Pell, W. H., Woolley, R. M., and Davis, L. J., 1966. Deflection of Centrally Loaded Thin Circular Elastic Plates on Equally Spaced Point Supports. Journal of Research of the National Bureau of Standards, Vol. 70C, 227-244.

Kirstein, A. F., and Woolley, R. M., 1967. Symmetrical Bending of Thin Circular Elastic Plates on Equally Spaced Point Supports. Journal of Research of the National Bureau of Standards, Vol. 71C, 1-10.

Koike, J., Tashima, S., Wakiya, S., Maruyama, K., and Oikawa, H., 1996. Mechanical Properties and Microstructure of Centrifugally Compacted Alumina and Hot-Isostatically-Pressed Alumina. Material Science and Engineering A220, 26-34.

Kosmač, T., Oblak, C., Jevnikar, P., Funduk, N., and Marion, L., 1999. The effect of surface grinding and sandblasting on flexural strength and reliability of Y-TZP zirconia ceramic. Dental Materials, Vol. 15, 426-433.

Kumar, A. and Søorensen, B., 2000. Fracture Resistance and Stable Crack-Growth Behavior of 8-mol%-Yttria-Stabilized Zirconia. Journal of the American ceramic society, Vol. 83 [5], 1199-1206.

Kumar, A. and Søorensen, B., 2001. Fracture Energy and Crack Growth in Surface Treated Yttria Stabilized Zirconia for SOFC Applications. Material Science and Engineering A000, in press.

Lambert, D. E. and Ross, C. A., 2000. Strain Rate Effects on Dynamic Fracture and Strength. International Journal of Impact Engineering, Vol. 24, 985-998.

Lawn, B., 1993. *Fracture of Brittle Solids*. Cambridge University Press, New York, NY.

Lawn, B. and Wilshaw, R., 1975. *Fracture of Solids*, Cambridge University Press, New York, NY.

Lowrie, F. L. and Rawlings, R. D., 2000. Room and High Temperature Failure Mechanisms in Solid Oxide Fuel Cell Electrolytes. Journal of the European Ceramic Society, Vol. 20, 751-760.

Mazars, J. and Pijaudier-Cabot, G., 1996. From Damage to Fracture Mechanics and Conversely: A Combined Approach. International Journal of Solids and Structures, Vol. 33, No. 20-22, 3327-3342.

Mori, M., Abe, T., Itoh, H., Yamamoto, O., Takeda, Y., and Kawahara, T., 1994. Cubic-Stabilized Zirconia and Alumina Composites as Electrolytes in Planar Type Solid Oxide Fuel Cells. Solid State Ionics, Vol. 74, 157-164.

Morozov, N. and Petrov, Y., 2000. *Dynamics of Fracture*. Springer-Verlag Berlin Heidelberg.

Newman, C., Jr. and Raju, I. S., 1981. An Empirical Stress Intensity Factor Equation for the Surface Crack. Engineering Fracture Mechanics, Vol. 15, 185-192.

Niihara, K., Morena, R., and Hasselman D. P. H., 1982. Evaluation of KIC of Brittle Solids by the Indentation Method with Low Crack-to-Indent Ratios. Journal of Materials Science Letters, Vol. 1, 13-16.

Palaniswamy, A. and Knauss, W. G., 1978. On the Problem of Crack Extension in Brittle Solids Under General Loading. Mechanics Today 4, 87-148.

Pasciak, G., Prociow, K., Mielcarek, W., Gornicka, B., and Mazurek, B., 2001. Solid Electrolytes for Gas Sensors and Fuel Cells Applications. Journal of the European Ceramic Society, Vol. 21, 1867-1870.

Ponton C. B. and Rawlings R. D., 1989a. Vickers Indentation Fracture Toughness Test, Part 1. Review of Literature and Formulation of Standardised Indentation Toughness Equations. Materials Science and Technology, Vol. 5, 865-72.

Ponton C. B. and Rawlings R. D., 1989b. Vickers Indentation Fracture Toughness Test, Part 2. Application and Critical Evaluation of Standardised Indentation Toughness Equations. Materials Science and Technology, Vol. 5, 961-76.

Rajendran, A. M., 1994. Modeling the Impact Behavior of AD85 Ceramic Under Multiaxial Loading. International Journal of Impact Engineering, Vol. 15 (6), 749-768.

Ravichandran, G., and Subhash, G., 1994a. Critical Appraisal of Limiting Strain Rates for Compression Testing of Ceramics in a Split Hopkinson Pressure Bar. Journal of the American ceramic society, Vol. 77, No. 1, 263-67.

Ravichandran, G., and Subhash, G., 1994b. A Micromechanical Model for Strain Rate Behavior of Ceramics. International Journal of Solids and Structures, Vol. 32, No. 17/18, 2627-2646.

Rice, R. W., 1997. Review: Effects of Environment and Temperature on Ceramic Tensile Strength-Grain Size Relations. Journal of Materials Science, Vol. 32, 3071-3087.

Rice, R. W., 2000. Mechanical Properties of Ceramics and Composites. Marcel Dekker, Inc., New York, NY.

Richerson, D. A., 1992. Modern Ceramic Engineering, 2nd edition. Marcel Dekker, Inc., New York, NY.

Riou, P., Denoual, C., and Cottenot, C. E., 1998. Visualization of the Damage Evaluation in Impacted Ceramic Carbide Ceramics. International Journal of Impact Engineering, Vol. 21 (4), 225-235.

Rosakis, A. and Ravichandran, G., 2000. Dynamic Failure Mechanics. International Journal of Solids and Structures, Vol. 37, 331-348.

Salem, J. A., and Jenkins, M. G., 1999. A Test Apparatus for Measuring the Biaxial Strength of Brittle Materials. Experimental Techniques, Vol. 45, 19-23.

Sakuma, T., Eda, H., and Suto, H., 1983. Composition Optimization of ZrO2-Y2O3 Alloy to Improve the Fracture Toughness. In: *Science and Technology of Zirconia III*, edited by Somiya, S., Yamamoto, N., Yanagida, H., the American Ceramic Society, Inc., Westerville, OH. pp. 357-363.

Salem, J. A., and Jenkins, M. G., 1999. A Test Apparatus for Measuring the Biaxial Strength of Brittle Materials. Experimental Techniques, Vol. 23 (4), 19-23.

Selçuk, A. and Atkinson, A., 1997. Elastic Properties of Ceramic Oxides Used in Solid Oxide Fuel Cells (SOFC). Journal of the European Ceramic Society, Vol. 17 [12], 1523-1532.

Selçuk, A. and Atkinson, A., 2000. Strength and Toughness of Tape-Cast Yttria-Stabilized Zirconia. Journal of the American ceramic society, Vol. 83 [8], 2029-2035.

Shetty, D. K., 1987. Mixed-Mode Fracture Criteria for Reliability Analysis and Design With Structural Ceramics. Journal of Engineering for Gas Turbines and Power, Vol. 109, 282-289.

Shimada, M., Matsushita, K., Kuratani, S., Okamoto, T., Koizumi, M., Tsukuma, K., and Tsukidate, T., 1984. Temperature Dependence of Young's Modulus and Internal Friction in Alumina, Silicon Nitride, and Partially Stabilized Zirconia Ceramics. Journal of the American Ceramic Society, Vol. 67 [2], C-23-24.

Sih, G. C., 1984. *Handbook of Stress-Intensity Factors*. Lehigh University, Bethlehem, PA, pp. 31.

Singh, D. and Shetty, D. K., 1989a, Facture Toughness of Polycrystalline Ceramics in Combined Mode I and Mode II Loading. Journal of the American Ceramic Society, Vol. 72, 78-84.

Singh, D. and Shetty, D. K., 1989b. Microstructure Effects on Toughness of Polycrystalline Ceramics in Combined Mode I and Mode II loading. Journal of Engineering for Gas Turbines and Power, Vol. 111, 174-180.

Singhal, S. C., 2000. Advances in solid oxide fuel cell technology. Solid State Ionics, Vol. 135, 305-313.

Smith, F. W. and Sorensen, D. R., 1975. Mixed-Mode Stress Intensity Factors for Semi-Elliptical Surface Cracks. Report No. NASA-CR-134684, NASA Lewis Research Center, Cleveland, OH.

Sridhar, K. R. and Vaniman, B. T., 1997. Oxygen Production on Mars Using Solid Oxide Electrolysis. Solid State Ionics, Vol. 93, 321-328.

Tsukuma, K., Kubota, Y., and Tsukidate, T., 1983. Thermal and Mechanical Properties of Y_2O_3-Stabilized Tetragonal Zirconia Polycrystals. In: *Science and Technology of Zirconia II*, edited by Claussen, N., Rühle, M., and Heuer, A. H., The American Ceramic Society, Inc., Columbus, OH. pp. 382-390.

Tuler, F. R. and Butcher, B. M., 1968. A Criterion for the Time Dependence of Dynamic Fracture. International Journal of Fracture, Vol. 4, 431-437.

Wachtman, J. B., 1996. *Mechanical Properties of Ceramics*. John Wiley & Sons, Inc., New York.

Wachtman, J., Capps, W, and Mandel, J., 1972. Biaxial Flexure Tests of Ceramic Substrates. Journal of Material, JMLSA, Vol. 7, No. 2, 188-194.

Wallace, J. S., Fuller, E. R., Ueno, F., Kasori, M., Ohji, T., Kanzaki, S., and Rafaniello, W. F., 1998. Strength Measurement Metrology for an AlN Substrate. Private communication.

Weibull, W., 1939. A Statistical Theory of the Strength of Materials. *Ingenioers Vetenskaps Akademien Handlinger*, Vol. 151, 1-45.

Winnubst, A. J. A., Keizer, K., and Burggraaf, A. J., 1983. Mechanical Properties and Fracture Behavior of ZrO_2-Y_2O_3 Ceramics. Journal of Materials Science, Vol. 18, 1958-1966.